Optimization Design of Carburizing and Quenching Process in Consideration of Transformation Plasticity Mechanism

変態塑性のメカニズムを考慮した浸炭焼き入れプロセスの最適化設計

Shan Miao

Saitama Institute of Technology

March, 2019

Table of Contents

Abstract

With the progress of science and technology, the automobile is developing gradually in the direction of lightweight and low energy consumption. Therefore, electric vehicles are receiving more and more attention because of their environmentally friendly and energy-efficient. However, with the rapid development of the electric vehicle industry, it puts forward higher request to the load capacity and economy of the gearing which is the core equipment of mechanical transmission system. At present, the carburizing and quenching has been widely used for surface hardening because the hard surface gear has the advantages of thigh strength, small volume and light weight. However, distortion and fatigue properties after heat treatment are two problems commonly occurred in the production and application of transmission gears. Simultaneous preparation of gear with smaller variants and good fatigue properties is one of the major topics at present. On the other hand, transformation plasticity behavior is found to have a significant effect on the deformation and residual stress during the phase transformation of the gear. This work has three main purposes: (i) a new mathematic model is proposed to describe the transformation plasticity behavior of steels during the austenite transformation, which includes the influence of the dynamic recovery of the austenite. (ii) The combination method of orthogonal experiment and numerical simulation is used to optimize the standard heat treatment condition in reducing distortion after carburizing quenching to provide a new optimization method of minimum distortion after carburizing quenching. (iii) The optimization effects of the optimized condition are verified by comparing the fatigue limit and the crack growth rate. The strengthening mechanism of fatigue performance improvement are analyzed by comparing residual stress, domain size and microstructure with different conditions.

Acknowledgments

Chapter 1 Introduction

With the progress of science and technology, the automobile is developing gradually in the direction of lightweight and low energy consumption [1, 2]. Therefore, electric vehicles are receiving more and more attention because of their environmentally friendly and energy-efficient. However, with the rapid development of the electric vehicle industry, it puts forward higher request to the load capacity and economy of the gearing which is the core equipment of mechanical transmission system. At present, the carburizing and quenching has been widely used for surface hardening because the hard surface gear has the advantages of thigh strength, small volume and light weight. However, distortion and fatigue properties after heat treatment are two problems commonly occurred in the production and application of transmission gears. Simultaneous preparation of gear with smaller variants and good fatigue properties is one of the major topics at present. On the other hand, transformation plasticity behavior is found to have a significant effect on the deformation and residual stress during the phase transformation of the gear.

1.1 Carburizing and quenching

Carburizing and quenching process is often used in industry as a method of surface hardening technique to obtain improved mechanical properties and fatigue strength of mechanical components, such as gears, shafts and so on [3-5]. Carburizing and quenching is usually carried out on low carbon steels, which relies on high hardness surface layer to provide strength and wear resistance that cannot obtainable from the core metal [6-8].

As shown in Fig. 1-1, in the manufacturing process of mechanical structural parts, mechanical processing is roughly classified by material, design, forging, machine processing, carburizing and quenching, shot peening, cutting and polishing, etc [9-11]. From the viewpoint of improvement of productivity and reduction of manufacturing cost, the material is required to be softer and easier to be processed, and at the stage

when it is used as a part after finishing the final processing, it is desirable to have high intensity, high fatigue strength and high reliability. Therefore, carburizing and quenching technology gives the material a soft and easy to process characteristic before processing and high strength in the final process after parts processing to have superior lifetime and high reliability. In the future, carburizing and quenching technology is indispensable in the industrial field in order to satisfy the needs for environmentally friendly and inexpensive steel.
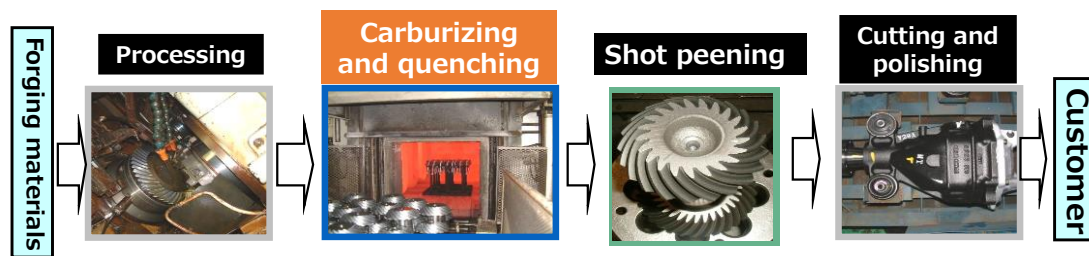
Fig. 1-1 Mechanical processing of gears

The initial carbon content in most steels used for carburizing and quenching is the range of 0.10% to 0.30%. Steel 20MnCrS5 is one of the most important metallic materials used for many applications including mechanical structural parts due to its characteristics and diversity of functions, and one of the technologies that brings various characteristics and functions of steel [12, 13]. In the automotive industry, carburized 20MnCrS5 steel is typically used for differential ring gears, camshafts and transmission gears for its excellent carburizing response with good hardenability for most section sizes [12, 14, 15]. The carburizing and quenching process includes two parts, carburization and quenching.

1.1.1 Carburization

Carburization is a case hardening process in which carbon is diffused into the surface layers of a steel part at a temperature below its melting point and above its A_3 critical temperature, at which austenite, with its high solubility for carbon, is the stable crystal structure [16, 17]. It is the addition of carbon at the surface of low-carbon steels within the austenitic region temperature, which is between 850°C and 950°C for carburizing steels generally. Hardening is accomplished when the subsequent high-

carbon surface layer is quenched to form martensite so that a high-carbon martensitic case with good wear and fatigue resistance is superimposed on a tough, low carbon steel core as shown in Fig. 1-2 [18].
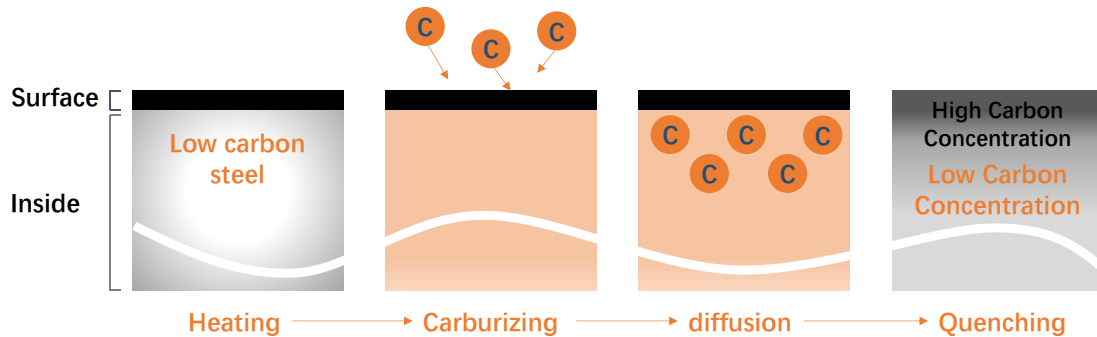
Fig. 1-2 Carbon diffusion process in carburizing and quenching

In order to ensure a satisfactory and reliable intensity and fatigue strength of carburized parts – it is imperative to understand the mechanism of carbon transfer and to accurately predict carbon concentration profile and case depth during the carburizing and quenching process. Successful carburizing performance depends on the effective control of the three principal variables: temperature, time and the carburizing atmosphere. Some research has been performed to investigate the effect of these process parameters on the carburizing kinetic coefficients, i.e. the mass transfer coefficient and carbon diffusivity in steel [19-24]. The mass transfer coefficient has been reported to be a complex function of the atmosphere gas composition, carburizing potential, temperature and surface carbon content. The coefficient of carbon diffusion in austenite is another parameter determining the rate of carbon transport, which is strongly influenced by the carburizing temperature and carbon concentration in steel [25]. Although the mechanism of mass transport in carburizing appears to be known and understood, the results of the current industrial carburizing practices show that the carbon concentration profiles and case depths often deviate from those of the predicted ones.

The carburizing potential in the furnace is determined by the atmosphere gas composition. Accurate carbon potential calculation requires not only adequate

measurement of the gas constituents (CO, CH$_4$, CO$_2$ and H$_2$O) in the furnace but also representative sampling locations where the constituents are analyzed. Since surface carbon concentration and flux of carbon atoms from the atmosphere to the steel surface change with time, maintaining a constant atmosphere carbon potential during single stage carburization requires continuous adjustment of the set point until the parts meet the required specification. An increase in the carburizing temperature increases the rate of mass transfer both in the furnace atmosphere and steel. It also promotes excessive austenite grain growth and deteriorates the furnace condition. The effect of time on case depth is interdependent with the carburizing temperature and is often estimated by using the Harris equation [26].

1.1.2 Quenching

Quenching is also important among the heat treatment techniques. Quenching is a technique of forming a martensitic structure by heating the steel to austenite and then using a coolant such as water, oil, polymer solution or the like to set the cooling rate to be higher than the upper critical speed as shown in Fig. 1-3 [27, 28]. In quenching treatment, it is a main object to improve compressive residual stress and surface hardness, which is advantageous for material fatigue strength by obtaining a martensitic structure. But defects such as quenching cracks, deformations, burn-in, bad hardness often occur [29]. In particular, tensile residual stress is cited as a cause of quenching cracking, and it has a great influence on the strength and functionality of the manufactured parts, as well as the composition and structural defects of the material. In addition, there are problems such as residual temperature distribution in the furnace, heating temperature, heating time, etc. As a cause of defects such as residual unevenness and insufficient hardness, particularly when the coolant is convected or boiled by the vapor film, it has a large impact on the large amount of cooling unevenness that occurs [30].

Fig. 1-3 An example of quenching

1.1.3 Residual stress in carburizing and quenching

The residual stress may be defined as the self-equilibrating internal or locked-in stress remaining within a body with no applied (external) force, external constraint, or temperature gradient. These residual stresses must be balanced near the surface or in the body of a material, i.e., negative (compressive) in one region and positive (tensile) in another. Residual stresses may be generated by variations in stress, temperature, and chemical species within the body. In heat-treated materials, residual stresses may be generated by a variation in temperature (thermal gradient) alone or a combination with a change in chemical species.

When a steel part is quenched from the austenitizing temperature to room temperature, residual stresses are produced due to a combination of a thermal gradient and a phase transformation-induced volume expansion: austenite transforms to martensite or other products [31].

1.1.4 Retained austenite in carburizing and quenching

High carbon and carburized low carbon steels such as carburized 20MnCrS5 steel always contain retained austenite to varying degrees in the as-hardened and also in the quenching [32].

In hardenable steels, austenite is stable at temperatures above the A_3 and A_{cm} phase

boundaries, but is unstable below these temperatures. On quenching from the austenite-stable area, austenite transforms to martensite which usually forms at a characteristic temperature named M_S and continues to form with decreasing temperature until M_f, the temperature of 100% transformation is reached. However, in many hardenable steels such as plain carbon and low alloy steels with carbon contents more than 0.5%, the M_f temperature is below room temperature, so that a considerable quantity of untransformed austenite may be retained at room temperature in these steels [33-36].

The quantity of retained austenite depends on the austenitizing temperature, chemical composition, especially the carbon content, cooling rate and final temperature of the quenching process [34]. As to the presence of retained austenite, Grosch and Schwarz point out that the case-microstructure of carburized steels always consists of plate martensite and retained austenite for case-carbon contents higher than 0.6%. The amount of retained austenite is mainly determined by the carbon content: for steels of the same carbon content, the effect of the content of the other alloying elements is also noticeable [36]. The martensite finish temperature, M_f of plain carbon and low alloy steels with carbon contents more than about 0.5%, is below room temperature. That is why austenite that contains more than 0.5% carbon in solid solution does not completely transform into martensite when quenched to room temperature [36].

1.1.5 Distortion in carburizing and quenching

The microstructure of the steel material has undergone complicated changes during the heat treatment [37, 38]. Since the density of this metal structure varies from different tissues, phase transformation stress is generated due to the different volumes between surface and inside [39]. Due to temperature change of cooling and latent heat of phase transformation, thermal stress occurs due to the temperature distribution at the surface, the inside, or the shape of the steel material. Plastic deformation occurs due to the influence of these stresses [40, 41]. If stress is applied during the phase transformation, large transformation plasticity occurs even if it is below the yield stress at that temperature. Since the transformation plasticity strain becomes equal / greater than the

thermal strain / transformation strain and has a great influence on the deformation after the heat treatment, both heat treatment experiment and heat treatment simulation analysis need to analysis this behavior in detail.

1.1.6 Fatigue strength

Since failure caused by repeated loading accounts for at least half of all mechanical failures, the fatigue performance is prime importance for the materials which are subject to cyclic loading [42]. Carburizing and quenching process is widely used in industry, as a method of surface hardening technology to obtain improved mechanical properties and fatigue strength of mechanical components, such as gears, shafts and so on [3, 43]. The main advantages of carburizing are that they can achieve high surface hardness, compressive residual stress and good toughness at the core, which can effectively improve the surface strength, wear resistance and fatigue strength of the steel [44].

It is well known that many performances can affect the fatigue resistance of carburized parts. One of the important performances is the distribution of residual stresses. The compressive residual stresses counteract the applied tensile stresses and therefore improve the fatigue performance. The ideal hardness distribution shifts the failure initiation point transfer from the core to the surface. Therefore, in order to obtain maximum gain in fatigue resistance, the hardness distribution should be kept in a certain range depending on the thickness and size of the specimen [45]. Core microstructure is also one of these performances. Lower carbon content of core increases the fatigue resistance, particularly due to the enlarged compressive residual stresses at the surface, compared with the cases of higher carbon content [46]. The refinement of austenitic grain size is also one of these performances, which results in a fine martensitic structure and/or reduced size and density of micro cracks in the structure produce better fatigue resistance [47, 48].

Predicting and preventing defects after quenching is most important for manufacturing mechanical parts. To date, these deficiencies have been overcome by the experience and intuition of engineers. Furthermore, along with recent advances in

numerical analysis technology and computers, simulations of phase transformation and thermal / mechanical behavior in the quenching process were conducted simulation.

Many factors such as carburizing time and temperature during the various stages of a carburizing process affect the performance above [49]. It is necessary to determine the relationship between the carburizing process factors and the material performances. It is very important to select the proper carburizing and quenching condition but it is difficult to decide the compromise between maximum hardness and minimum distortion. Computer simulation is very useful for the determination of the quenching condition to obtain the optimum quality. The application of "metallo-thermo-mechanical" theory is capable of describing the interaction among temperature field, stress/deformation field and microstructure changes in quenching.

It is expected that various problems in the heat treatment process will be elucidated by the technology. However, most simulation codes so far focused on phase transformation, residual stress and deformation that occurred inside the material, the effect of the heat transfer behavior of the coolant used for quenching on the material there are not enough studies that take into consideration. Also, with respect to complicated geometric models such as gears, some simulation is performed by cutting out a part, and almost no simulation of the whole model is performed. Measurement of residual stress on the part surface by X-ray diffraction is the mainstream for evaluating residual stress. For the measurement of the internal residual stress in a component having a plurality of metallic structures such as a quenched material, it may have significant significance in the strength evaluation of the part, and development of a new residual stress evaluation technique is expected there.

1.2 Transformation plasticity behavior

Steel and iron are the most important materials which are widely used in different purposes such as building structures, automobile, railway and ship industries etc. Steel manufacturers and automakers are mostly concentrated on the fuel efficiency, reducing the weight and improving the quality of the products. Therefore, it is necessary to

improve the mechanical properties of steels and products. The properties of metallic materials can be changed during heat treatment such as welding or quenching process. In these processes, the material is exposed to high temperature or heat generated during the processing. In this case, if the temperature is not uniformly distributed, thermal stress will generate or the residual stress existence in materials, the shape of materials will change by plastic deformation [3, 50]. During heat treatment, the relations between temperature, stress/strain and microstructure called coupling effects are very complex. In particular, transformation plasticity behavior with the nucleation and growth during phase transformation is necessary to know in detail in both experiment and simulation for which give a significant impact on the relationship of stress-strain of inelastic in the heat treatment process. The research about transformation plasticity has been conducted and theoretically studied by now [51]. For instance, experiment for identification of transformation plasticity of pearlite transformation by the tensile test is being carried out. However, few kinds of materials are identified, because the experiments must be repeated under various loads for research on transformation plasticity. The condition of the experiments requires rapid cooling for transformation plasticity of bainite transformation and martensitic transformation, therefore, rare attention is being paid to the experiment research.

As early as the last century, scholars discovered the phenomenon of phase transformation plasticity during the experiments. During the experiments, even the external stress applied to the sample does not exceed the yield strength of the weak phase, the strain increase during the continuous cooling process is greater than that without stress. With the applied stress is greater, it results the larger variable, and the strain does not disappear after the load is removed, it is actually an irreversible plastic deformation. This deformation is not the same as the classical plastic deformation. The classical plastic deformation requires an applied load exceeding the yield strength to produce irreversible plastic deformation, and the transformation plasticity can be produced when the stress is lower than the yield strength. Transformation plasticity has

two basic characteristics: first, it occurs with organizational transformation. Second, the applied stress is not required to reach or even the weak phase yield strength.

Lambers experimentally studied the role of austenitization and plastic pre-deformation on isothermal bainite and martensitic transformation behavior of low alloy steel. According to the test results, the austenitization conditions strongly affect the isothermal bainitic and martensitic transformations and the plastic pre-deformations at high austenitization temperature accelerated the isothermal phase transformation, but at low austenitization temperature the acceleration was not happened [52, 53]. The effect of austenite grain size on the kinetics of upper and lower bainite transformation of low alloy steel was reported by Lee et al. [54]. The transformation rate of upper bainite increased with reduction of austenite grain size and the transformation rate of lower bainite is independent of austenite grain size. The effect of stress and strain on martensitic transformation plasticity was investigated by Liu with tensile and compressive loading system. Here, the transformation plasticity coefficient increases with increases in applied stress, but when the applied stress reached to the yield stress, the transformation plasticity coefficient is constant even the applied stress increased [55]. The effect of compressive deformation of austenite on the isothermal bainite/ferrite transformation showed that the increases of deformation caused reduction on the value of ferrite bainite transformation [56]. The stress-dependent phase transformation and transformation induced plasticity were tested and modelled with simple experiments such as uniaxial tensile or torsional tests, and using the obtained results under constant temperature and loading, the material behavior under time-dependent conditions can be tested [57].

At present, there are two main explanation mechanisms for transformation plasticity: Greenwood-Johnson mechanism and Magee mechanism [58, 59].

The mechanism of Greenwood-Johnson is currently a widely used theoretical model. The mechanism considers that the internal stress caused by the specific volume change or the applied stress will cause plastic deformation of the weak phase of the material

during the phase transformation, and the calculation is derived based on the plastic flow theory and the yield criterion. Transformation plasticity is due to standard, dislocation-induced plasticity at the microscopic scale in the weaker, mother-phase (that prevailing at high temperatures, with a generally much lower yield stress). Microscopic plasticity arises from the difference of specific volume between the phases coexisting during the transformation (volumetric part of the transformation strain), which generates internal stresses of sufficient magnitude to induce plasticity in the weaker one. The effect occurs even in the absence of external stress; but such a stress, when present, takes advantage of the internal "transformation-induced weakness" of the material to deform it plastically. An analytical formula for the transformation plasticity induced by phase transformation. In later research, the equations of the sum are extended to study the transformation plasticity under high stress state [60-62]. It is found that the transformation plasticity strain exhibits a non-linear change with the stress when the stress approaches the yield strength of the weak phase.

The Magee mechanism believes that during the transformation of martensite, the preferred orientation of the new phase leads to the generation of phase transformation plasticity, because the preferred orientation of the new phase minimizes the total energy of the system in this state. If the orientations in the polycrystalline material are randomly selected during the phase transition, the resulting macroscopic volume changes are the same in all directions. However, when there is an applied stress, the orientation probability of some orientations increases, and the martensite sheets are preferentially generated upward in these positions, resulting in transformation plasticity. And a microstructure-based model is proposed to explain the bainite transformation plasticity phenomenon under external force by means of the orientation relationship between the face-centered cubic structure and the body-centered cubic structure [60]. (In this interpretation the expression "transformation plasticity" is somewhat inappropriate, since the transformation strain responsible for the effect is of essentially pseudo-elastic, reversible nature; but the wording is classical).

1.3 Simulation in carburizing and quenching

The thermo-mechanical behavior of materials undergoing a solid-solid phase transformation has been largely investigated experimentally and numerically. The transformation plasticity behavior under uniaxial loading have experimentally studied by many researchers with different materials [63-73]. Simon and Inoue have numerically analyzed the effect of applied tensile stress during pearlite phase transformation for the eutectoid carbon steel [65, 68-70]. Kim numerically analyzed the thermo-elastic plastic constitutive equation of Leblond, which accounts for the transformation plasticity in welding, has been carried out for finite element analysis [74-76]. The thermo-elastic free energy with the temperature-dependent material constants has been employed together with the relation of the transformation plastic flow rule between the additive decomposition of the rate of deformation and the multiplicative decomposition of the deformation gradient [76]. Furthermore, phase-field method, a computational technique, has been used to simulate the microstructure evolution during various phase transformations [77-80].

Recently, computer techniques and simulation software for heat treatment and machining processes are introduced with a high performance and relatively low cost. In addition, by high-performance computer, the numerical analysis techniques increased and the analysis software for heat treatment simulations are improved. For example, Idea Map company developed the finite element analysis software (COSMAP) based on transformation, thermal and mechanical theory. It can analysis complex coupled problem in the heat treatment process, such as temperature, diffusion, phase transformation stress and strain. However, the simulation analysis requires various materials data, rare attention is being paid to resolve this problems, and a good accuracy analysis cannot be achieved. Also US SFTC Inc. has extended the machining simulation software "DEFORM" to "DEFORM-HT" for heat treatment analysis. There are many products such as welding and heat treatment analysis software "SYSWELD" of French ESI Company which is used in the actual manufacturing process. In addition, Abaqus

from DASSAULT SYSTEMES Company provides users with an extensive array of user subroutines that allow them to adapt Abaqus to their particular analysis requirements. In order to increase the functionality of several Abaqus capabilities, many user subroutines which they furnish an extremely powerful and flexible tool for analysis are provided.

1.4 Optimization design

The experimental design is based on probability theory and mathematical statistics, and it is a scientific method to study and deal with the relationship between multi-factor and response variables. Through the experimental design method, reasonable and effective sample points can be extracted, so that the researchers can obtain the unbiased processing effect and the estimation of the test error when performing statistical analysis on the test results, so as to make a correct and effective judgment.

The experimental design was derived from agricultural production, analyzing the different ratios of phosphorus and nitrogen fertilizers, and the effect on wheat yield, so as to find the optimal fertilization ratio to increase the yield per unit of wheat. After nearly a hundred years of development, the application design has been extended to various fields of daily life. The experimental design was originally applied only in physical experiments. After development, it has been widely used in non-physical tests. The experimental design method is also the first few have evolved into a variety of experimental design methods. The following are common test design methods.

1.4.1 DOE full factorial

The DOE full factorial is to test and evaluate all combinations of all factors at all levels, allowing any number of factors and levels to be fully combined with the experimental design, taking into account all possible test conditions. The biggest advantage of the DOE full factorial is that the amount of information is large, and the main effect size of each experimental factor and the interaction effect between the various factors can be accurately estimated, and the influence degree of each factor on the index can be evaluated, and the factor number is applied. Where there are not many

levels, the reliability of the analysis can be obtained. With increasing the number of factors and the number of levels, the number of experiments required will multiply. Three factors and three levels of test design requires 27 trials. Equation 2.5 is the formula for calculating the number of full factor tests. Equation 1 is the formula for calculating the number of full factor tests.

$$f = n_1 \times n_2 \times n_i \times \cdots \times n_m \tag{1}$$

Where n_i is the number of levels of the i-th factor, and m is the number of factors.

1.4.2 Orthogonal design

Orthogonal test design is the main test method for researching and processing multi-factor tests. According to the principle of orthogonality, a representative test point is selected from the comprehensive test. Due to the balanced distribution of factors and levels, and uniform distribution of data points, it is widely used in various fields of daily life. The orthogonal table is a mathematical form constructed by mathematical theory and is the basic tool of orthogonal experimental design. The test results are statistically analyzed by corresponding range analysis, variance analysis and regression analysis.

1.4.3 Topology optimization

Topology optimization (TO) is a mathematical method that optimizes material layout within a given design space, for a given set of loads, boundary conditions and constraints with the goal of maximizing the performance of the system. TO is different from shape optimization and sizing optimization in the sense that the design can attain any shape within the design space, instead of dealing with predefined configurations.

The conventional TO formulation uses a finite element method (FEM) to evaluate the design performance. The design is optimized using either gradient-based mathematical programming techniques such as the optimality criteria algorithm and the method of moving asymptotes or non-gradient-based algorithms such as genetic algorithms.

Topology Optimization has a wide range of applications in aerospace, mechanical, bio-chemical and civil engineering. Currently, engineers mostly use TO at the concept

level of a design process. Due to the free forms that naturally occur, the result is often difficult to manufacture. For that reason, the result emerging from TO is often fine-tuned for manufacturability. Adding constraints to the formulation in order to increase the manufacturability is an active field of research. In some cases, results from TO can be directly manufactured using additive manufacturing; TO is thus a key part of design for additive manufacturing.

1.4.4 Genetic algorithm

In 1950, Alan Turing proposed a "learning machine" which would parallel the principles of evolution [81]. Computer simulation of evolution started as early as in 1954 with the work of Nils Aall Barricelli, who was using the computer at the Institute for Advanced Study in Princeton, New Jersey [82, 83]. His 1954 publication was not widely noticed. Starting in 1957 [84], the Australian quantitative geneticist Alex Fraser published a series of papers on simulation of artificial selection of organisms with multiple loci controlling a measurable trait. From these beginnings, computer simulation of evolution by biologists became more common in the early 1960s, and the methods were described in books by Fraser and Burnell (1970) and Crosby (1973) [85]. Fraser's simulations included all of the essential elements of modern genetic algorithms. In addition, Hans-Joachim Bremermann published a series of papers in the 1960s that also adopted a population of solution to optimization problems, undergoing recombination, mutation, and selection. Bremermann's research also included the elements of modern genetic algorithms. Other noteworthy early pioneers include Richard Friedberg, George Friedman, and Michael Conrad. Many early papers are reprinted by Fogel (1998).

Although Barricelli, in work he reported in 1963, had simulated the evolution of ability to play a simple game [86], artificial evolution became a widely recognized optimization method as a result of the work of Ingo Rechenberg and Hans-Paul Schwefel in the 1960s and early 1970s – Rechenberg's group was able to solve complex engineering problems through evolution strategies[84-86]. Another approach was the

evolutionary programming technique of Lawrence J. Fogel, which was proposed for generating artificial intelligence. Evolutionary programming originally used finite state machines for predicting environments, and used variation and selection to optimize the predictive logics. Genetic algorithms in particular became popular through the work of John Holland in the early 1970s, and particularly his book Adaptation in Natural and Artificial Systems (1975). His work originated with studies of cellular automata, conducted by Holland and his students at the University of Michigan. Holland introduced a formalized framework for predicting the quality of the next generation, known as Holland's Schema Theorem. Research in GAs remained largely theoretical until the mid-1980s, when The First International Conference on Genetic Algorithms was held in Pittsburgh, Pennsylvania.

In computer science and operations research, a genetic algorithm (GA) is a metaheuristic inspired by the process of natural selection that belongs to the larger class of evolutionary algorithms (EA). Genetic algorithms are commonly used to generate high-quality solutions to optimization and search problems by relying on bio-inspired operators such as mutation, crossover and selection [87]. John Holland introduced Genetic Algorithm (GA) in 1960 based on the concept of Darwin's theory of evolution; afterwards, his student Goldberg extended GA in 1989.

Genetic Algorithm has been used extensively "as a powerful tool to solve various optimization problems such as integer nonlinear problems (INLP)" [88]. "GA is one of the meta-heuristics that has been frequently utilized to find near-optimum solutions of many combinational problems" [87] . In a genetic algorithm, a population of candidate solutions (called individuals, creatures, or phenotypes) to an optimization problem is evolved toward better solutions. Each candidate solution has a set of properties (its chromosomes or genotype) which can be mutated and altered; traditionally, solutions are represented in binary as strings of 0s and 1s, but other encodings are also possible.

The evolution usually starts from a population of randomly generated individuals, and is an iterative process, with the population in each iteration called a generation. In

each generation, the fitness of every individual in the population is evaluated; the fitness is usually the value of the objective function in the optimization problem being solved. The more fit individuals are stochastically selected from the current population, and each individual's genome is modified (recombined and possibly randomly mutated) to form a new generation. The new generation of candidate solutions is then used in the next iteration of the algorithm. Commonly, the algorithm terminates when either a maximum number of generations has been produced, or a satisfactory fitness level has been reached for the population.

A typical genetic algorithm requires:

(1) Genetic representation of the solution domain,

(2) A fitness function to evaluate the solution domain.

A standard representation of each candidate solution is as an array of bits. Arrays of other types and structures can be used in essentially the same way. The main property that makes these genetic representations convenient is that their parts are easily aligned due to their fixed size, which facilitates simple crossover operations. Variable length representations may also be used, but crossover implementation is more complex in this case. Tree-like representations are explored in genetic programming and graph-form representations are explored in evolutionary programming; a mix of both linear chromosomes and trees is explored in gene expression programming.

Once the genetic representation and the fitness function are defined, a GA proceeds to initialize a population of solutions and then to improve it through repetitive application of the mutation, crossover, inversion and selection operators.

1.5 Purpose and composition of this thesis

Along with advances in science and technology, automobiles are evolving towards light weight and low energy consumption. Recent improvements in high performance and automation of various machines are remarkable, the use and perception of weight saving of components, cost reduction, high precision of processing and surface hardening heat treatment technology of steel are increasing not only in Japan but also

in various countries around the world. The object of these processing techniques is to improve various functions such as wear resistance and fatigue strength. However, since the structure and the crystal structure of the steel material change during the heat treatment, phase transformation occurs by quenching the austenitized steel material, the martensite is present in the vicinity of the surface, and the metallic structure such as bainite and pearlite are formed. Since the density of this metallographic structure is different for each tissue, the transformation stress occurs due to the difference in volume between the surface and the inside, and if a stress is externally applied during the phase transformation, large transformation plasticity occurs even if it is below the yield stress at that temperature. This transformation plastic strain is a strain equal to or greater than the thermal strain and the transformation strain and has a great influence on the strain control of the heat treated part. In addition, strain control of heat-treated parts has a great influence on factors such as heat treatment process conditions, quench coolant selection, etc. Optimum design of heat treatment process is expected while grasping the transformation plasticity of the material.

As shown in Fig.1-4, this thesis proposes a new transformation plasticity theory in heating stage. In consideration of material properties, oil for quenching, process influencing factors, etc., the experimental design method, simulation and experimental verification was used. Optimized design for carburizing and quenching process of steel 20MnCrS5 was carried out.

This thesis consists of 6 chapters. In the first chapter, after describing the research background and necessity of this thesis, the purpose of the research, contents of the research and composition of the paper are shown. In the second chapter, the material properties are calculated, a new transformation plasticity theory applied to the austenite transformation is proposed and experimentally verification is carried out simultaneously. In the third chapter, heat treatment of round bars considering transformation plasticity in the carburizing quenching process by software COSMAP was simulated and it is proved that simulation accuracy is improved. In chapter 4,

simulation and experimental verification of total 27 heat treatment process conditions considering heat treatment process condition, selection of quenching oil and gear orientation during quenching are used. In addition, a multi-purpose evaluation of hardness, residual stress and deformation of gears was used to the experimental design method and an optimal process for carburizing and quenching of gears was designed. In chapter 5, it was demonstrated that by optimum carburizing quenching process, fatigue strength of the test piece is increased while maintaining the surface hardness. Chapter 6 summarizes the paper and briefly summarizes the conclusions obtained from each chapter.
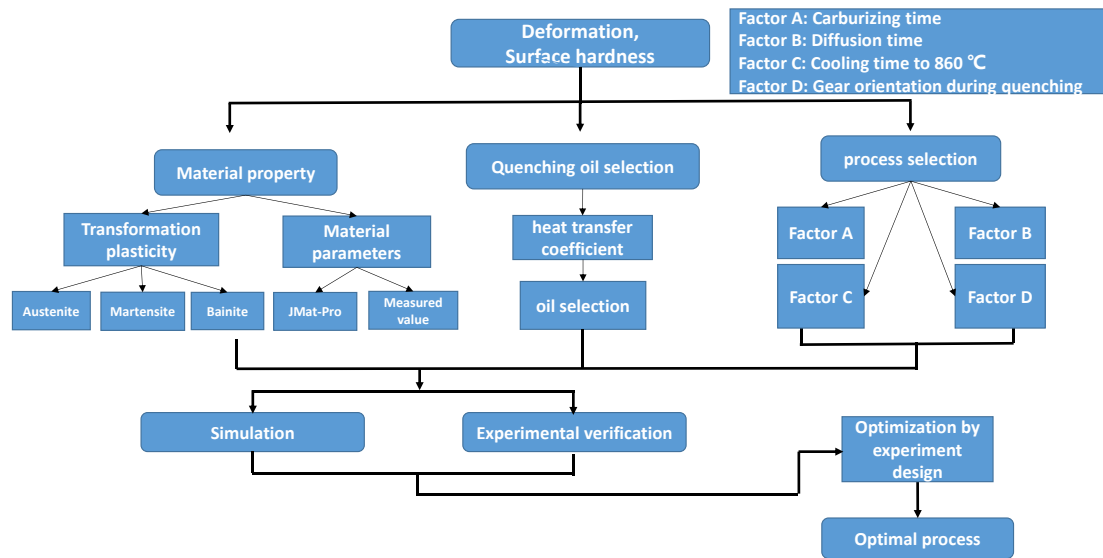

Fig. 1-4 Outline of the thesis

References

[1] **Zhao, H., Zhang, R. and Bin, Z.,** "A Review of Automotive Lightweight Technology," *2018 International Conference on Mechanical, Electronic, Control and Automation Engineering (MECAE 2018)*, 2018.

[2] **Wagner, F. T., Lakshmanan, B. and Mathias, M. F.,** "Electrochemistry and the future of the automobile," *The Journal of Physical Chemistry Letters,* 2010, vol. 1, no. 14, pp. 2204-2219.

[3] **Mukai, R. and Ju, D.-Y.,** "Simulation of carburizing-quenching of a gear. Effect of carbon content on residual stresses and distortion," *Journal de Physique IV (Proceedings)*, 2004, vol. 120, pp. 489-497: EDP sciences.

[4] **Wise, J., Matlock, D. and Krauss, G.,** "Microstructure and fatigue resistance of carburized steels," *Heat Treating: Proceedings of the 20th Conference, K. Funatani and GE Totten (Eds.), ASM International, Materials Park, Ohio*, 2001, vol. 2, pp. 1152-1161.

[5] **Kim, H.-J. and Kweon, Y.-G.,** "High cycle fatigue behavior of gas-carburized medium carbon Cr-Mo steel," *Metallurgical and Materials Transactions A,* 1996, vol. 27, no. 9, pp. 2557-2563.

[6] **Bensely, A., Venkatesh, S., Lal, D. M., Nagarajan, G., Rajadurai, A. and Junik, K.,** "Effect of cryogenic treatment on distribution of residual stress in case carburized En 353 steel," *Materials Science and Engineering: A,* 2008, vol. 479, no. 1-2, pp. 229-235.

[7] **Bataev, I., Golkovskii, M., Bataev, A., Losinskaya, A., Dostovalov, R., Popelyukh, A. and Drobyaz, E.,** "Surface hardening of steels with carbon by non-vacuum electron-beam processing," *Surface and Coatings Technology,* 2014, vol. 242, pp. 164-169.

[8] **Sugianto, A., Narazaki, M., Kogawara, M., Shirayori, A., Kim, S.-Y. and Kubota, S.,** "Numerical simulation and experimental verification of carburizing-quenching process of SCr420H steel helical gear," *Journal of Materials Processing*

Technology, 2009, vol. 209, no. 7, pp. 3597-3609.

[9] **Cho, J., Kang, W., Kim, M., Lee, J., Lee, Y. and Bae, W.,** "Distortions induced by heat treatment of automotive bevel gears," *Journal of Materials Processing Technology,* 2004, vol. 153, pp. 476-481.

[10] **Townsend, D. P. and Zaretsky, E. V.,** "Effect of shot peening on surface fatigue life of carburized and hardened AISI 9310 spur gears," SAE Technical Paper0148-7191, 1988.

[11] **Kenda, J., Duhovnik, J., Tavčar, J. and Kopač, J.,** "Abrasive flow machining applied to plastic gear matrix polishing," *The International Journal of Advanced Manufacturing Technology,* 2014, vol. 71, no. 1-4, pp. 141-151.

[12] **Acht, C., Clausen, B., Hoffmann, F. and Zoch, H. W.,** "Simulation of the distortion of 20MnCr5 parts after asymmetrical carburization," *Materialwissenschaft und Werkstofftechnik: Entwicklung, Fertigung, Prüfung, Eigenschaften und Anwendungen technischer Werkstoffe,* 2006, vol. 37, no. 1, pp. 152-156.

[13] **Miao, S., Ju, D.-Y., Chen, Y. and Liu, Y.-Q.,** "Optimization Based on Orthogonal Experiment Design and Numerical Simulation for Carburizing Quenching Process of Helical Gear," *Materials Performance and Characterization,* 2018, vol. 7, no. 6, pp. 66-79.

[14] **Stöbener, D., Acht, C., Zoch, H.-W. and Goch, G.,** "Distortion measurements of cylindrical 20MnCr5 discs during quenching in oil," *HTM Härtereitechnische Mitteilungen,* 2007, vol. 62, no. 4, pp. 157-162.

[15] **MacKenzie, D., Li, Z. and Ferguson, B. L.,** "Effect of quenchant flow on the distortion of carburized automotive pinion gears," *HTM Härtereitechnische Mitteilungen,* 2008, vol. 63, no. 1, pp. 15-21.

[16] **Christ, H. J.,** "Experimental characterization and computerbased description of the carburization behaviour of the austenitic stainless steel AISI 304L," *Materials and corrosion,* 1998, vol. 49, no. 4, pp. 258-265.

[17] **Rudnev, V., Loveless, D. and Cook, R. L.**, *Handbook of induction heating*. : CRC

press, 2017.

[18] **Ju, D.-Y., Sahashi, M., Omori, T. and Inoue, T.**, "Residual stresses and distortion of a ring in quenching-tempering process based on metallo-thermo-mechanics," ASM International, Materials Park, OH (United States)1996.

[19] **Moiseev, B., Brunzel', Y. M. and Shvartsman, L.**, "Kinetics of carburizing in an endothermal atmosphere," *Metal Science and Heat Treatment,* 1979, vol. 21, no. 6, pp. 437-442.

[20] **Stolar, P. and Prenosil, B.**, "Kinetics of Transfer of Carbon from Carburizing and Carbonitriding Atmospheres," *Kovove Mater.,* 1984, vol. 22, no. 5, p. 7.

[21] **Goldstein, J. and Moren, A.**, "Diffusion modeling of the carburization process," *Metallurgical Transactions A,* 1978, vol. 9, no. 11, pp. 1515-1525.

[22] **Munts, V. and Baskakov, A.**, "Mass exchange in carburization and decarburization of steel," *Metal Science and Heat Treatment,* 1983, vol. 25, no. 2, pp. 98-102.

[23] **Rimmer, K., Schwarz-Bergkampf, E. and Wunning, J.**, "Surface Reaction Rate in Gas Carburizing," *Haerterei-Technische Mitteilungen,* 1975, vol. 30, no. 3, pp. 152-160.

[24] **Munts, V. and Baskakov, A.**, "Rate of carburizing of steel," *Metal Science and Heat Treatment,* 1980, vol. 22, no. 5, pp. 358-360.

[25] **Ågren, J.**, "A revised expression for the diffusivity of carbon in binary Fe-C austenite," *Scripta metallurgica,* 1986, vol. 20, no. 11, pp. 1507-1510.

[26] **Harris, F.**, "Case depth—an attempt at a practical definition," *Metal Progress,* 1943, vol. 44, no. 2, pp. 265-272.

[27] **Lindig, B. A. and Rodgers, M. A.**, "Rate parameters for the quenching of singlet oxygen by water - soluble and lipid - soluble substrates in aqueous and micellar systems," *Photochemistry and Photobiology,* 1981, vol. 33, no. 5, pp. 627-634.

[28] **Fila, M. and Hulshof, J.**, "A note on the quenching rate," *Proceedings of the American Mathematical Society,* 1991, vol. 112, no. 2, pp. 473-477.

[29] **Apple, C. and Krauss, G.,** "Microcracking and fatigue in a carburized steel," *Metallurgical Transactions,* 1973, vol. 4, no. 5, pp. 1195-1200.

[30] **Murao, Y. and Sugimoto, J.,** "Correlation of heat transfer coefficient for saturated film boiling during reflood phase prior to quenching," *Journal of Nuclear Science and Technology,* 1981, vol. 18, no. 4, pp. 275-284.

[31] **Baker, T. and Harrison, W.,** "Overheating and burning in steel castings," *Metals Technology,* 1975, vol. 2, no. 1, pp. 201-205.

[32] **Jatczak, C. F.,** "Retained Austenite and its Measurement by X-ray Diffraction," *SAE Transactions,* 1980, pp. 1657-1676.

[33] **Banerjee, R.,** "Effect of room temperature aging on low temperature transformation of retained austenite," *Journal of Heat Treating,* 1984, vol. 3, no. 4, pp. 353-355.

[34] **Gregorutti, R., Sarutti, J. and Sikora, J.,** "Microstructural stability of austempered ductile iron after sub-zero cooling," *Materials science and technology,* 2003, vol. 19, no. 6, pp. 831-835.

[35] **Hoffmann, F.,** "Residual austenite, measurement and influencing; effect on mechanical properties," *Materialen(Netherlands),* 1997, vol. 4, pp. 31-34.

[36] **Grosch, J. and Schwarz, O.,** "Retained austenite and residual stress distribution in deep cooled carburized microstructures," *International Journal of Fatigue,* 1997, vol. 4, no. 19, p. 354.

[37] **Liu, X., Tian, W., Xu, W., Liang, W. and Xu, Z.,** "Wear resistance of TiAl intermetallics by plasma alloying and plasma carburization," *Surface and Coatings Technology,* 2007, vol. 201, no. 9-11, pp. 5278-5281.

[38] **Bensely, A., Prabhakaran, A., Mohan Lal, D. and Nagarajan, G.,** "Enhancing the wear resistance of case carburized steel (En 353) by cryogenic treatment," *Cryogenics,* 2005, vol. 45, no. 12, pp. 747-754.

[39] **Bammann, D., Prantil, V., Kumar, A., Lathrop, J., Mosher, D., Callabresi, M., Jou, H., Lusk, M., Krauss, G., and Elliot, B.**, "Development of a carburizing and

quenching simulation tool: a material model for carburizing steels undergoing phase transformations," *Proceedings of the 2nd International Conference on Quenching and the Control of Distortion*, 1996, pp. 367-375.

[40] **Greenwood, G. W.,** "The deformation of metals under small stresses during phase transformations," *Mathematical and Physical Sciences,* 1965, vol. 283, no. 1394, pp. 403-422.

[41] **Leblond, J.-B.,** "Mathematical modelling of transformation plasticity in steels I: case of ideal-plastic phases," *International journal of plasticity,* 1989, vol. 5, no. 6, pp. 551-572.

[42] **Genel, K. and Demirkol, M.,** "Effect of case depth on fatigue performance of AISI 8620 carburized steel," *International Journal of Fatigue,* 1999, vol. 21, no. 2, pp. 207-212.

[43] **Zhang, J., Zhang, Q., Wu, C., Xu, Z. and Lyu, S.,** "Experimental application of pitting formation for 20MnCr5 carburized gear tooth," *International Journal of Precision Engineering and Manufacturing,* 2014, vol. 15, no. 5, pp. 899-903.

[44] **Boniardi, M., D'Errico, F. and Tagliabue, C.,** "Influence of carburizing and nitriding on failure of gears–A case study," *Engineering Failure Analysis,* 2006, vol. 13, no. 3, pp. 312-339.

[45] **Asi, O., Can, A. Ç., Pineault, J. and Belassel, M.,** "The relationship between case depth and bending fatigue strength of gas carburized SAE 8620 steel," *Surface and Coatings Technology,* 2007, vol. 201, no. 12, pp. 5979-5987.

[46] **Cameron, T., Diesburg, D. E. and Kim, C.,** "Fatigue and overload fracture of carburized steels," *JOM,* 1983, vol. 35, no. 7, pp. 37-41.

[47] **Preston, S.,** "Bending fatigue strength of carburising steel SS 2506," *Materials science and technology,* 1991, vol. 7, no. 2, pp. 105-110.

[48] **Asada, N., Yamamoto, Y., Shimatani, K., Honkawa, S. and Miyake, M.,** "Particle size of fine grain WC by the 'continuous direct carburizing process'," *Metal Powder Report,* 1990, vol. 45, no. 1, pp. 60-64.

[49] **Mukai, R., Matsumoto, T., Ju, D.-Y., Suzuki, T., Saito, H. and Ito, Y.,** "Modeling of numerical simulation and experimental verification for carburizing-nitriding quenching process," *Transactions of Nonferrous Metals Society of China,* 2006, vol. 16, pp. s566-s571.

[50] **Zhang, X., Tang, J.-Y. and Zhang, X.-R.,** "An optimized hardness model for carburizing-quenching of low carbon alloy steel," *Journal of Central South University,* 2017, vol. 24, no. 1, pp. 9-16.

[51] **Ju, D., Sahashi, M., Omori, T. and Inoue, T.**, "Residual stresses and distortion of a ring in quenching-tempering process based on metallo-thermo-mechanics," ASM International, Materials Park, OH (United States)1996.

[52] **Lambers, H.-G., Tschumak, S., Maier, H. and Canadinc, D.,** "Role of austenitization and pre-deformation on the kinetics of the isothermal bainitic transformation," *Metallurgical and Materials Transactions A,* 2009, vol. 40, no. 6, pp. 1355-1366.

[53] **Lambers, H.-G., Tschumak, S., Maier, H. and Canadinc, D.,** "On the bainitic and martensitic phase transformation behavior and the mechanical properties of low alloy 51CrV4 steel," *The International Journal of Structural Changes in Solids,* 2011, vol. 3, no. 1, pp. 15-27.

[54] **Lee, S.-J., Park, J.-S. and Lee, Y.-K.,** "Effect of austenite grain size on the transformation kinetics of upper and lower bainite in a low-alloy steel," *Scripta Materialia,* 2008, vol. 59, no. 1, pp. 87-90.

[55] **Liu, C., Yao, K.-f., Liu, Z. and Gao, G.,** "Study of the effects of stress and strain on martensite transformation: Kinetics and transformation plasticity," *Journal of computer-aided materials design,* 2000, vol. 7, no. 1, pp. 63-69.

[56] **Larn, R. and Yang, J.,** "The effect of compressive deformation of austenite on the Widmanstätten ferrite transformation in Fe–Mn–Si–C steel," *Materials Science and Engineering: A,* 1999, vol. 264, no. 1-2, pp. 139-150.

[57] **Wolff, M., Böhm, M., Löwisch, G. and Schmidt, A.,** "Modelling and testing of

transformation-induced plasticity and stress-dependent phase transformations in steel via simple experiments," *Computational materials science,* 2005, vol. 32, no. 3-4, pp. 604-610.

[58] **Magee, C. L. and Paxton, H. W.**, "Transformation kinetics, microplasticity and aging of martensite in Fe-31 Ni," CARNEGIE INST OF TECH PITTSBURGH PA1966.

[59] **Greenwood, G. W. and Johnson, R.,** "The deformation of metals under small stresses during phase transformations," *Proceedings of the Royal Society of London. Series A. Mathematical and Physical Sciences,* 1965, vol. 283, no. 1394, pp. 403-422.

[60] **Han, H. N. and Suh, D.-W.,** "A model for transformation plasticity during bainite transformation of steel under external stress," *Acta materialia,* 2003, vol. 51, no. 16, pp. 4907-4917.

[61] **Kitazono, K., Sato, E. and Kuribayashi, K.,** "Unified interpretation of internal stress superplasticity models based on thermally-activated kinetics," *Acta materialia,* 1999, vol. 47, no. 5, pp. 1653-1660.

[62] **Zwigl, P. and Dunand, D.,** "A non-linear model for internal stress superplasticity," *Acta materialia,* 1997, vol. 45, no. 12, pp. 5285-5294.

[63] **OTSUKA, T. and INouE, T.,** "Identification of transformation plasticity coefficient by four-point bending tests and some data under pearlite transformation," *Journal of the Society of Materials Science, Japan,* 2003, vol. 52, no. 10, pp. 1198-1203.

[64] **Hikida, N., Yamamoto, Y., Oshita, K. and Nagaki, S.**, "Experimental investigation of transformation plastic behavior under tensile-compressive-torsional stress in Steel," *Key Engineering Materials*, 2015, vol. 626, pp. 426-431: Trans Tech Publ.

[65] **Denis, S., Sjöström, S. and Simon, A.,** "Coupled temperature, stress, phase transformation calculation," *Metallurgical Transactions A,* 1987, vol. 18, no. 7, pp. 1203-1212.

[66] **Coret, M., Calloch, S. and Combescure, A.,** "Experimental study of the phase transformation plasticity of 16MND5 low carbon steel induced by proportional and nonproportional biaxial loading paths," *European Journal of Mechanics-A/Solids,* 2004, vol. 23, no. 5, pp. 823-842.

[67] **Taleb, L., Cavallo, N. and Waeckel, F.,** "Experimental analysis of transformation plasticity," *International journal of plasticity,* 2001, vol. 17, no. 1, pp. 1-20.

[68] **Yamaguchi, T., Wang, Z. and Inoue, T.,** "Analysis of temperature, metallic structure and stress during carburized quenching of a gear with consideration of carbon content," *Journal of the Society of Materials Science, Japan,* 1984, vol. 33, no. 375, p. 1470.1476.

[69] **Wang, Z.-G. and Inoue, T.,** "Analyses of temperature, structure and stress during quenching of steel with consideration for stress dependence of transformation kinetics," *Journal of the Society of Materials Science, Japan,* 1983, vol. 32, no. 360, p. 991.996.

[70] **Denis, S., Gautier, E., Simon, A. and Beck, G.,** "Stress–phase-transformation interactions–basic principles, modelling, and calculation of internal stresses," *Materials science and technology,* 1985, vol. 1, no. 10, pp. 805-814.

[71] **Coret, M., Calloch, S. and Combescure, A.,** "Experimental study of the phase transformation plasticity of 16MND5 low carbon steel under multiaxial loading," *International journal of plasticity,* 2002, vol. 18, no. 12, pp. 1707-1727.

[72] **Taleb, L. and Petit, S.,** "New investigations on transformation induced plasticity and its interaction with classical plasticity," *International journal of plasticity,* 2006, vol. 22, no. 1, pp. 110-130.

[73] **Gautier, E., Simon, A. and Beck, G.,** "Deformation of eutectoid steel during pearlitic transformation under tensile stress," *Strength of Metals and Alloys*: Elsevier, 1979, pp. 867-873.

[74] **Leblond, J.-B., Mottet, G. and Devaux, J.,** "A theoretical and numerical approach to the plastic behaviour of steels during phase transformations—II. Study of classical plasticity for ideal-plastic phases," *Journal of the Mechanics and Physics of*

Solids, 1986, vol. 34, no. 4, pp. 411-432.

[75] **Leblond, J.-B., Mottet, G. and Devaux, J.,** "A theoretical and numerical approach to the plastic behaviour of steels during phase transformations—I. Derivation of general relations," *Journal of the Mechanics and Physics of Solids,* 1986, vol. 34, no. 4, pp. 395-409.

[76] **Kim, J., Im, S. and Kim, H.-G.,** "Numerical implementation of a thermo-elastic–plastic constitutive equation in consideration of transformation plasticity in welding," *International journal of plasticity,* 2005, vol. 21, no. 7, pp. 1383-1408.

[77] **Yamanaka, A., Takaki, T. and Tomita, Y.,** "Elastoplastic phase-field simulation of martensitic transformation with plastic deformation in polycrystal," *International Journal of Mechanical Sciences,* 2010, vol. 52, no. 2, pp. 245-250.

[78] **Yamanaka, A., Takaki, T. and Tomita, Y.,** "Elastoplastic phase-field simulation of self-and plastic accommodations in cubic$\rightarrow$ tetragonal martensitic transformation," *Materials Science and Engineering: A,* 2008, vol. 491, no. 1-2, pp. 378-384.

[79] **Moelans, N., Blanpain, B. and Wollants, P.,** "An introduction to phase-field modeling of microstructure evolution," *Calphad,* 2008, vol. 32, no. 2, pp. 268-294.

[80] **Boettinger, W. J., Warren, J. A., Beckermann, C. and Karma, A.,** "Phase-field simulation of solidification," *Annual review of materials research,* 2002, vol. 32, no. 1, pp. 163-194.

[81] **Machinery, C.,** "Computing machinery and intelligence-AM Turing," *Mind,* 1950, vol. 59, no. 236, pp. 433-460.

[82] **Barricelli, N. A.,** "Esempi numerici di processi di evoluzione," *Methodos,* 1954, vol. 6, no. 21-22, pp. 45-68.

[83] **Barricelli, N. A.,** "Symbiogenetic evolution processes realized by artificial methods," *Methodos,* 1957, vol. 9, no. 35-36, pp. 143-182.

[84] **Fraser, A. S.,** "Simulation of genetic systems by automatic digital computers I. Introduction," *Australian Journal of Biological Sciences,* 1957, vol. 10, no. 4, pp. 484-491.

[85] **Fraser, A. and Burnell, D.,** "Computer models in genetics," *Computer models in genetics,* 1970.

[86] **Aall, B. N.,** "Numerical testing of evolution theories. Part II. Preliminary tests of performance, symbiogenesis and terrestrial life," *Symbiogenesis and terrestrial life, Acta Biotheoretica,* 1963, vol. 16, pp. 99-126.

[87] **Sadeghi, J., Sadeghi, S. and Niaki, S. T. A.,** "Optimizing a hybrid vendor-managed inventory and transportation problem with fuzzy demand: an improved particle swarm optimization algorithm," *Information Sciences,* 2014, vol. 272, pp. 126-144.

[88] **Sadeghi, J., Niaki, S. T. A., Malekian, M. R. and Sadeghi, S.,** "Optimising multi-item economic production quantity model with trapezoidal fuzzy demand and backordering: two tuned meta-heuristics," *Eur J Ind Eng,* 2016, vol. 10, no. 2, pp. 170-195.

Chapter 2 Mechanism of transformation plasticity

2.1 Introduction

In recent years, the major impact of transformation plasticity upon residual stresses and distortions resulting from thermo mechanical treatment has been emphasized by various authors [1-5]. Heat treatment is wildly used in daily life to improve the properties of metals. However, deformation often occurs after heat treatment due to the impact of transformation plasticity, which indicates that permanent strain remains after the solid-solid phase transformation, even under much smaller stress than the yield stress [6]. This impact constitutes the motivation for developing good models of transformation plasticity, to be used for accurate predictions of residual stresses and distortions in heat treatments [7].

It is widely accepted nowadays that mechanisms of transformation plasticity can be classified into two groups: weaker phased yielding and favorable variant selection. The first mechanism is that transformation plasticity is caused by volume mismatch between the stronger phase and weaker phase, which produces plasticity in the weaker phase. The second mechanism is that the transformation plasticity is due to the deviatoric part of the transformation strain of the transforming regions. when the external stress is zero the deviatoric part of the transformation strain varies randomly in direction in the material, and therefore averages out to zero; but when the external stress is nonzero, it "orients" this deviatoric part and the net result is a nonzero macroscopic strain. The above theories have been experimentally verified in the phase transformation during cooling [8, 9].

Transformation plasticity behavior with nucleation and growth during phase transformation is necessary to know in detail for which give a significant impact on the relationship of stress-strain of inelastic in the heat treatment process. When steel is strained in high temperature it shows a typical regions of hot deformation: a hardening

region characterized by an increasing dislocation density, followed by a dynamic recovery characterized by a polygonized austenite, and finally dynamic recrystallization where the build-up of dislocations leads to the nucleation and growth of recrystallized grains during the deformation until the steady state is reached where recrystallization is total and continuous [10]. This phenomenon leads to significant grain refinement. However, the above theories have not considered the effect of grain size on deformation in phase change plasticity. It is necessary to develop a model that takes into account the grain size and is suitable for any temperature.

In this chapter, a new mathematic model suitable for both high and low temperatures was developed based on the mechanism of weaker phase yielding to describe the transformation plasticity behavior of steels, which includes the influence of grain size changes on transformation plasticity behavior. The effectiveness of the new model was verified through experimental methods.

2.2 Theory of transformation plasticity

2.2.1 Constitutive Equation

Total strain rate $\dot{\varepsilon}_{ij}$ is assumed to be divided into elastic strain rate $\dot{\varepsilon}_{ij}^e$, thermal strain rate $\dot{\varepsilon}_{ij}^{th}$, phase transformation strain rate $\dot{\varepsilon}_{ij}^{tr}$, normal plastic strain rate $\dot{\varepsilon}_{ij}^{np}$ and transformation plasticity strain rate $\dot{\varepsilon}_{ij}^{tp}$ such that

$$\dot{\varepsilon}_{ij} = \dot{\varepsilon}_{ij}^e + \dot{\varepsilon}_{ij}^{th} + \dot{\varepsilon}_{ij}^{tr} + \dot{\varepsilon}_{ij}^{np} + \dot{\varepsilon}_{ij}^{tp} \tag{1}$$

Since the transformation plasticity strain is a kind of plastic strain, transformation plasticity strain rate and normal plastic strain rate are combined into total plastic strain rate $\dot{\varepsilon}_{ij}^p$ as followed.

$$\dot{\varepsilon}_{ij}^p = \dot{\varepsilon}_{ij}^{np} + \dot{\varepsilon}_{ij}^{tp} \tag{2}$$

When any phase is deformed, even if the volume fraction of the phase is constant, it is affected by the thermal strain. Therefore, the weaker phase (such as austenite) will be affected by the stronger phase (such as martensite) in transformation plasticity. The

plastic strain of weaker phase depends on stress, temperature change, plastic strain, hardening parameter, and volume of stronger phase. The yield function F_I of weaker phase I is as followed

$$F_I = F_I(\sigma_{ij}, T, \varepsilon_{Iij}^P, \kappa_I, \zeta_J), \quad (I = 1, 2, \dots, N; J = 1, 2, \dots, M) \tag{3}$$

Where σ_{ij} is the stress, T is the temperature, ε_{Iij}^P is the equivalent plastics strain of phase I, κ_I is the hardening parameter and ζ_J is the volume fraction of stronger phase J. In the case of the plastic deformation, it can obtain the following relationship.

$$\frac{\partial F_I}{\partial \sigma_{ij}} \dot{\sigma}_{ij} + \frac{\partial F_I}{\partial T} \dot{T} + \frac{\partial F_I}{\partial \varepsilon_{Iij}^P} \dot{\varepsilon}_{Iij}^P + \frac{\partial F_I}{\partial \kappa_I} \dot{\kappa}_I + \sum_{J=1}^{M} \frac{\partial F_I}{\partial \zeta_J} \dot{\zeta}_J = 0 \tag{4}$$

Therefore, the plastic strain rate $\dot{\varepsilon}_{Iij}^p$ of phase I is expressed as followed.

$$\dot{\varepsilon}_{Iij}^p = \lambda_I \frac{\partial F_I}{\partial \sigma_{ij}} = \hat{G}_I \left\{ \left(\frac{\partial F_I}{\partial \sigma_{ij}} \dot{\sigma}_{ij} + \frac{\partial F_I}{\partial T} \dot{T} \right) + \sum_{J=1}^{M} \frac{\partial F_I}{\partial \zeta_J} \dot{\zeta}_J \right\} \frac{\partial F_I}{\partial \sigma_{ij}} \tag{5}$$

$$\frac{1}{\hat{G}_I} = - \left\{ \frac{\partial F_I}{\partial \varepsilon_{Iij}^P} + \frac{\partial F_I}{\partial \kappa_I} \sigma_{ij} \right\} \frac{\partial F_I}{\partial \sigma_{ij}} \tag{6}$$

With combination of Eq. 3, Eq. 4, Eq. 5 and Eq. 6, the plasticity strain rate $\dot{\varepsilon}_{Iij}^{tp}$ of phase I and the total plasticity strain rate $\dot{\varepsilon}_{ij}^{tp}$ can be obtained as followed.

$$\dot{\varepsilon}_{Iij}^{tp} = \sum_{J=1}^{M} \hat{G}_I \frac{\partial F_I}{\partial \zeta_J} \dot{\zeta}_J \frac{\partial F_I}{\partial \sigma_{ij}} \tag{7}$$

$$\dot{\varepsilon}_{ij}^{tp} = \sum_{I=1}^{N} \xi_I \dot{\varepsilon}_{Iij}^{tp} = \sum_{I=1}^{N} \sum_{J=1}^{M} \hat{G}_I \frac{\partial F_I}{\partial \zeta_J} \dot{\zeta}_J \xi_I \frac{\partial F_I}{\partial \sigma_{ij}} \tag{8}$$

In the case of isotropic hardening material, it conform to the yield condition of Mises. The yield function F_I of phase I is as followed

$$F_I = \frac{1}{2} s_{ij} s_{ij} - \frac{1}{3} \bar{\sigma}_I^2 (\kappa_I(\bar{\varepsilon}_I^P), \zeta_J, T) \tag{9}$$

where s_{ij} is deviatoric stress, $\bar{\sigma}_I$ is the equivalent flow stress of phase I and $\bar{\varepsilon}_I^P$ is the equivalent plastic strain of phase I.

The strain hardening rate H_I' of phase I is that

$$\frac{\partial F_I}{\partial \kappa_I} = -\frac{2}{3} \bar{\sigma}_I \frac{\partial \bar{\sigma}_I}{\partial \bar{\varepsilon}_I^P} = -\frac{2}{3} \bar{\sigma}_I H_I'; \qquad (H_I' = \frac{\partial \bar{\sigma}_I}{\partial \bar{\varepsilon}_I^P}) \tag{10}$$

H_I^T is the dependence coefficient between equivalent flow stress of phase I and temperature.

$$\frac{\partial F_I}{\partial T} = -\frac{2}{3}\bar{\sigma}_I\frac{\partial \bar{\sigma}_I}{\partial T} = -\frac{2}{3}\bar{\sigma}_I H_I^T; \qquad (H_I^T = \frac{\partial \bar{\sigma}_I}{\partial T}) \tag{11}$$

H_{IJ}^{ζ} is the dependence coefficient between equivalent flow stress of phase I and volume fraction of phase J.

$$\frac{\partial F_I}{\partial \zeta_J} = -\frac{2}{3}\bar{\sigma}_I\frac{\partial \bar{\sigma}_I}{\partial \zeta_J} = -\frac{2}{3}\bar{\sigma}_I H_{IJ}^{\zeta}; \qquad (H_{IJ}^{\zeta} = \frac{\partial \bar{\sigma}_I}{\partial \zeta_J}) \tag{12}$$

Combined with Eq. 10-12, Eq. 8 can be transformed as followed

$$\dot{\varepsilon}_{ij}^{tp} = 3\sum_{I=1}^{N}\sum_{J=1}^{M}\frac{H_{IJ}^{\zeta}}{2\bar{\sigma}_I H_I'}\xi_I\dot{\zeta}_J\, s_{ij} \tag{13}$$

The grain size has a measurable effect on most of the mechanical properties. The yield strength increase with decreasing grain size. The influence of grain size on the mechanical properties is most commonly expressed in a Hall-Petch Equation [11-13].

$$\bar{\sigma}_I = \sigma_0 + k_y \cdot d^{-0.5} \tag{14}$$

Where σ_0 is the friction resistance for dislocation movement within the polycrystalline grains. k_y is a measure of the local stress needed at a grain boundary for the transmission of plastic flow. d is the average grain size. σ_0 is proved to be constant. Combined with Eq. 10-12, Eq. 13 can be transformed as followed

$$\dot{\varepsilon}_{ij}^{tp} = 3\sum_{I=1}^{N}\sum_{J=1}^{M}\frac{\partial \bar{\varepsilon}^P}{\partial \zeta_J} \cdot \frac{1}{2(\sigma_0 + k_y \cdot d^{-0.5})}\xi_I\dot{\zeta}_J\, s_{ij} \tag{15}$$

When $N = 2, M = 1$, Eq. 15 can be transformed as followed

$$\dot{\varepsilon}_{ij}^{tp} = 3\frac{\partial \bar{\varepsilon}^P}{\partial \zeta_J} \cdot \frac{1}{2(\sigma_0 + k_y \cdot d^{-0.5})}\xi\dot{\zeta} s_{ij} \tag{16}$$

When the transformation is single phase to single phase, the following formula can be obtained.

$$\xi + \zeta = 1 \tag{17}$$

Equation 16 shows below

$$\dot{\varepsilon}_{ij}^{tp} = 3\frac{\partial \bar{\varepsilon}^P}{\partial \zeta_J} \cdot \frac{1}{2(\sigma_0 + k_y \cdot d^{-0.5})}(1 - \zeta)\dot{\zeta} s_{ij} \tag{18}$$

From the Leblond model,

$$\Delta\varepsilon_{1\to2}^{th} = \Delta\varepsilon_{ij}^{T} + \varepsilon_{ij}^{tr} \tag{19}$$

$$\frac{\partial \bar{\varepsilon}^P}{\partial \zeta_J} = -\frac{2\Delta\varepsilon_{1\to2}^{th}}{1-\zeta}\ln(\zeta) \tag{20}$$

So that

$$\dot{\varepsilon}_{ij}^{tp} = 3 \frac{-\Delta\varepsilon_{1\to2}^{th}}{(\sigma_0+k_y\cdot d^{-0.5})} \ln(\zeta)\dot{\zeta}s_{ij} \tag{21}$$

When the transformation plasticity strain rate $\dot{\varepsilon}_{ij}^{tp}$ (Eq. 18) is integrated from the beginning ($\xi=0$) to the end ($\xi=1$) of the transformation, the transformation plastic strain ε_{ij}^{tp} during the transformation process can be written as:

$$\varepsilon^{tp} = 3 \int_0^1 \frac{-\Delta\varepsilon_{1\to2}^{th}}{(\sigma_0+k_y\cdot d^{-0.5})} \ln(\zeta)\dot{\zeta}s_{ij} \tag{22}$$

$$\varepsilon^{tp} = \frac{3\Delta\varepsilon_{1\to2}^{th}}{(\sigma_0+k_y\cdot d^{-0.5})} s_{ij} \tag{23}$$

When the stress is in the uniaxial direction, the transformation plasticity strain can be written as:

$$\varepsilon^{tp} = \frac{2\Delta\varepsilon_{1\to2}^{th}}{(\sigma_0+k_y\cdot d^{-0.5})} \sigma \tag{24}$$

2.2.2 Austenite transformation plasticity behavior

In austenite transformation, dynamic recrystallization leads to grain refinement. Therefore, the influence of grain size d and the measure of the local stress needed at a grain boundary for the transmission of plastic flow k_y on phase change plastic behavior cannot be ignored.

$$\varepsilon^{tp}(\sigma, k_y, d) = \frac{2\Delta\varepsilon_{1\to2}^{th}}{(\sigma_0+k_y\cdot d^{-0.5})} \sigma \tag{25}$$

2.3 Experimental procedure

The dimensions of small round bar tensile specimen used in this experiment is shown in Fig. 2-1. Distance between the target points is set to 6mm in the specimen center. The overview of the electric furnace of multipurpose thermo-mechanics load testing machine is shown in Fig. 2-2. It was designed by Tatsuo Inoue Professor and manufactured by Yonekura Mfg. Co., Ltd. The specimen is fixed to the tension rod extending to the both sides of the electric furnace. The thermocouple (platinum platinum-rhodium) is spot welded to center of the specimen surface. In order to make the specimen heated evenly, the specimen is heated by the combination of the lamp

heater and reflecting surface in the electric furnace. The experiment is controlled by a computer program. Fig. 2-3 shows an example of austenite transformation plasticity process (ATP). The specimens are heated to 950°C at a rate of 5°C/s with different low tensile stresses of 0MPa, 5MPa, 10MPa, 15MPa are started to load just before the austenite transformation initiating temperature and completed after the austenite transformation. The specimens are then slowly cooled to room temperature. It shows an example of cooling process (MTP & BTP). The specimens are heated to 950°C at a rate of 5°C/s. During cooling the different low tensile stresses of 0MPa, 10MPa, 20MPa, 30MPa are started to load just before the transformation initiating temperature. The tensile loading is followed by Table 2-1. Displacement and strain of the specimens are measured by the installed two quartz glass rod between the target points of 6mm at the specimen center. The relative distance of the quartz glass rod is measured by a displacement measuring device, a GaN green LED light which is made by the Keyence Corporation.
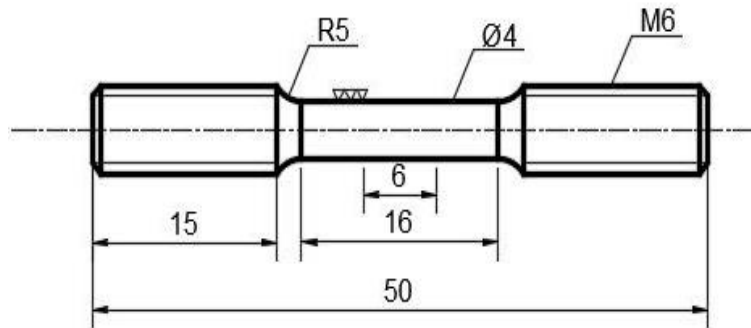
Fig. 2-1 Dimensions of specimen for experiments.
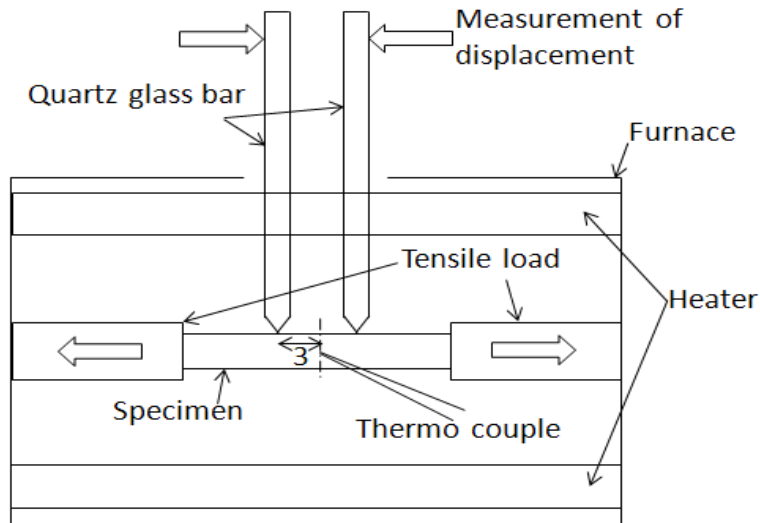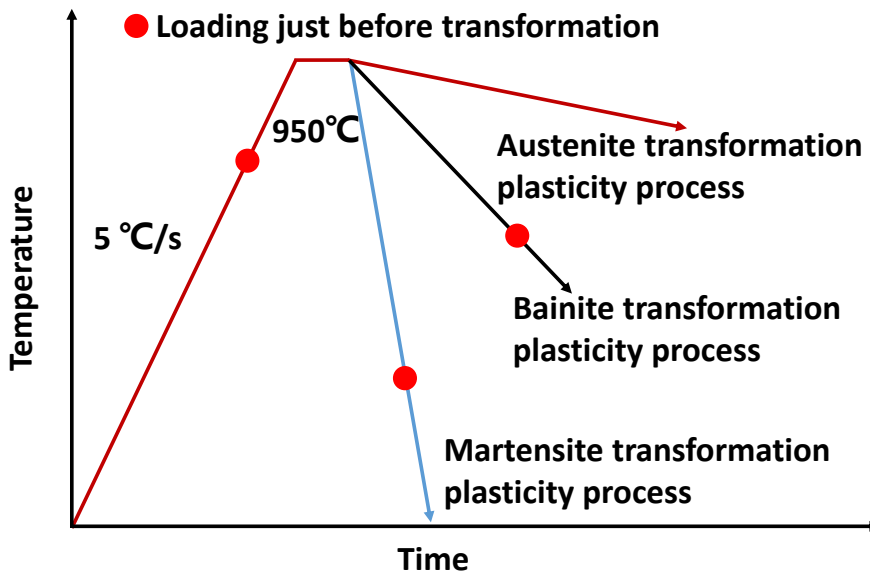
Fig. 2-2 Schematic of tensile test system

Fig. 2-3 Examples of heat treatment process

Table 2-1 Applied load of each stress equivalent

Stress (MPa)	Tensile load (N)
5	62.8
10	125.6
15	188.4
20	251.2
30	376.8

2.4 Results

2.4.1 Transformation plasticity during cooling

The specimens were heated to the austenite transformation temperature and stresses

were loaded respectively before bainite transformation and martensitic transformation. The temperature-strain diagrams are obtained by enlarging transformation as shown in Fig. 2-4. Bainite transformation occurs at around 500°C and martensitic transformation occurs at around 350°C during cooling. As the simple phase transformation occurs respectively, transformation plasticity behavior can be measureable. Compared to the stress-free, it is seen to have different significantly as the load stress increases. There are only transformation strain and thermal strain in the case of stress-free, while there is also transformation plasticity strain in the case of loading stress. Therefore, subtracting the stress-free strain from loaded stress strain is transformation plasticity strain. In this case, because load stress is under the yield stress point, normal plasticity strain does not occur.

The relationship of stress and transformation plasticity strain obtained from the experimental value is shown in Fig. 2-5. According to the Eq. 46, transformation plasticity coefficient in the martensitic transformation and bainite transformation are constant value in proportion to the stress and transformation plasticity strain. The transformation plasticity coefficients are shown in Table 2-1.
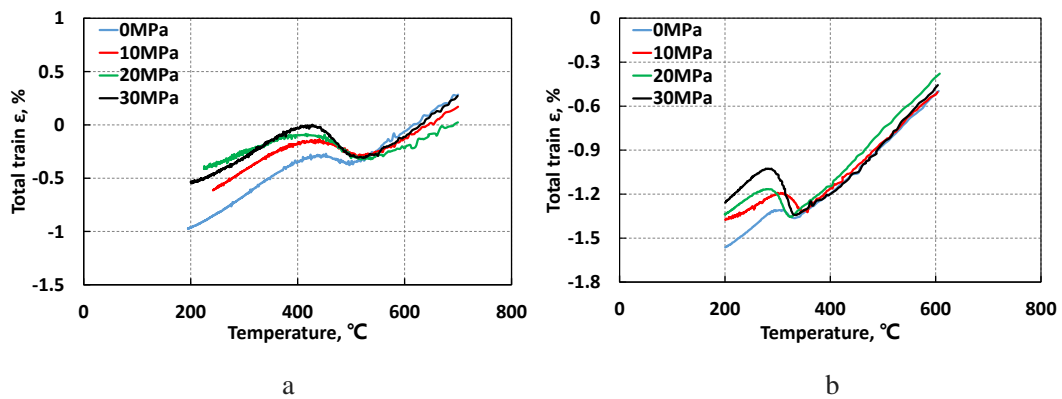

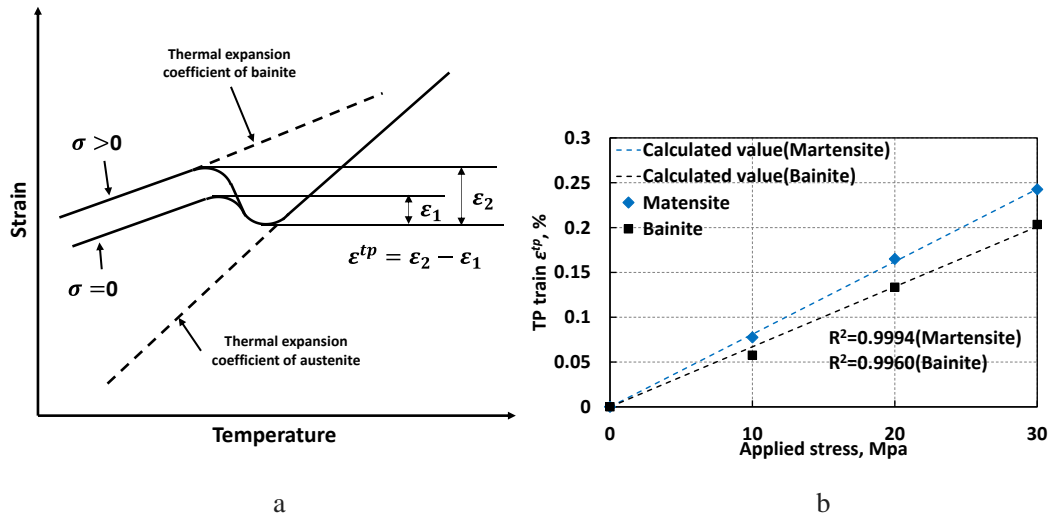Fig. 2-4 Temperature-strain diagram: (a) bainite transformation; (b) martensitic transformation

Fig. 2-5 Relation between applied stress and transformation plastic strain for materials examined

In the experiment, specimens loaded with each stress were processed, and the microstructures were observed using SEM. Using a fine cutter for cutting the specimens, the center of the specimens were machined into a half column shape as shown in Fig. 2-6 and Fig. 2-7. Because the processed specimens were very small and difficult to polish, make a pedestal with copper and polish each foundation.

The cross section of the specimens are first grounded and polished and then the surfaces of the microstructure observation points are eroded with a solution of 4% HNO_3 + 96% C_2H_5OH, the microstructures at different depth from the surface are finally observed by OM.
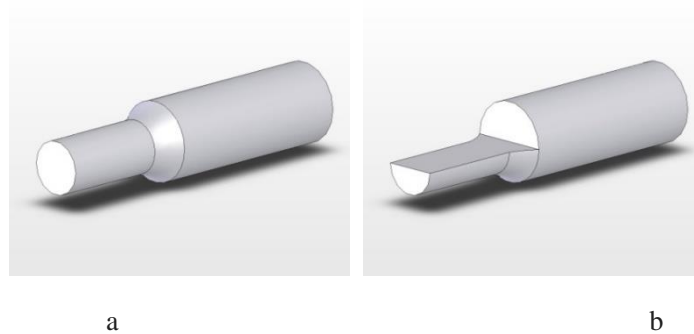
Fig. 2-6 (a) Cutting vertically (b) Cutting horizontally
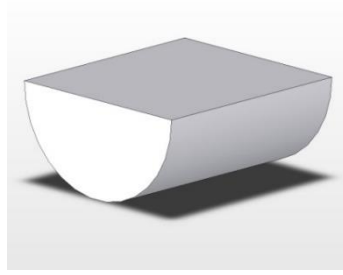
Fig.2-7 Observation part

Fig. 2-8 shows the original structure of 20MnCrS5 (China) raw material. As can be seen from Fig. 2-8(a), it mainly has ferrite and pearlite, it also contains a small amount of bainite structure. During the cooling after rolling, the ferrite precipitates along the grain boundary of the prior austenite grains, and gradually grows into a strip shape during the cooling process. In Fig. 2-8(b) the longitudinal section contains a large amount of bainite structure. Combined with Fig. 2-8(a), it is estimated that the cooling rate after rolling is about 2~4°C/s.

Fig. 2-9 shows the heat treatment process of 900°C for 2 h and then 5h to room temperature. In the process of slow cooling, a large amount of ferrite is formed, and gradually grows up in the slow cooling process, and after reaching the eutectoid transition point, pearlite is formed. As shown in Fig. 2-9(b), it can be seen that the band segregation is serious, and it is speculated that the dendrites of the raw material continuous casting billet are developed and the solidification segregation is relatively serious. Eliminate or cover up the furnace by high temperature insulation, billet rolling, large rolling deformation and fast cooling rate, but reheating occurs again when the austenite zone is slowly cooled, which requires a reasonable heat treatment process to prevent re-generation of banded segregation.

Fig. 2-10 is an image of the martensite structure obtained after the sample is extremely cold test. The sample undergoes martensite transformation at about 350°C to form lath martensite. The presence of the slat group can be clearly observed.

Fig. 2-11 shows the bainite tissue image obtained after the sample under extremely cold test. The sample undergoes a bainite transformation at about 500°C to form a small

amount of feathery bainite, carbon-free bainite and a large number of plate strip bainite.
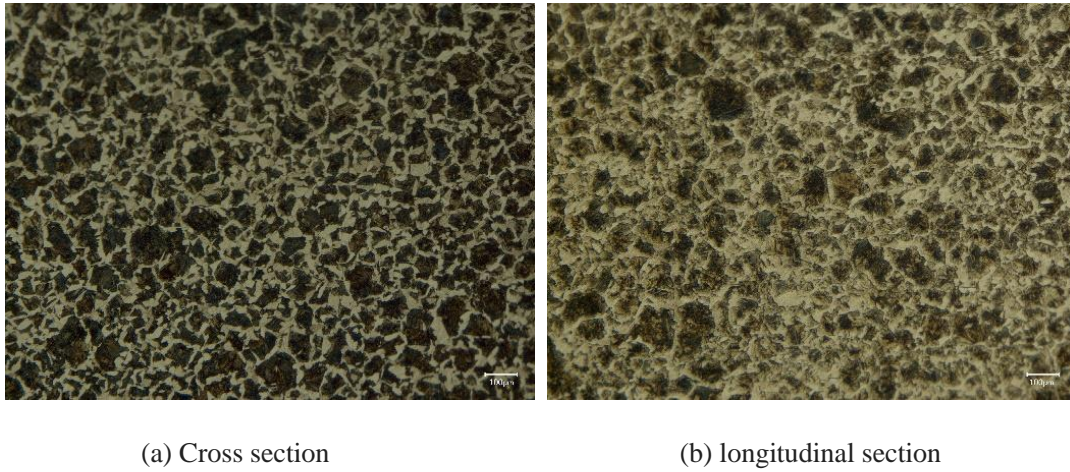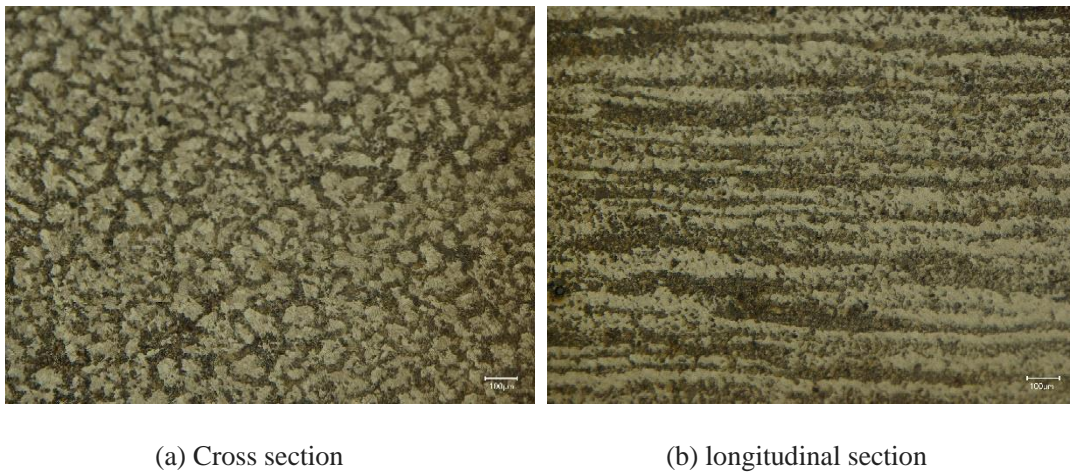

(a) Cross section   (b) longitudinal section

Fig. 2-8 Raw material of 20MnCrS5 (China)

(a) Cross section   (b) longitudinal section

Fig. 2-9 Preprocessed microstructure of 20MnCrS5 (China)

(a) Cross section   (b) longitudinal section
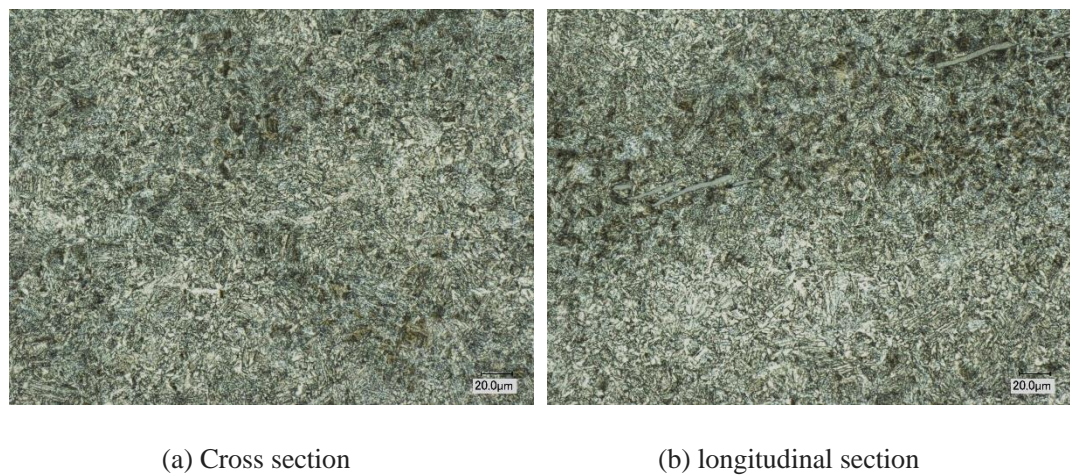
Fig. 2-10 Bainite of 20MnCrS5 (China)
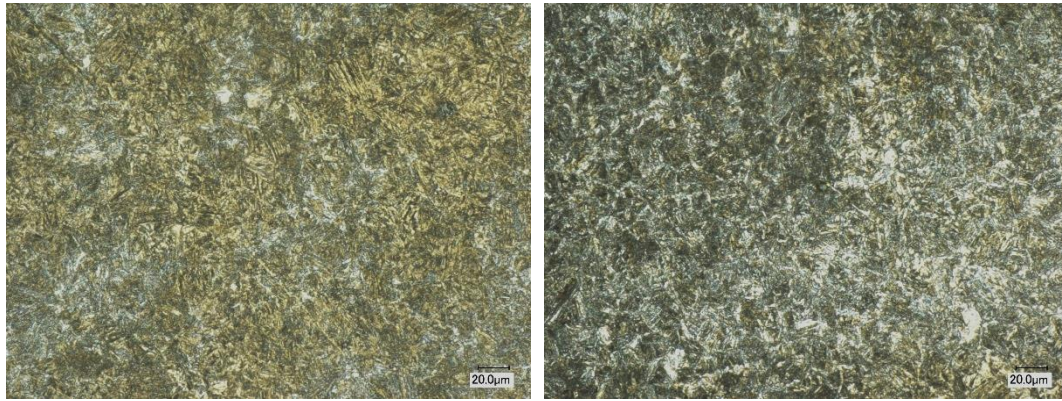
<div align="center">
(a) Cross section   (b) longitudinal section

Fig. 2-11 Martensite of 20MnCrS5 (China)
</div>

2.4.2 Austenite transformation plasticity coefficient

The specimens are heated to the austenite transformation temperature and stresses are loaded just before the austenite transformation. The temperature-strain diagrams are obtained by enlarging transformation as shown in Fig. 2-12. The austenite transformations occur at around 780℃ during heating process. Compared to the stress-free, it is seen to have differences significantly when subjected to tensile stress. As the tensile force increases, the total strain in the austenite transformation becomes smaller. In this case, because load stress is less than the yield stress point, normal plasticity strain does not occur.

As the simple phase transformation occurs, transformation plasticity behavior can be measureable. There are only transformation strain and thermal strain in the case of stress-free, while there is also transformation plasticity strain in the case of loading stress. At the same time, the elastic strain generated by the low tensile stress is extremely low, so it can be ignored. Therefore, subtracting the stress-free strain from loaded stress strain is transformation plasticity strain.

The relationship of stress and transformation plasticity strain obtained from the experimental value is shown in Fig. 2-12. As the tensile stress increases, the increase degree of transformation plastic strain decreases significantly. Transformation plasticity coefficient in the austenite transformation is not a constant value in proportion

to the stress and transformation plasticity strain.

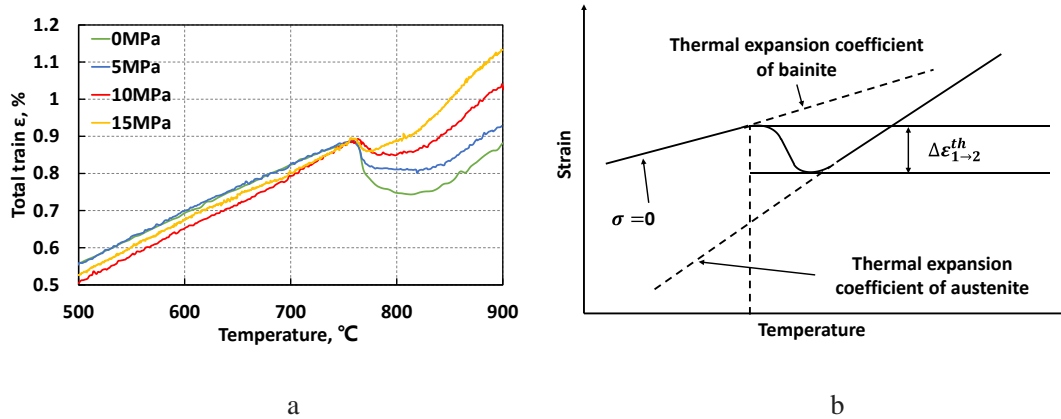a   b

Fig. 2-12 Temperature-strain diagram depending on austenite transformation

As shown in Fig. 2-3, the specimens after transformation plasticity were slowly cooled to room temperature. After each heat treatment, the specimens with different tensile stresses were ground and polished using standard techniques for metallographic examination. The nital etching solution was used for the characterization of the microstructure. The microstructure after transformation plasticity behavior with different stresses are shown in Fig. 2-12. Average grain sizes are determined by the linear intercept method. Grain size evaluated from 3 measurements is shown in Fig. 2-13. The grain size decrease with increasing tensile tress was approximated with a linear function at the level of correlation $R^2 =0.8677$. According to the calculation above, Larger stresses produce higher dislocation density, which means higher deformation energy storage and work hardening. Therefore, the nucleation of austenite obtains a greater driving force and more nucleation locations, resulting in an increasing nucleation rate. Therefore, since stress is the only variable in the experimental conditions, it proves that greater stress leads to higher dislocation density during austenite transformation.
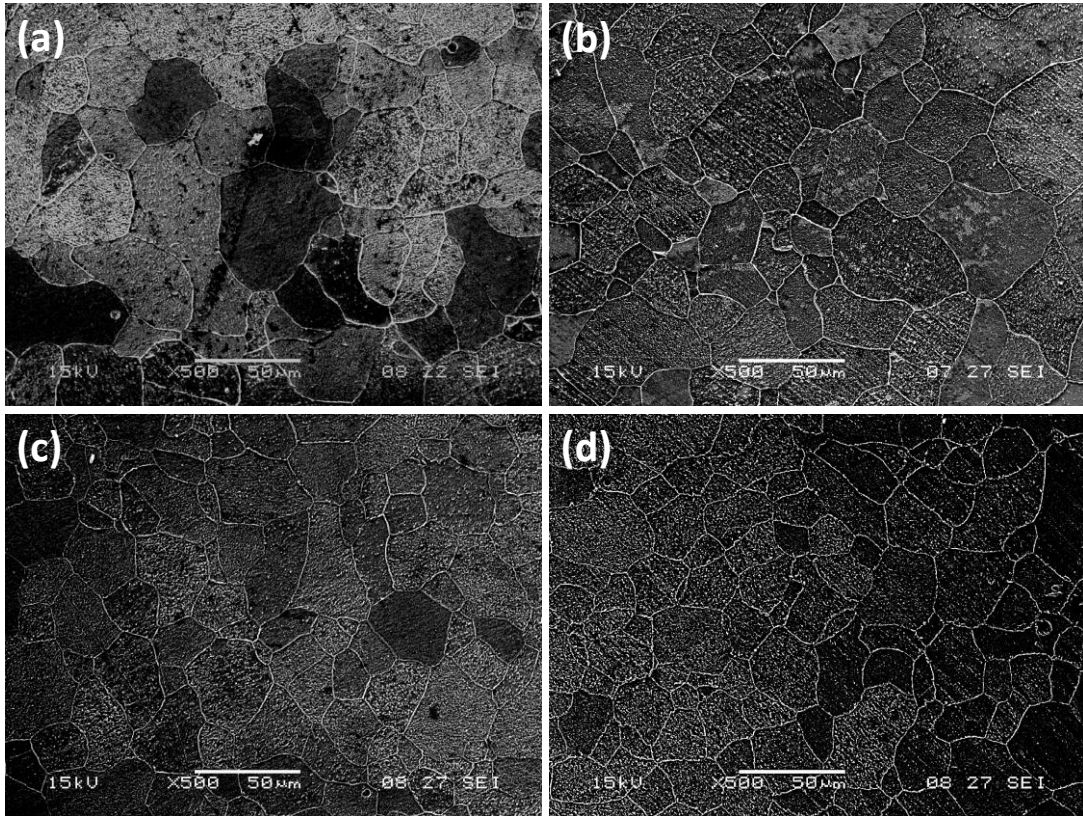
Fig. 2-13 Relation between applied stress and gain size

Considering Eq.25 and experimental data, the new mathematic model is developed to describe the transformation plasticity behavior of steels during the austenite transformation.

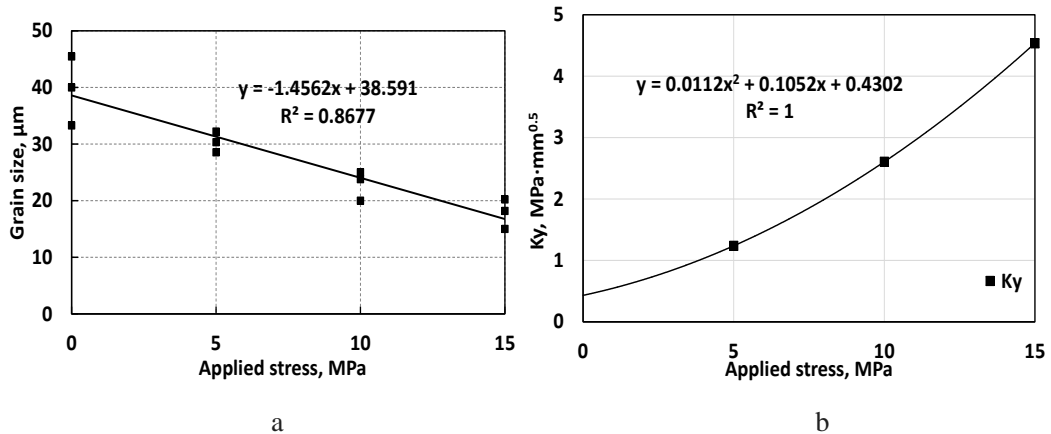The trend curve according to the new mathematic model are shown in Fig. 2-15.

a   b

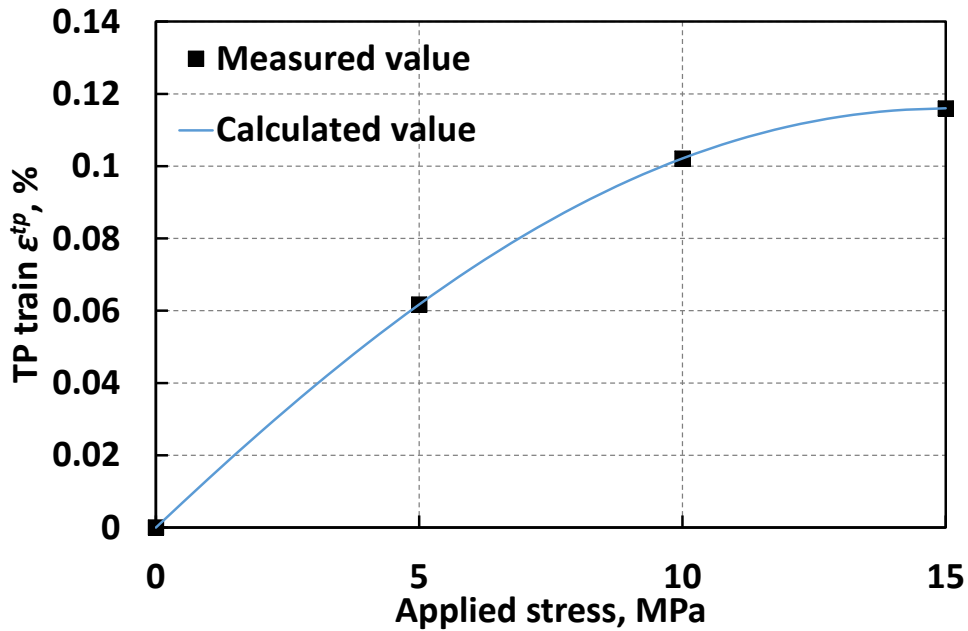Fig. 2-14 Temperature-strain diagram depending on austenite transformation

Fig. 2-15 Relation between applied stress and transformation plasticity

## 2.4.3 Mechanical properties and parameters of materials

JMatPro is a powerful material performance simulation software developed by Sente Software, UK, it can be used to calculate a variety of properties of metal materials. It is a software based on material type, the different material types have different modules. JMatPro calculates a wide range of material properties for industrial alloys such as nickel-based superalloys, steel (such as stainless steel, high-strength low-alloy steel, cast iron), aluminum alloys, magnesium alloys and titanium alloys. Each material was simulated by the software JMatPro to obtain thermal properties such as CCT curves of the material. The chemical composition of each material is shown in table 2-2.

Table 2-2 Chemical components of materials

	C	Si	Mn	Cr	Ni	Mo
20MnCrS5	0.17-0.22	≤0.4	1.10-1.50	1.00-1.30		

Fig. 2-16 shows the CCT curve of 20MnCrS5 steel. It can be seen from the figure that the austenite transformation temperature A_1 is about 728.8℃, and A_3 is about 793.8℃. The pearlite formation temperature is 581.38℃ - 709.68℃, the bainite formation temperature is 468.6℃ - 557.1℃, and the martensite formation temperature is 273.74℃ - 385.86℃. When the cooling rate is less than or equal to 0.8℃/s, the

structure of the room temperature transition product is a large amount of ferrite and pearlite. As the cooling rate increases, the content of bainite increases and the content of ferrite and pearlite decreases; when the cooling rate is more than 3℃/s, the room temperature conversion product (tissue) is a large amount of ferrite and bainite and a very small amount of pearlite. When the cooling rate is more than 30℃/s, the room temperature conversion product (tissue) is a large amount of martensite and bainite and a small amount of ferrite. This steel grade has a high martensite structure and requires a very high cooling rate. When the cooling rate reaches and exceeds 100℃/s, its room temperature structure contains about 97% martensite.
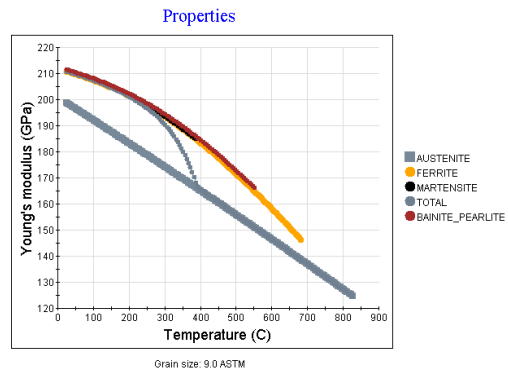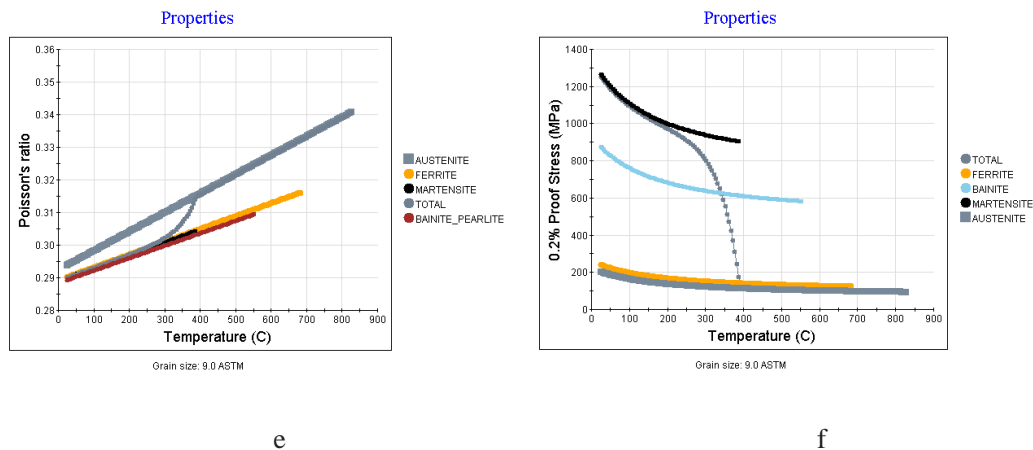

a

b

c

d

<div align="center">e   f</div>
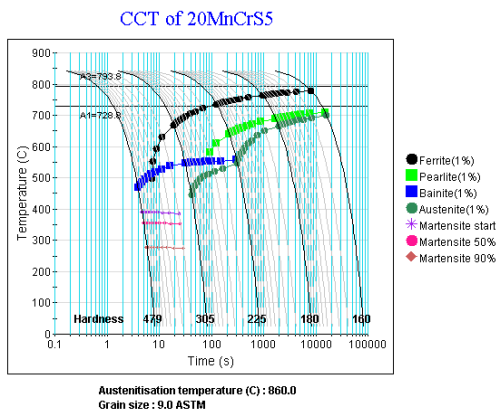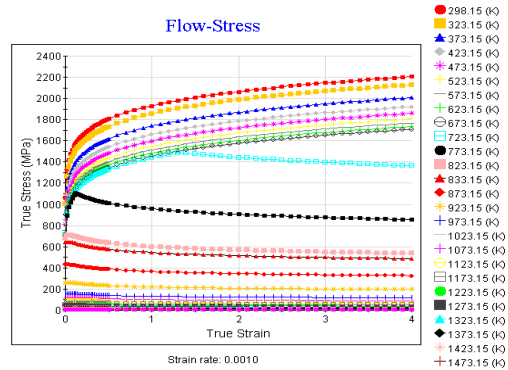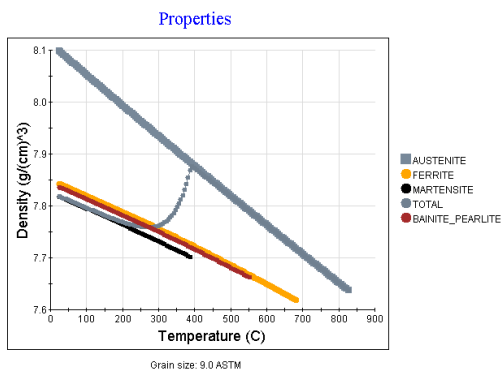
<div align="center">Fig. 2-16 CCT curve and mechanical properties of 20MnCrS5</div>

2.5 Concluding remarks

(1) It is able to measure and calculate the physical property values of material.

(2) The transformation plasticity behavior during the phase transformation can be sufficiently grasped.

(3) It is proved that the transformation plasticity coefficient in the austenitic transformation is not a constant.

(4) Transformation plastic behavior of the austenite transformation is sufficiently measurable.

(5) Transformation plasticity coefficient in the austenite transformation is not a constant value in proportion to the stress and transformation plasticity strain. As the tensile stress increases, the increase degree of transformation plastic strain decreases significantly.

(6) A new mathematic model has been developed to describe the transformation plasticity behavior of steels during the austenite transformation, which includes the influence of the gain size of the austenite.

References

[1] **Franz, C., Besserdich, G., Schulze, V., Müller, H. and Löhe, D.**, "Influence of transformation plasticity on residual stresses and distortions due to the heat treatment of steels with different carbon contents," *Journal de Physique IV (Proceedings)*, 2004, vol. 120, pp. 481-488: EDP sciences.

[2] **Mukai, R. and Ju, D.-Y.**, "Simulation of carburizing-quenching of a gear. Effect of carbon content on residual stresses and distortion," *Journal de Physique IV (Proceedings)*, 2004, vol. 120, pp. 489-497: EDP sciences.

[3] **Ju, D.-Y., Zhang, W. M., Matsumoto, Y. and Mukai, R.**, "Modeling and experimental verification of plastic behavior of the martensitic transformation plastic behavior in a carbon steel," *Solid State Phenomena*, 2006, vol. 118, pp. 369-374: Trans Tech Publ.

[4] **Mitra, A., Prasad, N. S. and Ram, G. J.,** "Estimation of residual stresses in an 800 mm thick steel submerged arc weldment," *Journal of Materials Processing Technology,* 2016, vol. 229, pp. 181-190.

[5] **Vasileiou, A. N., Smith, M. C., Balakrishnan, J., Francis, J. A. and Hamelin, C. J.,** "The impact of transformation plasticity on the Electron Beam welding of thick-section ferritic steel components," *Nuclear engineering and design,* 2017, vol. 323, pp. 309-316.

[6] **Leblond, J.-B., Devaux, J. and Devaux, J.,** "Mathematical modelling of transformation plasticity in steels I: case of ideal-plastic phases," *International journal of plasticity,* 1989, vol. 5, no. 6, pp. 551-572.

[7] **Zhu, J., Wu, H., Wang, D., Gao, Y., Wang, H., Hao, Y., Yang, R., Zhang, T.-Y., and Wang, Y.,** "Crystallographic analysis and phase field simulation of transformation plasticity in a multifunctional β-Ti alloy," *International journal of plasticity,* 2017, vol. 89, pp. 110-129.

[8] **Magee, C. L. and Paxton, H. W.**, "Transformation kinetics, microplasticity and aging of martensite in Fe-31 Ni," CARNEGIE INST OF TECH PITTSBURGH

PA1966.

[9] **Greenwood, G. W. and Johnson, R.,** "The deformation of metals under small stresses during phase transformations," *Proceedings of the Royal Society of London. Series A. Mathematical and Physical Sciences,* 1965, vol. 283, no. 1394, pp. 403-422.

[10] **Kumar, S. and Singh, R. N.,** "Crack propagation in piezoelectric materials under combined mechanical and electrical loadings," *Acta materialia,* 1996, vol. 44, no. 1, pp. 173-200.

[11] **Gwalani, B., Soni, V., Lee, M., Mantri, S., Ren, Y. and Banerjee, R.,** "Optimizing the coupled effects of Hall-Petch and precipitation strengthening in a Al0. 3CoCrFeNi high entropy alloy," *Materials & Design,* 2017, vol. 121, pp. 254-260.

[12] **Yu, H., Li, C., Xin, Y., Chapuis, A., Huang, X. and Liu, Q.,** "The mechanism for the high dependence of the Hall-Petch slope for twinning/slip on texture in Mg alloys," *Acta materialia,* 2017, vol. 128, pp. 313-326.

[13] **Cordero, Z., Knight, B. and Schuh, C.,** "Six decades of the Hall–Petch effect–a survey of grain-size strengthening studies on pure metals," *International Materials Reviews,* 2016, vol. 61, no. 8, pp. 495-512.

Chapter 3 Verification of material properties by simulation of axisymmetric model

3.1 Introduction of COSMAP

COSMAP software (Computer Simulation of Manufacturing Process) is a simulation software for heat treatment process. This simulation software is part of the research results of the international joint research project IMS-VHT developed by International IMS (Intelligent Manufacturing System) from 2003 to 2005, It is a software developed by Prof. Ju Dongying from the Saitama University of Technology and Prof. Tatsuo Inoue from Fukuyama University [1].

COSMAP is a finite element method developed based on continuum thermo-mechanical theory and metallo-thermo-mechanics. In order to understand the calculation method of COSMAP, we can refer to the finite element method and the theory of numerical analysis described in many textbooks. In addition, when using COSMAP, you need to have some basic knowledge of metal materials, material processing, metallurgy and heat treatment, thermodynamics, heat transfer and diffusion theory. As long as you have studied this knowledge in a university or a specialized school, you can use this software after a period of practice.

COSMAP can perform numerical simulations of carburizing, nitriding, quenching, and local heating and cooling processes. The COSMAP solver uses two methods, the direct method and the ICCG method. Users can choose a reasonable calculation plan according to the needs of the problem. When building models and describing calculation results, users can use the pre- and post-processing software FEMAP or GID, if the user has an inverse solution of the heat transfer coefficient and a material database, the subsystem can be constructed. As an example here, MATEQ is a material database developed by the Materials Database Research Association of the Plastics Engineering Committee of the Japan Society Materials Science. For the inverse solution of the heat transfer coefficient, users can use the interface program developed.

COSMAP trial version as a special program for heat treatment simulation demonstration, for example, quenching, carburizing, carburizing, nitriding, local heating, etc., the chemical composition concentration, temperature distribution, phase transformation and deformation-stress distribution of carbon and nitrogen can be combined and analyzed. Obviously, because of the diffusion analysis, the boundary conditions in the analysis of heat conduction and inelastic analysis depend on the change of the time, which is a function of time, and the relevant boundary conditions such as temperature and external load (for example, pressure) can be set.

3.2 Basic theory of transformation and thermodynamics

Characteristics of material can be improved by controlling the internal structure due to phase transformation, such as quenching, tempering and so on. However, such phase transformations are essentially coupled with temperature and mechanical fields. Consider the case of quenching of steels with initial structure of pearlite and ferrite. If the steel is heated up beyond A_{C1} temperature to be austenite and cooled moderately to room temperature, it will be returned back to the original pearlite and ferrite structure. On the contrary to that, when the cooling rate is high enough in the cooling process by water, oil, or polymer solution, martensite or bainite structure in addition to pearlite is induced depending on the difference in cooling rate at each location of the work.

Three kinds of field play important role: temperature field, phases of the metallic structures, and elastic - or in most cases, inelastic - stress and strain field. A variation in any of the three parameters will have an effect on the others, and the interaction is properly termed as metallo-thermo-mechanical coupling [2].

3.2.1 Mixture Rule

Materials undergoing structural change due to phase transformation is assumed to consist of a mixture of N constituents (pearlite, austenite and martensite). It is well known that changes in microstructure are really observed in microscopic level. For the analysis based on continuum mechanics level, however, any material with volume is assumed to consist of N kinds of constituents: Denoting the volume fraction of the *I-th*

constituent as ξ_I, the mechanical and physical properties χ of the material may be expressed as a linear combination of the properties χ_I of the constituents [2].

$$\chi = \sum_{I=1}^{N} \chi_I \xi_I \text{ and } \sum_{I=1}^{N} \xi_I = 1 \tag{1}$$

3.2.2 Heat Conduction Equations

For the heat transfer equation relevant to the quenching simulation, latent heat generated by phase transformation and heat generated by stress should be taken into account consideration in the normal heat conduction equation.

$$\rho c \dot{T} - \frac{\partial}{\partial \chi_i}\left(k \frac{\partial T}{\partial \chi_i}\right) - \sigma_{ij}\dot{\varepsilon}_{ij}^p + \sum \rho_I l_I \dot{\xi}_I = 0 \tag{2}$$

where, c, k and l_I denote the specific heat, the coefficient of heat conduction and the latent heat produced by the progressive I-th constituent. ρ, T and σ_{ij} are the coefficient of the density, the temperature and the stress, respectively.

The convection boundary conditions of heat transfer on the surface is assumed to be.

$$-k \frac{\partial T}{\partial \alpha_i} n_i = h_T(T - T_w) \tag{3}$$

where h_T and T_w are the heat transfer coefficient and the temperature of coolant on heat transfer boundary with unit normal n_i, respectively.

3.2.3 Diffusion equation

During carburizing and diffusion, by assuming non steady-state practical carburizing, the basic governing equation of the carbon diffusion into the iron matrix is [3].

$$\frac{\partial C}{\partial t} = \frac{\partial}{\partial \chi_i}[D \frac{\partial C}{\partial \chi_i}] \tag{4}$$

here, D is the diffusion coefficient and C is the carbon content. The derivator is time t and position χ_i direction. When the diffusion coefficient is assumed constant and independent of composition, Eq. (4) can be simplified to:

$$\frac{\partial C}{\partial t} = D \frac{\partial^2 C}{\partial \chi_i^2} \tag{5}$$

Generally, the diffusion coefficient D is determined by boundary condition being specified by reaction across the surface layer and it is expressed in:

$$D \frac{\partial C}{\partial \chi_i} n_i = h_c(C_e - C_s) \tag{6}$$

here, h_c is the coefficient of surface reaction rate, C_e is the employed carbon content of the external environment, and C_s is the carbon content in the surface. D is known to be temperature dependent according to expression.

$$D \equiv f(C_e, t) \tag{7}$$

here, C_e is the employed carbon content and t is the carburizing time.

3.2.4 Hardening rule

The yield function is determined by the plastic strain ε_{ij}^p and the scalar hardening parameter κ exhibiting the magnitude of material hardening, which depends on loading history, as well as the stress and temperature;

$$F = F(\sigma_{ij}, \varepsilon_{ij}^p, \kappa, T) \tag{8}$$

Since the scalar variables κ and T appeared in Eq. (8) play a role to isotropic expansion of yield surface, while the tensor parameter ε_{ij}^p contributes the anisotropic hardening, then it forms

$$F = F(\sigma_{ij}, \varepsilon_{ij}^p) - K(\kappa, T) \tag{9}$$

When the yield surface is assumed to expand isotropically with holding the center by this hypothesis, which gives the yield function in the form

$$F = F(\sigma_{ij}, \kappa, T) = f(\sigma_{ij}) - K(\kappa, T) \tag{10}$$

Provide that the center of the yield surface in stress space, called back stress, is denoted by α_{ij}, the mathematical description of the kinematic hardening hypothesis is now derived by substituting $\sigma_{ij} - \alpha_{ij}$ instead of σ_{ij} without κ as

$$F = F(\sigma_{ij} - \alpha_{ij}, T) = f(\sigma_{ij} - \alpha_{ij}) - K(T) \tag{11}$$

By combining the above two hypotheses of isotropic and kinematic hardening, represented by (10) and (11), respectively, we have

$$F = F(\sigma_{ij} - \alpha_{ij}, \kappa, T) = f(\sigma_{ij} - \alpha_{ij}) - K(\kappa, T) \tag{12}$$

3.2.5 Transformation plasticity

Total strain rate $\dot{\varepsilon}_{ij}$ is assumed to be divided into elastic, plastic, thermal strain rate, phase transformation and transformation plasticity such that

$$\dot{\varepsilon}_{ij} = \dot{\varepsilon}_{ij}^e + \dot{\varepsilon}_{ij}^p + \dot{\varepsilon}_{ij}^T + \dot{\varepsilon}_{ij}^{tr} + \varepsilon_{ij}^{tp} \tag{13}$$

The elastic strain is normally expressed as:

$$\varepsilon_{ij}^e = \frac{1+\nu}{E}\sigma_{ij} - \frac{\nu}{E}(\sigma_{kk})\delta_{ij} \tag{14}$$

with Young's modulus E, Poisson's ratio ν and deviator stress δ_{ij}.

The thermal strain is the function of temperature change of material $(T - T_0)$ and thermal expansion coefficient α as followed

$$\varepsilon_{ij}^T = \alpha(T - T_0)\delta_{ij} \tag{15}$$

where α is expressed as the function of carbon content and volume fraction of the structure.

The plastic strain rate is reduced to the form by employing temperature dependent materials parameters

$$\dot{\varepsilon}_{ij}^p = \lambda\frac{\partial F}{\partial \sigma_{ij}} \tag{16}$$

$$\lambda = \hat{G}\left\{\frac{\partial F}{\partial \sigma_{kl}}\sigma_{kl} + \frac{\partial F}{\partial T}\dot{T} + \sum_{I=1}^{N}\frac{\partial F}{\partial \xi_I}\dot{\xi}_I + \frac{\partial F}{\partial C}\dot{C}\right\} \tag{17}$$

$$\frac{1}{\hat{G}} = -\left\{\frac{\partial F}{\partial \varepsilon_{mn}^P} + \frac{\partial F}{\partial k}\sigma_{mn}\right\}\frac{\partial F}{\partial \sigma_{mn}} \tag{18}$$

with a temperature dependent yield function

$$F = F(T, C, \sigma_{ij}, \varepsilon^P, \xi_I, \kappa) \tag{19}$$

where T is the temperature, C is the carbon content, σ_{ij} is the flow stress, ε^P is the plastic strain, ξ_I is the individual phase, κ is the hardening parameter.

Strain rates due to structural dilatation depending on the I-th constituent is

$$\dot{\varepsilon}_{ij}^{tr} = \sum_{I=1}^{N}\beta_I\dot{\xi}_I\delta_{ij}, \tag{20}$$

here, β_I is the coefficient of the phase transformation in fractional length change due to phase change instantaneously [4, 5].

Transformation plasticity depending on the I-th constituent is

$$\dot{\varepsilon}_{ij}^{tp} = 3K(1 - \xi)\dot{\xi}\delta_{ij} \qquad (21)$$

where K_I is the coefficient of transformation plasticity for martensitic, bainitic and Pearlite transformation which stand for the dilatation due to structural for the I-th constituent. δ_{ij} is the deviator stress [4].

3.2.6 Rate form of stress-strain relation

The total strain rate is divided into the elastic strain rate and the plastic strain rate within the framework of the infinitesimal theory; that is

$$\dot{\varepsilon}_{ij} = \dot{\varepsilon}_{ij}^{e} + \dot{\varepsilon}_{ij}^{p} \qquad (22)$$

The elastic part of the total strain rate is given by Hooke's law,

$$\dot{\varepsilon}_{ij} = \frac{1}{2G}\left(\dot{\sigma}_{ij} - \frac{\nu}{1+\nu}\delta_{ij}\dot{\sigma}_{kk}\right) + \delta_{ij}\alpha\dot{T} \qquad (23)$$

Where G, ν and α stand for shear modulus, Poisson's ratio, and linear expansion coefficient, respectively. We obtain the expression for the total strain rate,

$$\dot{\varepsilon}_{ij} = \frac{1}{2G}\left(\dot{\sigma}_{ij} - \frac{\nu}{1+\nu}\delta_{ij}\dot{\sigma}_{kk}\right) + \delta_{ij}\alpha\dot{T} + \hat{G}(\frac{\partial F}{\partial \sigma_{kl}}\dot{\sigma}_{kl} + \frac{\partial F}{\partial T}\dot{T})\frac{\partial F}{\partial \sigma_{ij}} \qquad (24)$$

Inverting the equation for the stress rate $\dot{\sigma}_{ij}$ under the assumption of constant volumetric plastic strain yields

$$\dot{\sigma}_{ij} = 2G\left(\delta_{ik}\delta_{jl} + \frac{\nu}{1-2\nu}\delta_{ij}\delta_{kl} - \frac{1}{S_0}\frac{\partial F}{\partial \sigma_{ij}}\frac{\partial F}{\partial \sigma_{kl}}\right)\left(\dot{\varepsilon}_{kl} - \delta_{kl}\alpha\dot{T}\right) - \frac{1}{S_0}\frac{\partial F}{\partial \sigma_{ij}}\frac{\partial F}{\partial T}\dot{T} \qquad (25)$$

Where

$$S_0 = \frac{1}{2G\hat{G}} + \frac{\partial F}{\partial \sigma_{mn}}\frac{\partial F}{\partial \sigma_{mn}} \qquad (26)$$

For further application of the constitutive equation in the finite element method, to be treated in Section5, it is useful to present the relation in the matrix form [ ],

$$\{\dot{\sigma}\} = [D^{ep}](\{\dot{\varepsilon}\} - \{\alpha\}\dot{T}) - \frac{1}{S_0}\left\{\frac{\partial F}{\partial \sigma}\right\}\frac{\partial F}{\partial T}\dot{T} \qquad (27)$$

where the components in matrices of stress and strain in engineering notation, and coefficient of linear expansion are, respectively,

$$\{\sigma\}^T = \{\sigma_x \sigma_y \sigma_z \tau_{xy} \tau_{yz} \tau_{xz}\},$$

$$\{\varepsilon\}^T = \{\varepsilon_x \varepsilon_y \varepsilon_z \gamma_{xy} \gamma_{yz} \gamma_{xz}\},$$

$$\{\alpha\}^T = \{\alpha \ \alpha \ \alpha \ 0 \ 0 \ 0\}. \tag{28}$$

Here, the matrix $[D^{ep}]$ is given as [   ]

$$[D^{ep}] = [D^e] - [D^p] \tag{29}$$

With

$$[D^e] = 2G \begin{bmatrix} \frac{1-\nu}{1-2\nu} & & & & & sym. \\ \frac{\nu}{1-2\nu} & \frac{1-\nu}{1-2\nu} & & & & \\ \frac{\nu}{1-2\nu} & \frac{1-\nu}{1-2\nu} & \frac{1-\nu}{1-2\nu} & & & \\ 0 & 0 & 0 & \frac{1}{2} & & \\ 0 & 0 & 0 & 0 & \frac{1}{2} & \\ 0 & 0 & 0 & 0 & 0 & \frac{1}{2} \end{bmatrix} \tag{30}$$

And

$$[D^p] = \frac{2G}{S_0} \begin{bmatrix} \left(\frac{\partial F}{\partial \sigma_x}\right)^2 & & & & & sym. \\ \frac{\partial F}{\partial \sigma_x}\frac{\partial F}{\partial \sigma_y} & \left(\frac{\partial F}{\partial \sigma_y}\right)^2 & & & & \\ \frac{\partial F}{\partial \sigma_x}\frac{\partial F}{\partial \sigma_z} & \frac{\partial F}{\partial \sigma_y}\frac{\partial F}{\partial \sigma_z} & \left(\frac{\partial F}{\partial \sigma_z}\right)^2 & & & \\ \frac{1}{2}\frac{\partial F}{\partial \sigma_x}\frac{\partial F}{\partial \tau_{xy}} & \frac{1}{2}\frac{\partial F}{\partial \sigma_y}\frac{\partial F}{\partial \tau_{xy}} & \frac{1}{2}\frac{\partial F}{\partial \sigma_z}\frac{\partial F}{\partial \tau_{xy}} & \frac{1}{4}\left(\frac{\partial F}{\partial \tau_{xy}}\right)^2 & & \\ \frac{1}{2}\frac{\partial F}{\partial \sigma_x}\frac{\partial F}{\partial \tau_{yz}} & \frac{1}{2}\frac{\partial F}{\partial \sigma_y}\frac{\partial F}{\partial \tau_{yz}} & \frac{1}{2}\frac{\partial F}{\partial \sigma_z}\frac{\partial F}{\partial \tau_{yz}} & \frac{1}{4}\frac{\partial F}{\partial \sigma_{xy}}\frac{\partial F}{\partial \tau_{yz}} & \frac{1}{4}\left(\frac{\partial F}{\partial \tau_{yz}}\right)^2 & \\ \frac{1}{2}\frac{\partial F}{\partial \sigma_x}\frac{\partial F}{\partial \tau_{zx}} & \frac{1}{2}\frac{\partial F}{\partial \sigma_y}\frac{\partial F}{\partial \tau_{zx}} & \frac{1}{2}\frac{\partial F}{\partial \sigma_z}\frac{\partial F}{\partial \tau_{zx}} & \frac{1}{4}\frac{\partial F}{\partial \sigma_{xy}}\frac{\partial F}{\partial \tau_{zx}} & \frac{1}{4}\frac{\partial F}{\partial \sigma_{yz}}\frac{\partial F}{\partial \tau_{zx}} & \frac{1}{4}\left(\frac{\partial F}{\partial \tau_{zx}}\right)^2 \end{bmatrix} \tag{31}$$

As an example of the yield functions, let us consider the Von Mises condition with isotropic hardening, i.e.

$$F = \frac{1}{2}s_{ij}s_{ij} - \frac{1}{3}\bar{\sigma}(\bar{\varepsilon}^p)^2 \tag{32}$$

Here, temperature dependence on flow stress $\bar{\sigma}$ is ignored for simplicity. Bearing in mind that $\frac{\partial F}{\partial \sigma_{ij}} = s_{ij}$, the hardening function is easily expressed as

$$\frac{1}{\bar{G}} = -\left(\frac{2}{3}s_{mn}s_{mn}\right)^{\frac{1}{2}}\left(-\frac{2}{3}\bar{\sigma}\frac{\partial \bar{\sigma}}{\partial \bar{\varepsilon}^p}\right) = \frac{4}{3}\frac{\bar{\sigma}^2\bar{\sigma}}{\bar{\varepsilon}^p} \tag{33}$$

Leads to the so-called Prandtl-Reuss flow rule:

$$\dot{\varepsilon}_{ij}^p = \frac{3}{2}\frac{\bar{\dot{\varepsilon}}^p}{\bar{\sigma}}s_{ij} \tag{34}$$

The hardening coefficient H' is defined as the tangent modulus of the (equivalent) stress-(equivalent) plastic strain diagram, it becomes

$$\dot{\varepsilon}_{ij}^p = \frac{3}{2}\frac{\bar{\sigma}}{\sigma H'}s_{ij} \tag{35}$$

The matrix $[D^{ep}]$ is simplified in this case to the form

$$[D^p] = \frac{2G}{S_0}\begin{bmatrix} S_x^2 & & & & & sym. \\ S_xS_y & S_y^2 \\ S_xS_z & S_yS_z & S_z^2 \\ S_x\tau_{xy} & S_y\tau_{xy} & S_z\tau_{xy} & \tau_{xy}^2 \\ S_x\tau_{yz} & S_y\tau_{yz} & S_z\tau_{yz} & \tau_{xy}\tau_{yz} & \tau_{yz}^2 \\ S_x\tau_{zx} & S_y\tau_{zx} & S_z\tau_{zx} & \tau_{xy}\tau_{zx} & \tau_{yz}\tau_{zx} & \tau_{zx}^2 \end{bmatrix} \tag{36}$$

With

$$S_0 = \frac{2}{3}\bar{\sigma}\left(1 + \frac{1}{3G}\frac{\bar{\sigma}}{\bar{\varepsilon}^p}\right) = \frac{2}{3}\bar{\sigma}\left(1 + \frac{H'}{3G}\right) \tag{37}$$

Since the Von Mises yield function with kinematic hardening with yield stress $\overline{\sigma_0}$ takes the form

$$F = \frac{1}{2}(s_{ij} - \beta_{ij})(s_{ij} - \beta_{ij}) - \frac{1}{3}\bar{\sigma}^2, \quad \beta_{ij} = x_{ij} - \frac{1}{3}\delta_{ij}\alpha \tag{38}$$

For further application to two-dimensional problems, the matrix $[D^{ep}]$ is now reduced to [ ]

$$[D^{ep}] = [D^e] - [D^p] \tag{39}$$

with elastic stress-strain matrix

$$[D^e] = \begin{cases} 2G\begin{bmatrix} \frac{1}{1-v} & & sym. \\ \frac{1}{1-v} & \frac{1}{1-v} \\ 0 & 0 & \frac{1}{2} \end{bmatrix} & \text{for plane stress} \\[3em] 2G\begin{bmatrix} \frac{1-v}{1-2v} & & sym. \\ \frac{1-v}{1-2v} & \frac{1-v}{1-2v} \\ 0 & 0 & \frac{1}{2} \end{bmatrix} & \text{for plane strain} \end{cases} \tag{40}$$

The form of matrix $[D^p]$ is now generally presented as

$$[D^p] = \frac{2G}{S_0}\begin{bmatrix} S_1^2 & & sym. \\ S_1S_2 & S_2^2 \\ S_1S_3 & S_2S_3 & S_1^2 \end{bmatrix} \tag{41}$$

3.2.7 Austenite transformation plasticity

According to the previous article, it is known that the transformation plasticity strain is shown as followed

$$\dot{\varepsilon}_{ij}^{tp} = \sum_{l=1}^{N} 3K(1-\xi)\dot{\xi}S_{ij} \tag{42}$$

The transformation plasticity stress in the case of uniaxial strain is shown as followed

$$K = \overline{\varepsilon^{tp}}\big/\bar{\sigma} \tag{43}$$

Where $\overline{\varepsilon^{tp}}$ is the equivalent stress, the transformation plasticity coefficient K can be determined by a tensile test when phase transformation occurs.

However, at the heating stage, it is predicted that transformation plasticity depends on the grain system when austenite transformation occurs, transformation plasticity strain is expressed by the following equation.

$$\dot{\varepsilon}_{ij}^{tp} = 3\frac{-\Delta\varepsilon_{1\to2}^{th}}{(\sigma_0 + k_y \cdot d^{-0.5})}\ln(\zeta)\dot{\zeta}s_{ij} \tag{44}$$

The transformation plasticity stress in the case of uniaxial strain is shown as

$$\overline{\varepsilon^{tp}} = \frac{2\Delta\varepsilon_{1\to2}^{th}}{(\sigma_0 + k_y \cdot d^{-0.5})}\bar{\sigma} \tag{45}$$

Where σ_0 is the friction resistance for dislocation movement within the polycrystalline grains. k_y is a measure of the local stress needed at a grain boundary for the transmission of plastic flow. d is the average grain size. σ_0 is proved to be constant. k_y is difficult to identify experimentally.

When austenite transformation occurs, the linearity parameters between transformation plasticity strain and stress is summarized as follows.

$$K(\bar{\sigma}) = \overline{\varepsilon^{tp}}\big/\bar{\sigma} \tag{46}$$

$$K = a_1 + a_2\bar{\sigma} + a_3\bar{\sigma}^2 \tag{47}$$

Specifically, from the experimental results shown in the following figures, the stress-dependent is fitted by the least squares method, The result is shown as followed

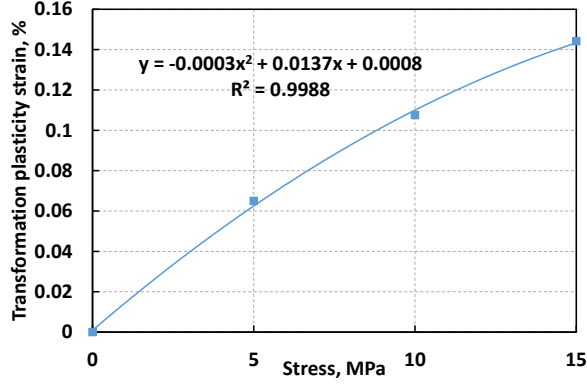$$K = 0.008 + 0.0137\bar{\sigma} - 0.0003\bar{\sigma}^2 \tag{48}$$

Fig. 3-1 Relation between applied stress and transformation plastic strain

According to the above proposal, the stress / strain formulation of the finite element method considering the transformation plastic strain of the austenite transformation can be expressed as follows.

$$\{d\varepsilon\} = [D^e]^{-1}\{d\sigma\} + \frac{\partial [D^e]^{-1}}{\partial T}\frac{\partial T}{\partial t}\{\sigma\} + \sum_{I=1}^{N}\alpha_I(T-T_0)\,d\xi_I\{1\} + \sum_{I=1}^{N}\alpha dT\{1\} +$$

$$\sum_{I=1}^{N}\beta_I\,d\xi_I\{1\} + 3K(\bar\sigma)\ln(\xi_I)\,d\xi_I\{s\} + \hat{G}\left\{(\frac{\partial F}{\partial\{\sigma\}}\{d\sigma\} + \frac{\partial F}{\partial T}dT) + \sum_{I=1}^{N}\frac{\partial F}{\partial\xi_I}d\xi_I\right\}\left\{\frac{\partial F}{\partial\sigma}\right\}$$

(49)

$$\{d\sigma\} = [D^e]\left(\{d\varepsilon\} - \frac{\partial [D^e]^{-1}}{\partial T}\frac{\partial T}{\partial t}\{\sigma\} - \sum_{I=1}^{N}\alpha_I(T-T_0)\,d\xi_I\{1\} - \sum_{I=1}^{N}\alpha dT\{1\} -\right.$$

$$\left.\sum_{I=1}^{N}\beta_I\,d\xi_I\{1\} - 3K(\bar\sigma)\ln(\xi_I)\,d\xi_I\{s\} - \hat{G}\left\{(\frac{\partial F}{\partial\{\sigma\}}\{d\sigma\} + \frac{\partial F}{\partial T}dT) + \sum_{I=1}^{N}\frac{\partial F}{\partial\xi_I}d\xi_I\right\}\left\{\frac{\partial F}{\partial\sigma}\right\}\right)$$

(50)

3.3 Effect of transformation plasticity on simulation of quenching

In order to verify the effect of transformation plasticity on simulation of quenching, simulation is performed using a coupled analysis code COSMAP (Computer Simulation system for Material Processing) based on the metallo-thermo-mechanics theory. The analysis model which is used in the simulation is shown in Fig. 3-2. Analysis model of the simulation, which is the axially symmetric model (1/4 model) of the round bar tensile specimens with the same dimensions of Fig. 3-2 by the 3DCAD software GiD, is created. The total number of nodes points of the analysis model is 909 and the total number of elements is 800. Constraint conditions constrain all the Y-axis

nodes in the X direction of the cylinder, and restrain all the X-axis nodes in the Y direction, then load the tensile load. Heat transfer boundary conditions are set in the cylindrical side and top. The measurement point of each data is shown in Fig. 3-3. Measurement point is measured by one point between the equivalent surface gauges of 3mm from the X-axis. Heat treatment process of the simulation is in the same condition as shown in Fig. 3-4.
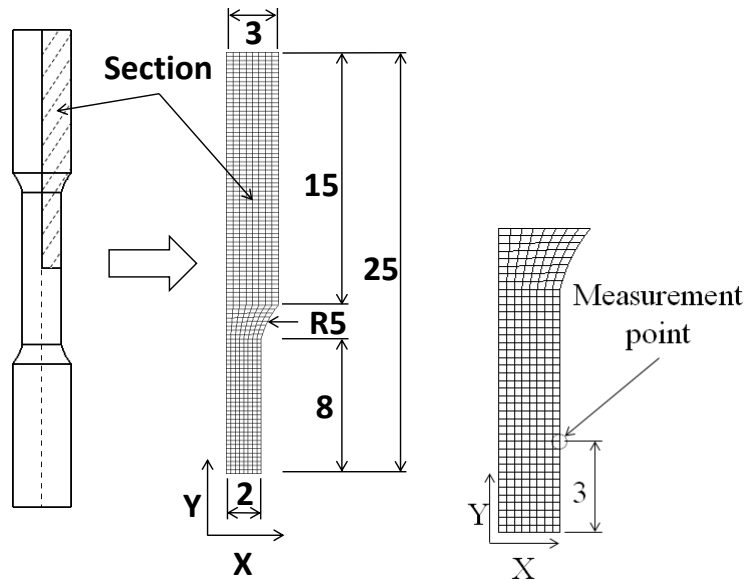

Fig. 3-2 Analysis model of cylinder and measurement point
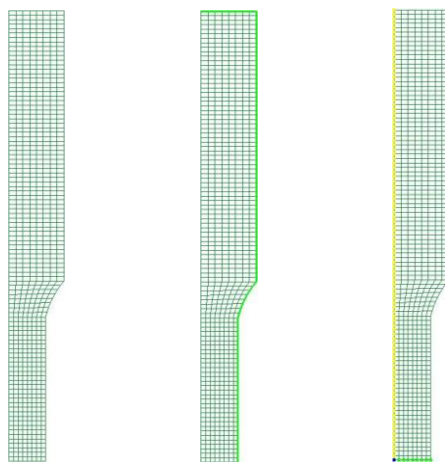
Fig. 3-3 Heat transfer boundary condition and restraint condition
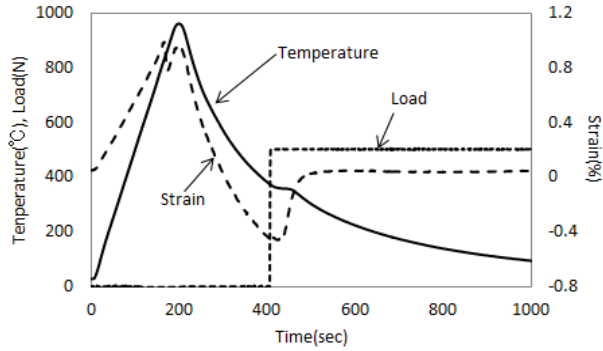
Fig. 3-4 Example of a heat treatment process

    20MnCrS5 is loaded around the following tensile load yield stress point from the vicinity of 350°C immediately before the martensitic transformation. The temperature-strain diagrams are obtained by enlarging martensitic transformation as shown in Fig. 3-6. Martensitic transformation from austenite occurs at around 350°C during cooling. As phase transformation except martensitic transformation does not occur, transformation plasticity behavior of the martensitic transformation can be measureable. Compared to the stress-free, it is seen to have different significantly as the load stress increases. There are only transformation strain and thermal strain in the case of stress-free, while there is also transformation plasticity strain in the case of loading stress. Therefore, subtracting the stress-free strain from loaded stress strain is transformation plasticity strain. It is divided by the stress loaded with transformation plasticity strain is transformation plasticity coefficient. In this case, because load stress is under the yield stress point, normal plasticity strain does not occur.
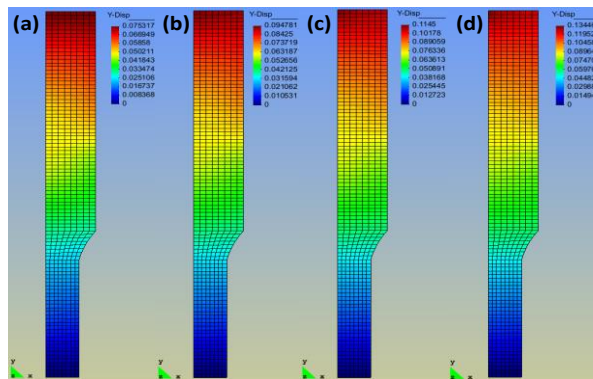
Fig. 3-5 Deformation of specimen under different stresses: (a) 0Mpa; (b) 10Mpa; (c) 20Mpa; (d) 30MPa
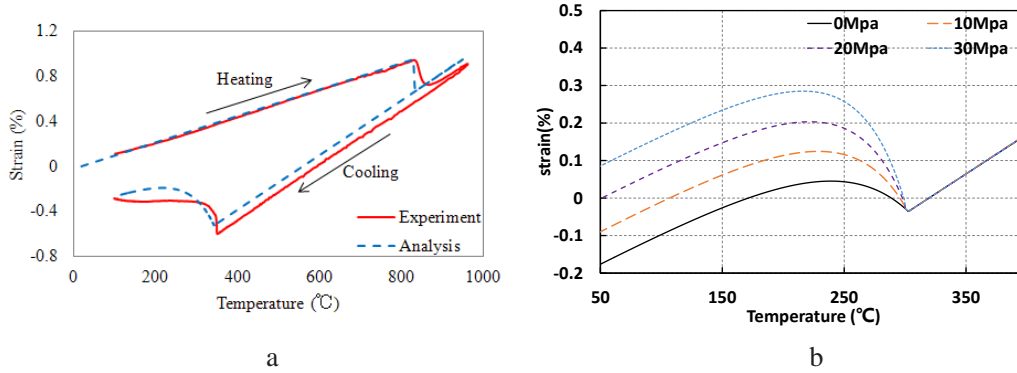
Fig. 3-6 Temperature-strain diagram of analysis

It can be proved that transformation plastic behavior of the martensitic transformation is sufficiently measurable. The transformation plasticity coefficient in the martensitic transformation revealed that it takes a constant value which is independent of the applied stress. With the reduction of carbon equivalent, the transformation plasticity coefficient becomes bigger gradually.

3.4 Effect of transformation plasticity on simulation

Based on the series of governing equations above, the simulation is used to predict the temperature field, carbon diffusion, phase transformation and distortion during carburizing-quenching process. The simulation case in carburizing-quenching process is a cylinder made of 20MnCrS5 steel which the carbon content 0.2% and about Chromium 1%. The total nodes and elements are 5935 and 3455, respectively. The restrictive conditions and the boundary conditions are set as shown in Fig. 3-7. Fig. 3-8 shows the heat treatment process.
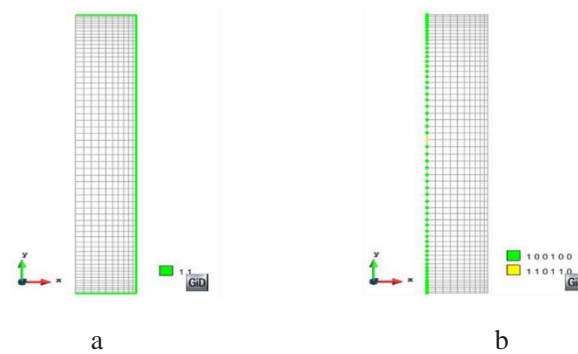

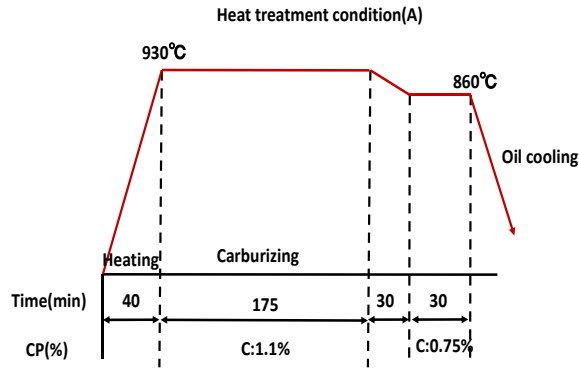Fig. 3-7 Restrictive conditions and boundary conditions

Fig. 3-8 Carburizing-quenching condition

3.4.1 Carbon Diffusion and Distribution

Fig. 3-9 shows the carbon content at the surface of the cylinder after carburizing-quenching. The distribution gradient of the carbon content from surface to the inside due to the carbon diffusion can be observed. At the surface, the carbon content reaches 0.75%. Inside the cylinder, the carbon content still keeps low. In addition, the carburizing depth into the surface is about 500μm.

The difference of the carbon content at the surface and inside of the cylinder after carburizing process has a great effect on the phase transformations and will result in martensite layer with a high hardness in the following quenching process. Fig. 3-9 shows the calculated bainite and martensite fraction of the cylinder after carburizing-quenching process. It shows that martensite forms near the surface, which corresponds with results shown in Fig. 3-10.

Fig. 3-10(a) shows the microstructure at the near surface and Fig. 3-10(b) shows the microstructure at the core of the cylinder. High fraction acicular martensite and partial residual austenite can be observed near the surface which confirm the carbon content becomes high. The mixed microstructure of lath martensite and bainite can be seen at the core of the cylinder.

The comparison of the carbon content and the microstructure shows that the simulation is in good accordance with experimental results, which satisfied the engineering requirements.
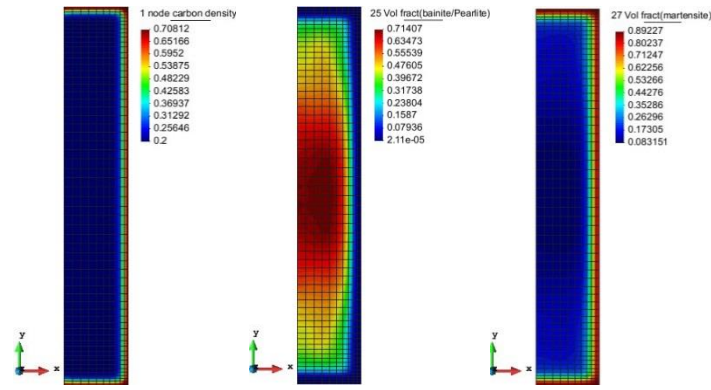
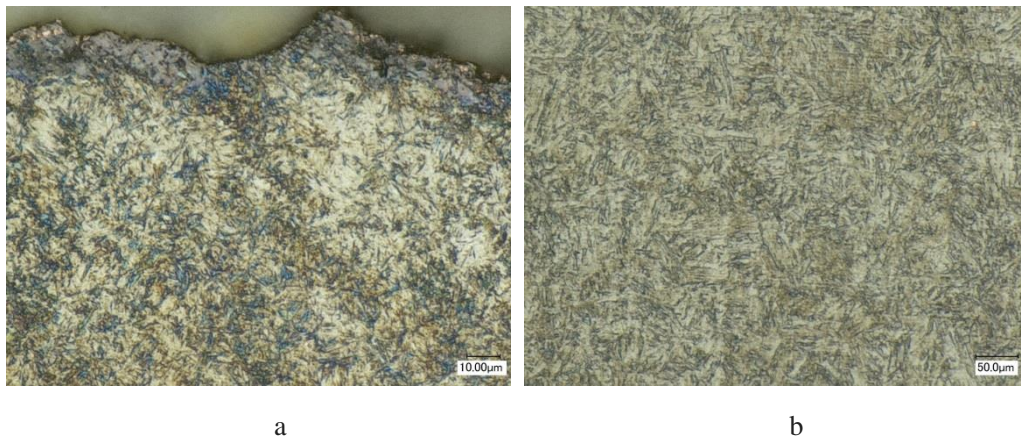Fig. 3-9 Distribution of carbon content, bainite and martensite

a	b

Fig. 3-10 Microstructural of cylinder

3.4.2 Hardness Distribution

In order to verify the accuracy of simulation, the carburizing-quenching process is simulated and tested using the process shown in Fig. 3-8.

Fig. 3-11 shows the measured and calculated Vickers hardness after carburizing-quenching treatment from the surface. From the results, we can know that after carburizing-quenching the surface hardness is about 700 kgf/mm^2 and the hardness distribution is uniform. Both simulation and experiment show that the hardness at the surface of the cylinder after heat treatment A is higher. It proves that condition A can achieve a higher surface hardness comparing with condition B. The simulation results verify the trend of the experimental results well and they are very close to the experimental results. The good agreement indicates that the simulation can be used in the following process optimization.
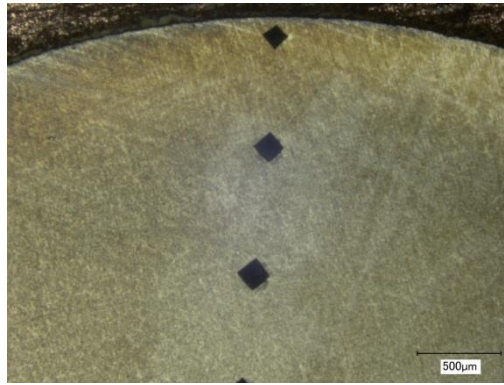
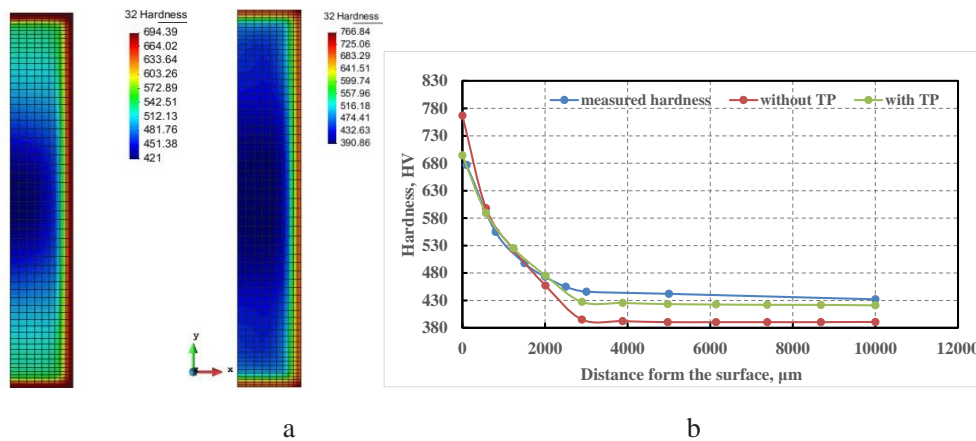Fig. 3-11 Hardness distribution of cylinder

a   b

Fig. 3-12 Distributions of Hardness

3.4.3 Results of Residual Stresses

Fig. 3-13 shows the calculated residual stress of the cylinders after carburizing-quenching process. Fig. 3-14 shows the calculated residual stress considering the transformation plasticity and the measured residual stress along the line AB after carburizing-quenching process. From the results, compressive stress at the pitch circle of the cylinder is formed. In order to verify the simulated residual stresses, the residual stresses on the surface of the cylinder were measured by X-ray diffraction. A diffractometer (Rigaku PSPC/MICRO stress analyzer) is used to produce Cr-Kα X-ray radiation at a voltage of 30 kV and an electricity of 30mA. The instrument uses a collimator with a diameter of 1mm. The measured stress agreed well with the calculated results, which verified the validity of this simulation.
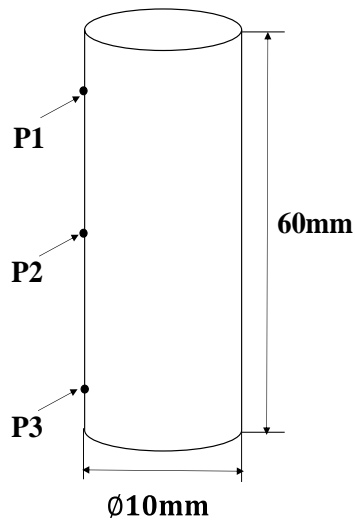
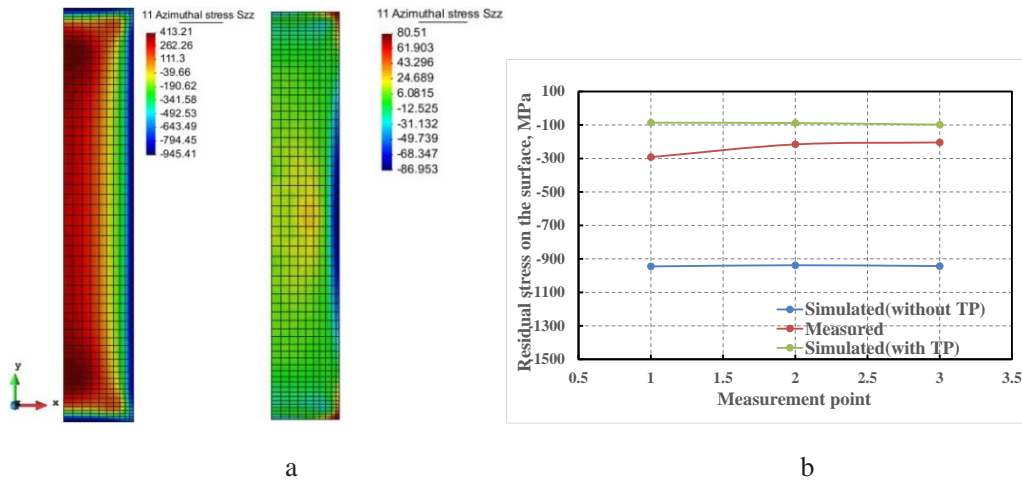Fig. 3-13 Residual stress on the surface of the cylinders

a   b

Fig. 3-14 Residual stresses on the surface of the cylinders

3.4.4 Distortion of the Cylinder after Quenching

The distortion of the cylinder after heat treatment is shown in Fig. 3-15. The distortion of the cylinder can be also calculated after carburizing-quenching. It shows the simulated and measured distortion values after carburizing-quenching. The simulation results verify the trend of the experimental results well and they are very close to the experimental results. It is proved that considering transformation plasticity will increase the accuracy of the deformation in the simulation.
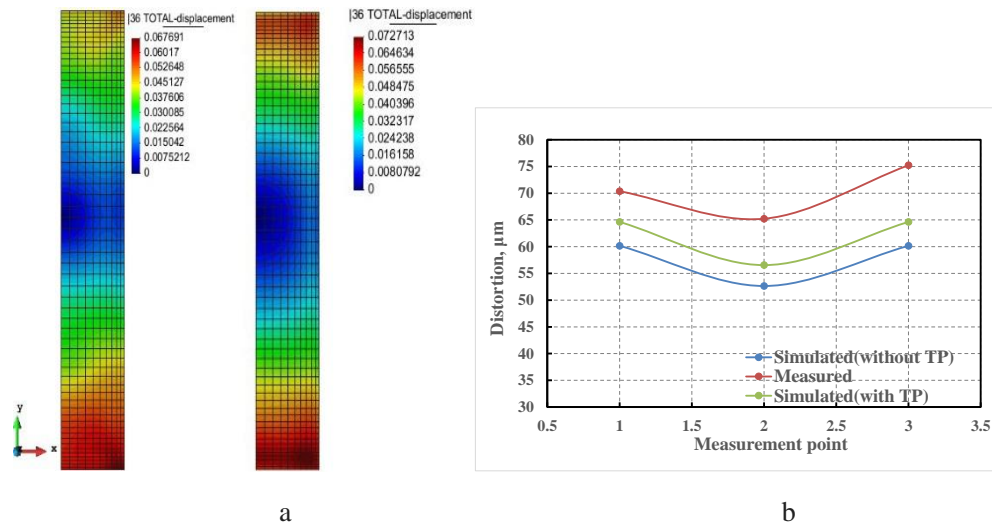
Fig. 3-15 Distortion distribution of cylinder

3.5 Effect of quenching oil on heat treatment results

In the quenching treatment, the boiling coolant, like water or water-soluble polymer aqueous solution is usually used [6] [7]. Especially oils with little defects are widely used in steel heat treatment. Although it is possible to increase the strength by performing heat treatment using these coolants, residual stress is generated, which may cause defects such as strain and crack [8]. Furthermore, non-uniformity of cooling caused by heat convection during cooling, boiling of the coolant, and adhesion of bubbles may cause problems such as variations in deformation and insufficient hardness. Therefore, quenching phenomenon is a complex system. In order to guarantee the quality of the quenched material, it is important to predict the heat-dynamic behavior such as heat convection including quenching process, heat transfer phenomenon including boiling, heat conduction, transformation and inelastic deformation generated in the quenched material is there [9, 10].

Along with recent advances in numerical analysis technology and computers, general-purpose cords using transformation, heat and dynamics theory have been developed to elucidate the phase transformation and thermal-mechanical behavior in the quenching process, and simulation of various quenching processes is often done.

However, most of them focused on the phase transformation, residual stress and

deformation that occurred inside the material, the study considering the effect of the heat transfer behavior of the coolant used for quenching on the material. It has not been done enough yet.

Usually, a boiling coolant is used for hardening treatment, water or a water-soluble polymer aqueous solution are also used [11]. Especially oils with less heat treatment defects are widely used in steel heat treatment. Although it is possible to increase the strength by heat treatment using these coolants. Therefore, residual stress is generated, which may cause defects such as strain and crack. Furthermore, non-uniformity of cooling caused by heat convection during cooling, boiling of the coolant, and adhesion of bubbles may cause problems such as variations in deformation and insufficient hardness. Therefore, the quenching phenomenon is a complex system, in order to guarantee the quality of the quenched material, it is important to predict thermal and dynamic behavior such as heat transfer phenomena including heat convection and boiling in the quenching process, heat conduction, transformation and inelastic deformation generated in the quenched material.

Along with recent advances in numerical analysis technology and computers, in order to elucidate the phase transformation and the thermodynamic behavior in the quenching process, a general purpose code using transformation, heat and dynamics theory was developed. However, most of them focused on phase transformation, residual stress and deformation occurred inside of the material, the research that takes into consideration the effect of the heat transfer behavior of the coolant used for quenching on the material has not yet been carried out sufficiently.

The most important factor in the coolant used for quenching is cooling capacity [12, 13]. In general, the cooling capacity can be obtained by measuring the temperature change using a silver specimen prescribed in the cooling performance test method. However, this method can not be used for simulation analysis unlike the actual cooling curve in quenching. Also, it is impossible to measure the surface of the material to be baked, it can be obtained by inserting a thermocouple inside the material surface and

measuring the temperature. Therefore, it can not be applied to the heat transfer boundary condition set on the material surface. Therefore, in the heat treatment simulation, it is possible to evaluate the cooling capacity of the coolant, and at the same time, the heat transfer coefficient that can be used as the heat transfer boundary condition in the simulation is used [11, 14, 15]. Furthermore, the temperature change in the actual quenching process of steel also depends on the shape and physical properties of the specimen. In addition, due to non-uniformity of cooling due to phenomena such as thermal convection and vapor film, the temperature change of the specimen surface varies from place to place. Even in quenching simulation, it is necessary to consider the influence of these phenomena.

In other words, rather than inputting the same heat transfer coefficient value to all of the thermal boundary conditions of the analytical model, it is necessary to input the value of the detailed heat transfer coefficient locally, and in the simulation the shape of the specimen and the surface Identifying heat transfer coefficients and heat transfer boundary conditions that are dependent on temperature change is an important factor.

In this laboratory, a disc-shaped sample was used to evaluate the cooling ability of the coolant used in the heat treatment. The nucleate boiling and vapor film associated with the coolant during heat treatment have a large effect on the surface cooling rate of the disk-shaped sample used. Use the right size to avoid the effects of other phenomena on the experiment. In the experiment, the disc-shaped sample was placed at an angle to the coolant to measure the temperature change of the upper and lower surfaces.

During the experiment, the disc-shaped sample was heated to a temperature above the austenite transformation. The material of the test piece was austenitic stainless steel SUS303. Because SUS303 does not undergo phase transformation during cooling, it will not be due to the phase change generates latent heat and the cooling capacity of the coolant can be measured separately. The disc-shaped test piece used in the experiment is shown in Fig. 3-16. To measure the upper and lower temperatures of the disk probe that are primarily susceptible to nuclear boiling and vapor film, two K-type

thermoelectric pairs are inserted into the center of the disk. In order to fix the disc probe, the M5 type screw was fixed on the side of the jig before the three were fixed, and a screw track of 1 mm was machined on the probe side. Considering the gap between the clamp and the probe and the thermal insulation of the side, a distance of 0.01 mm is retained to hold the probe and clamp.

In this experiment, in order to reduce the influence of convection, we prepared a jig in which two parallel angles of $\theta = 0°$ and $\theta = 60°$ were placed.

The heat treatment process of this study is shown in Fig. 3-17. The test piece was first heated for 30 minutes so that the center temperature of the test piece reached 850 °C, followed by heat retention for 30 minutes, and then quenching was carried out by adding a coolant. Note: Regarding the quenching conditions, the oil temperature used was 60°C each, and there was no stirring.
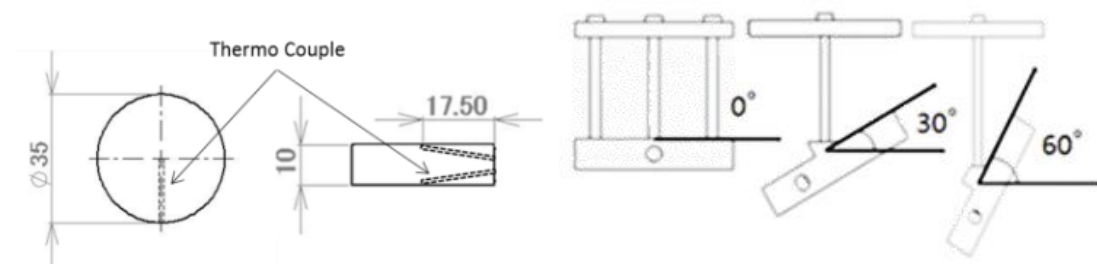

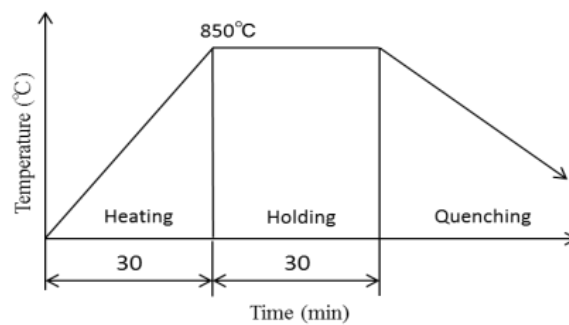Fig. 3-16 Model and fixture of the disc sample

Fig. 3-17 Heat treatment process with the same heat transfer coefficient

Using the above experimental methods, the heat transfer coefficients of various oils are measured as shown in Fig. 3-18. It can be obtained from the results that the oil H has the smallest heat transfer coefficient.
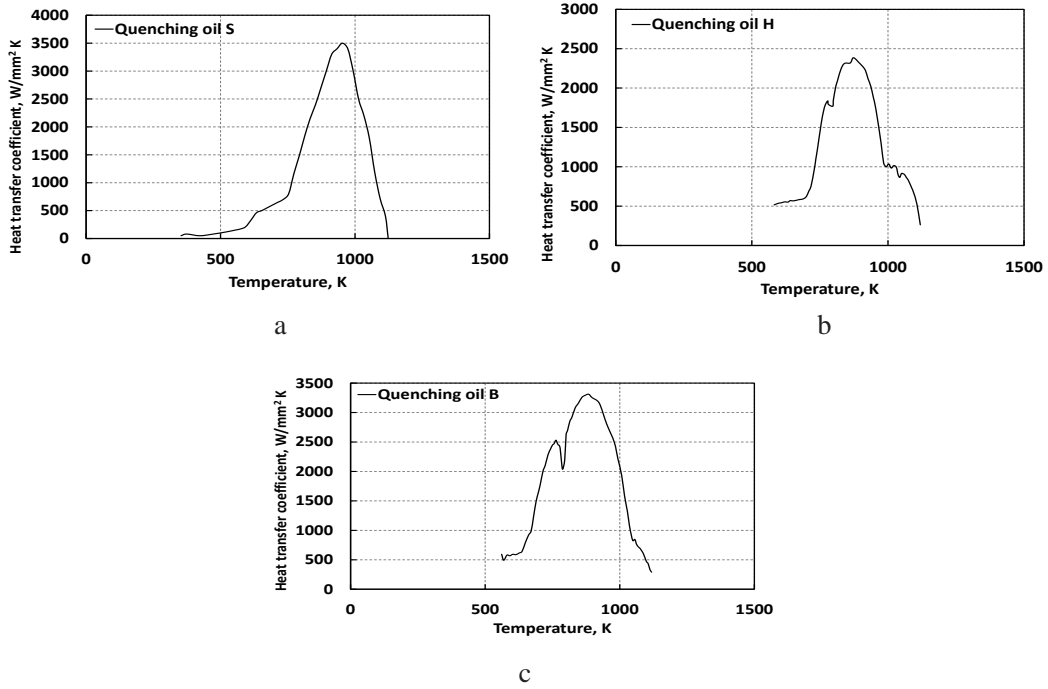
Fig. 3-18 Heat transfer coefficient curves

Carburizing and quenching simulation of cylinder model by three kinds of quenching oil. The simulation results are shown in Table 3-1. The deformation of the cylinder quenched by oil H is minimal. It proved that the oil H is most suitable for this work. It is also proved that Excessive heat transfer rate leads to increased deformation.
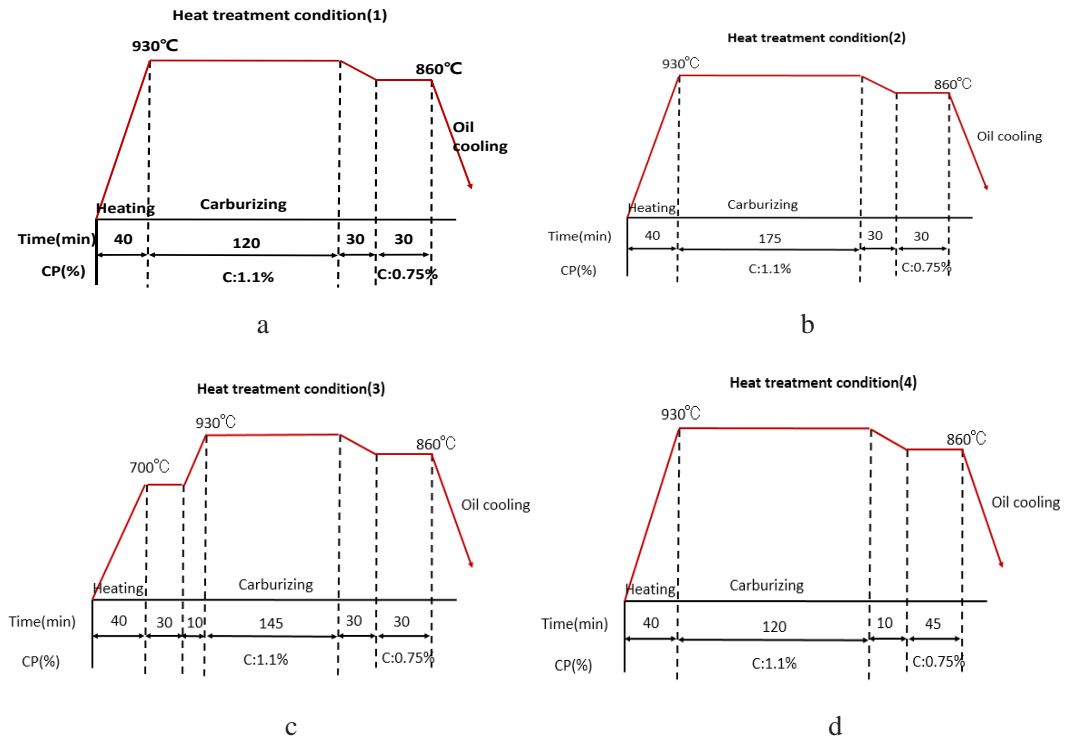

Fig. 3-19 Heat treatments

Table 3-1 Results of deformation with different oils

		Residual stress	Deformation (X)	Deformation (Y)	Deformation
S	1	-231.77	-0.016998~0.011592	-0.048772~0.059849	0.079849
S	2	-216.39	-0.0168~0.012025	-0.048237~0.058704	0.078704
S	3	-235.53	0~0.068356	-0.18513~0.17043	0.12101
S	4	-241.37	-0.015149~0.011083	-0.02992~0.051989	0.081989
H	1	-436.02	-0.017953~0.0038576	-0.044026~0.06666	0.05666
H	2	-423.39	-0.015842~0.0031666	-0.035441~0.054841	0.054841
H	3	-437.39	0~0.041507	-0.10291~0.099914	0.10309
H	4	-446.36	-0.016502~0.0030909	-0.035816~0.056089	0.056089
B	1	+253.51	-0.010761~0.01365	-0.034832~0.062211	0.062211
B	2	+246.26	-0.011285~0.014169	-0.034354~0.062381	0.062381
B	3	+268.98	0~0.052369	-0.10124~0.10587	0.11604
B	4	+271.01	-0.010802~0.013495	-0.034903~0.060083	0.060083

3.6 Concluding remarks

(1) A new mathematical model considering austenite transformation plasticity was first proposed to simulate the residual stress and distortion in software COSMAP.

(2) In consideration of the transformation plasticity coefficient obtained from the experiment, heat treatment simulation analysis was conducted and inelastic stress / strain behavior before and after the transformation was analyzed.

(3) It is proved that considering transformation plasticity will increase the accuracy of the simulation.

(4) It is also proved that Excessive heat transfer rate leads to increased deformation.

References

[1] **Ju, D.-Y. and Inoue, T.,** "On the Material Process Simulation Code COSMAP-Simulated Examples and its Experimental Verification for Heat Treatment Process," *Key Engineering Materials,* 2007, vol. 345-346, pp. 955-958.

[2] **Bowen, R.**, "Continuum Physics, Vol. 3, AC Eringen ed," ed: Academic Press, New York, 1976.

[3] **Callister, W. D. and Rethwisch, D. G.**, *Materials science and engineering: an introduction*. : John Wiley & Sons New York, 2007.

[4] **Inoue, T., Tanaka, T., Ju, D.-Y. and Mukai, R.**, "Transformation plasticity and the effect on quenching process simulation," *Key Engineering Materials*, 2007, vol. 345, pp. 915-918: Trans Tech Publ.

[5] **Ju, D.-Y., Zhang, W. and Zhang, Y.,** "Modeling and experimental verification of martensitic transformation plastic behavior in carbon steel for quenching process," *Materials Science and Engineering: A,* 2006, vol. 438, pp. 246-250.

[6] **Liang, G. and Mudawar, I.,** "Review of spray cooling–Part 2: high temperature boiling regimes and quenching applications," *International Journal of Heat and Mass Transfer,* 2017, vol. 115, pp. 1206-1222.

[7] **Li, H., Li, S., Du, X. and Bao, P.,** "Thermal shock behavior of Cr2AlC in different quenching media," *Materials Letters,* 2016, vol. 167, pp. 131-133.

[8] **Apple, C. and Krauss, G.,** "Microcracking and fatigue in a carburized steel," *Metallurgical Transactions,* 1973, vol. 4, no. 5, pp. 1195-1200.

[9] **Lindig, B. A. and Rodgers, M. A.,** "Rate parameters for the quenching of singlet oxygen by water - soluble and lipid - soluble substrates in aqueous and micellar systems," *Photochemistry and Photobiology,* 1981, vol. 33, no. 5, pp. 627-634.

[10] **Fila, M. and Hulshof, J.,** "A note on the quenching rate," *Proceedings of the American Mathematical Society,* 1991, vol. 112, no. 2, pp. 473-477.

[11] **Murao, Y. and Sugimoto, J.,** "Correlation of heat transfer coefficient for saturated film boiling during reflood phase prior to quenching," *Journal of Nuclear Science and*

Technology, 1981, vol. 18, no. 4, pp. 275-284.

[12] **Grishin, S. and Churyukin, Y. N.,** "Evaluation of the cooling capacity of quenching media based on water," *Metal Science and Heat Treatment,* 1986, vol. 28, no. 10, pp. 744-745.

[13] **Segerberg, S. and Troell, E.**, "High-pressure gas quenching in cold chambers for increased cooling capacity," ASM International, Materials Park, OH (United States)1996.

[14] **Caron, E. J., Daun, K. J. and Wells, M. A.,** "Experimental heat transfer coefficient measurements during hot forming die quenching of boron steel at high temperatures," *International Journal of Heat and Mass Transfer,* 2014, vol. 71, pp. 396-404.

[15] **Osman, A. and Beck, J.,** "Investigation of transient heat transfer coefficients in quenching experiments," *Journal of heat transfer,* 1990, vol. 112, no. 4, pp. 843-848.

Chapter 4 Optimization and verification of carburizing and quenching process of gear

4.1 Introduction

Carburizing quenching process is often used in industry as a method of surface hardening technique to obtain improved mechanical properties and fatigue strength of mechanical components, such as gears, shafts and so on [1-3]. Carburization is the addition of carbon at the surface of low-carbon steels within the austenitic region temperature, which is between 850℃ and 950℃ for carburizing steels generally. Hardening is accomplished when the subsequent high-carbon surface layer is quenched to form martensite so that a high-carbon martensitic case with good wear and fatigue resistance is superimposed on a tough, low carbon steel core [4, 5]. It is very important to select the proper carburizing quenching condition but it is difficult to decide the compromise between maximum hardness and minimum distortion. Computer simulation is very useful for the determination of the quenching condition to obtain the optimum quality [6, 7]. The application of "metallo-thermo-mechanical" theory is capable of describing the interaction among temperature field, stress/deformation field and microstructure changes in quenching [8, 9].

In this chapter, the combination method of orthogonal experiment and numerical simulation is used to optimize the standard heat treatment condition for the minimum distortion after carburizing quenching [10]. A helical gear made of carburizing steel 20MnCrS5 is simulated using three-dimensional coupled analysis based on thermo-mechanical theory. Verify the consistency between experiment and simulation by comparing experimental data with simulated data. Firstly, the improvement of the carbon content and hardness on surface of the gear due to the carburizing quenching process can be verified. The influencing factors of distortion after carburizing quenching are then investigated and discussed. Four influence factors of heat treatment

are selected as follows: carburizing time, the cooling time before 860℃, the holding time at 860℃ and the gear orientation during quenching. The influences of four factors are studied by simulation. Selection of optimal case is then determined by comparing the distortions. Finally, a new optimization method of minimum distortion after carburizing quenching is provided.

4.2 Modelling and conditions

Based on the series of governing equations above, the simulation is used to predict the temperature field, carbon diffusion, phase transformation and distortion during carburizing quenching process. The simulation case in carburizing quenching process is a helical gear made of 20MnCrS5 steel which the carbon content 0.2% and about Chromium 1%. Table 4-1 lists the dimension and main parameters of the gear and Fig. 4-1 shows the 3D finite element model. The total nodes and elements are 75935 and 63455, respectively. Fine meshes concentrate on the surface of the teeth and are used to improve the calculation accuracy where there are steep thermal, stress and carbon gradients. The restrictive conditions are set as shown in Fig. 4-2 (a cross section of the longitudinal axis of the gear). The displacement and rotation in y direction of points a1 and a2 on section plane and the displacement and rotation in z direction of points b1 and b2 are set fixed.

During carburizing quenching, the phenomena such as nucleate boiling and steam film collapses occurring on the surface of the object greatly influences the cooling capacity during the quenching [11]. This causes the heat transfer coefficient on the lower surface of the gear to be different from the other parts of the gear. Therefore, the boundary conditions of thermal transmission are set to distinguish lower surface and other parts shown as the different colors in Fig. 4-2. At the same time, the boundary condition of carburization is set at the surface of the gear.

Table 4-1 Dimension and main parameters of the gear

Gear parameters	Data
Module	1.85mm
Number of tooth	37
Face width	16.9mm
Pressure angle	17.5 °
Helix angle	29 °
Reference diameter	78.263mm
Root diameter	82.95mm
Base diameter	73.625mm
Tooth thickness	2.584mm
Addendum modification facto	1.773
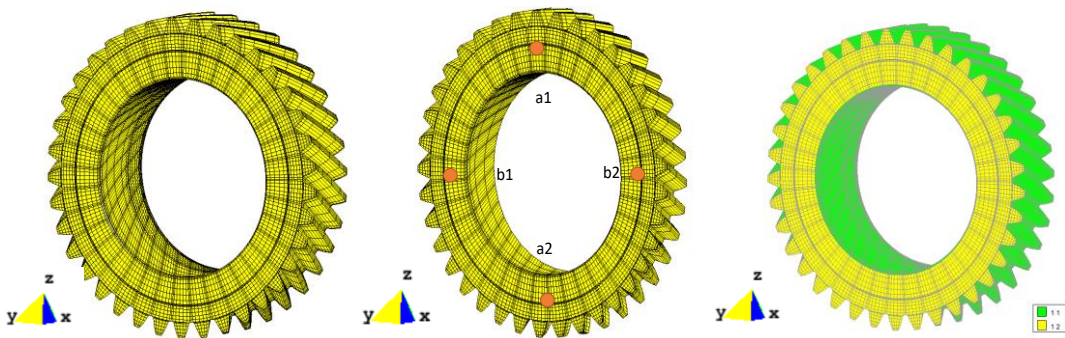
Fig. 4-1 Finite element model   Fig. 4-2 Restrictive conditions and boundary conditions

4.3 Optimized design

The total tooth profile error (Fα) and the total tooth trace error (Fβ) are both important parameters to evaluate the distortion of the gear. Fα is a synthesis of a concave error and a pressure angle error and will both change the gear contact stress distribution law and reduce the stiffness of gear. Fβ will affect the contact between teeth [12, 13]. Meanwhile, the distortion of the gear can be determined from the change of Fα and Fβ before and after carburizing quenching.

It is necessary to eliminate the distortion after the heat treatment. After finish machining, it is important to make sure the surface hardness of the gear is above a certain range. Therefore, we make the flow chart shown in Fig. 4-3 to optimize the process to satisfy the optimization goal: the surface hardness is above 700HV after finish machining.
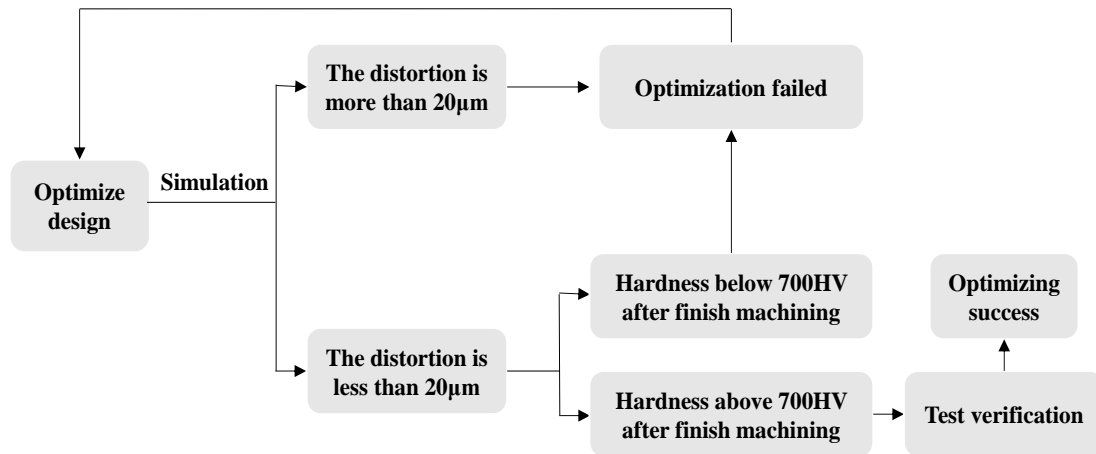
Fig. 4-3 Flow chart of optimization process

Carburization of steel involves a heat treatment of the metallic surface using a source of carbon. Carburization can be used to increase the surface hardness of low carbon steel. According to the diffusion equation described in the previous part of article, increasing the carburizing temperature and carburizing time will reinforce the carburizing effect and at the same time will increase grain growth and deformation. Insufficient carburizing depth and surface carbon phenomenon occurs with low carburizing temperature and short carburizing time [14-16]. The method of carburizing with high-carbon potential and cooling diffusion is used to solve this contradiction. Therefore, heat treatment process shown in Fig. 4-4 is adopted. The sample is heated to 930℃, carburized at high temperature for a period of time, and then cooled at a certain speed to 860℃ and held for a while, finally quenched into oil.

The phenomena of nucleate boiling and steam film collapses causes the heat transfer coefficient on the lower surface of the gear to be different from the other parts of the gear. It not only changes the heat transfer rate, also affects the distribution of temperature changes, thus affecting the distortion after quenching. Using the same method in the reference, the heat transfer coefficient used for simulation as the surface boundary condition is inversely identified [17].

Therefore, the four parameters (carburizing time, the cooling time before 860℃, the holding time at 860℃ and the gear orientation during quenching) have a great influence on the distortion after heat treatment.
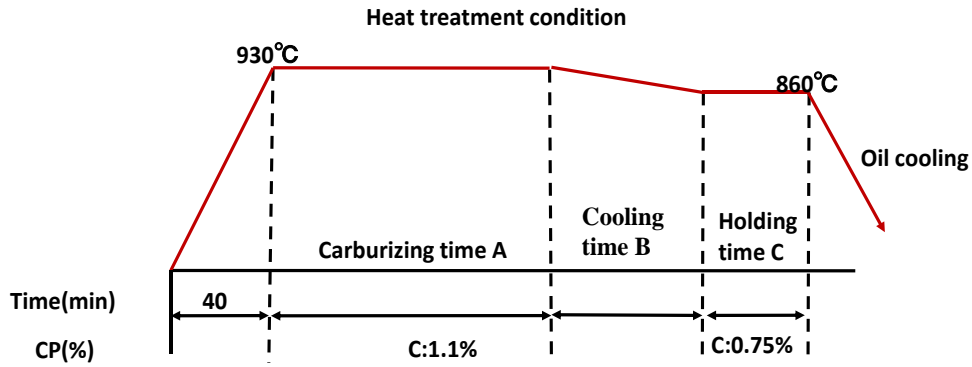
Fig. 4-4 Influence factors of the heat treatment (A, B, C)

The heat transfer coefficients of the surfaces are determined with the gear orientation of $0°$, $30°$, and $60°$, respectively shown in Fig. 4-5. The identified heat transfer coefficients are shown in Fig. 4-6
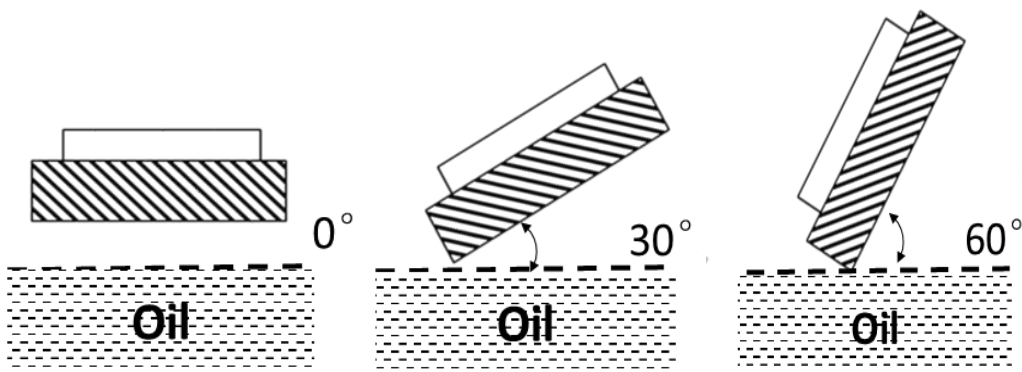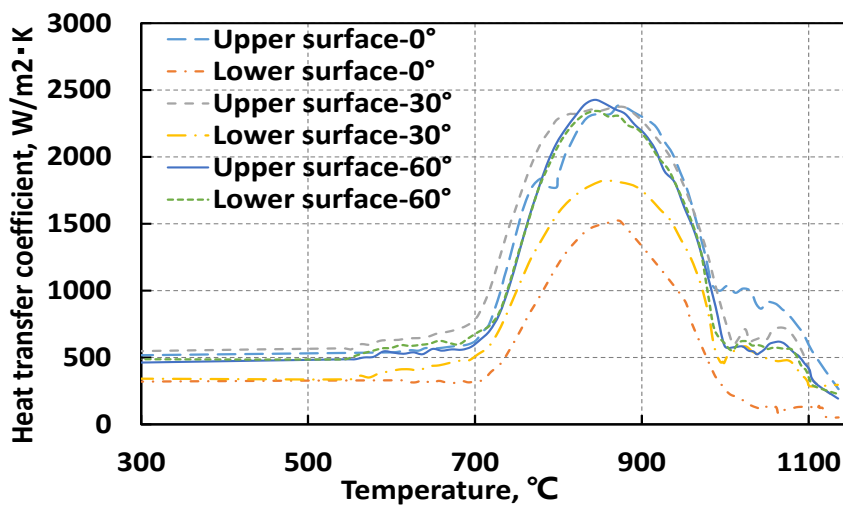

Fig. 4-5 Influence factor of the heat treatment (D)

Fig. 4-6 Heat transfer coefficient curves

4.4 Process optimization by orthogonal experimental

In order to optimize the heat treatment conditions to obtain the best conditions, the orthogonal experiment method is used. The tooth distortion can be determined from the change of Fα and Fβ before and after carburizing quenching as Fig. 4-7. Since the distortion of tooth trace is larger than the distortion of profile according to the calculation result shown later, the distortion of tooth trace are used to optimize the processes. Four influence factors of heat treatment are selected as shown in Fig. 4-4 and Fig. 4-5: carburizing time, the cooling time before 860℃, the holding time at 860℃ and the gear orientation during quenching. Each influence factor takes 3 levels. The 4 factors and their 3 level values are shown in Table 4-2.

Choosing orthogonal table is the most important issue in orthogonal design. After the factors and their levels are determined, appropriate orthogonal table can be chosen by considering the number of interaction between the factors from different levels [18]. The rule of choosing an orthogonal table is choosing the smaller orthogonal as much as possible in order to reduce the number of tests in the premise of the factors and their interaction can be arranged. Generally speaking, the number of levels in experimental factors should be equal to the number of levels in orthogonal table. The number of factors (including interactions) should not exceed the number of the orthogonal table's columns. In order to optimize the processes to obtain the minimum distortion, $L_9(3^4)$ is chosen as the orthogonal table to arrange the orthogonal design. The parameters of every test are shown in Table 4-3.

The calculation processes of mean and range are not presented, and the results are listed in the table. Ki is the sum of the distortion values in the i level. The order of the factors is listed according to the size of ranges. The larger the range is, the more influence on test result the level change of this factor has.

The results in Table 4-3 show that the order of factors influence level is D>A> C> B, namely the gear orientation during quenching> carburizing time> the holding time at 860℃> the cooling time before 860℃. The gear orientation during quenching is the

uppermost, while the cooling time before 860℃ is the unimportant. Selection of optimal case is determined by the research index which is the distortion of tooth trace. From the result, the optimal combination of factors and levels is $A_1B_3C_3D_3$, namely carburizing time (120min), cooling time before 860℃ (30min), holding time at 860℃ (45min) and the gear orientation during quenching (60°). The optimal condition is shown in Fig. 4-9.

Table 4-2 Influence factors and level values

Level	Carburizing time A	Cooling time before 860℃ B	Holding time C	the gear orientation D
1	120min	10min	15min	0°
2	175min	20min	30min	30°
3	230min	30min	45min	60°

Table 4-3 Orthogonal experiment of the distortion of tooth trace

Text number	A	B	C	D	Average distortion of
1	1(120min)	1(10min)	1(15min)	1(0°)	11.54
2	1(120min)	2(20min)	2(30min)	2(30°)	8.54
3	1(120min)	3(30min)	3(45min)	3(60°)	7.54
4	2(175min)	1(10min)	2(30min)	3(60°)	8.26
5	2(175min)	2(20min)	3(45min)	1(0°)	10.86
6	2(175min)	3(30min)	1(15min)	2(30°)	9.26
7	3(230min)	1(10min)	3(45min)	2(30°)	9.67
8	3(230min)	2(20min)	1(15min)	3(60°)	8.95
9	3(230min)	3(30min)	2(30min)	1(0°)	11.45
K1	27.62	29.47	29.75	33.85	
K2	28.38	28.35	28.25	27.47	
K3	30.07	28.25	28.07	24.75	
Range R	2.45	1.22	1.67	9.1	
Order			D>A>C>B		
Optimal level	A1(120min)	B3(30min)	C3(45min)	D3(60°)	
Optimal combination			A1B3C3D3		

Tooth tip

Tooth root

Total tooth profile error (Fα)

Tooth trace

Hardness measurement position
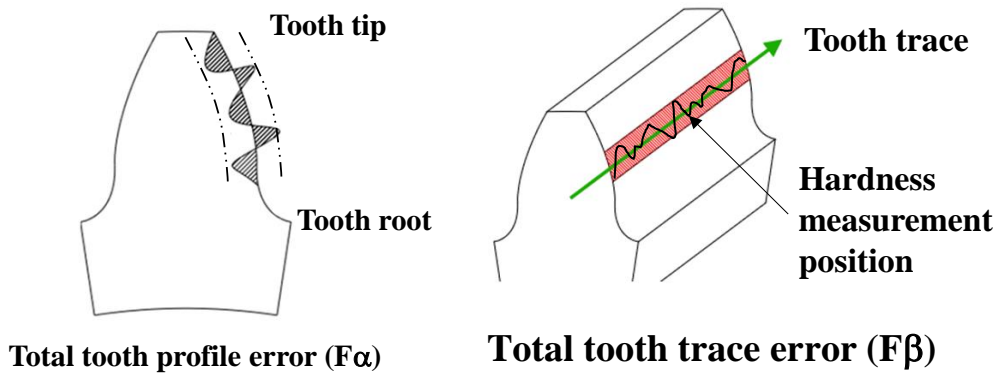
Total tooth trace error (Fβ)

Fig. 4-7 Tooth distortion after carburizing quenching

4.5 Results of experiment and simulation

4.5.1 Distortion of the Gear after Quenching

The standard heat treatment condition (S) is shown in Fig. 4-8 and the optimized condition (O) is shown in Fig. 4-9. The distortion of the gear can be determined from Fα and Fβ before and after carburizing quenching. Fig. 4-10 shows the simulated and measured distortion values of tooth profile after carburizing quenching. The simulation results verify the trend of the experimental results well and they are very close to the experimental results. Both simulation and experiment show that the distortion of tooth profile after the heat treatment O is smaller. It proves that condition O can achieve a smaller distortion of tooth profile comparing with condition S.

Fig. 4-11 shows the calculated and measured distortion values of tooth trace after carburizing quenching. The calculated distortions of gears are in good agreement with the measured values.   As the characteristics of the results, the distortion of tooth trace is larger than that of distortion of tooth profile. It proves that condition O can achieve a smaller distortion of tooth trace comparing with condition S. It can be observed that the maximum distortion of the gear with condition S is more than 20μm and the maximum distortion with condition O is less than 20μm. From this result we can confirm that the finished cutting thickness is 20μm. It is the reason for the parameters setting in Fig. 4-3. Comparing to the values in the Table 3, the distortion with condition O is less than any other value. It proves that the minimum distortion can be obtained with the
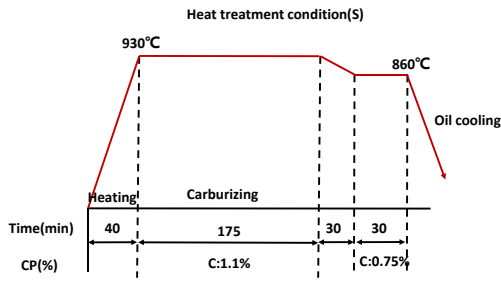
optimized condition.

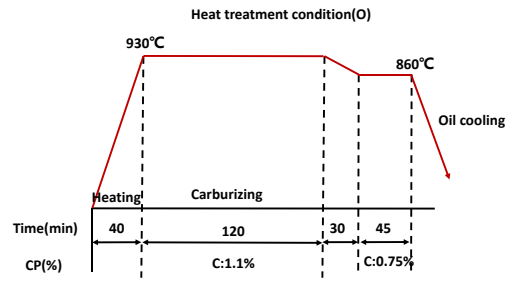Fig. 4-8 Standard condition (S)   Fig. 4-9 Optimal condition (O)
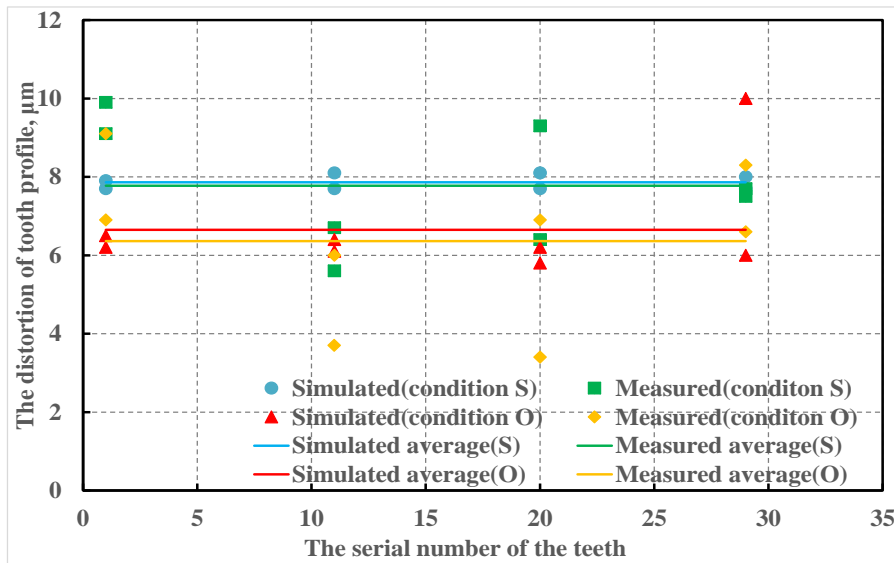

Fig. 4-10 Comparison of the tooth profile distortion between experimental value and calculated
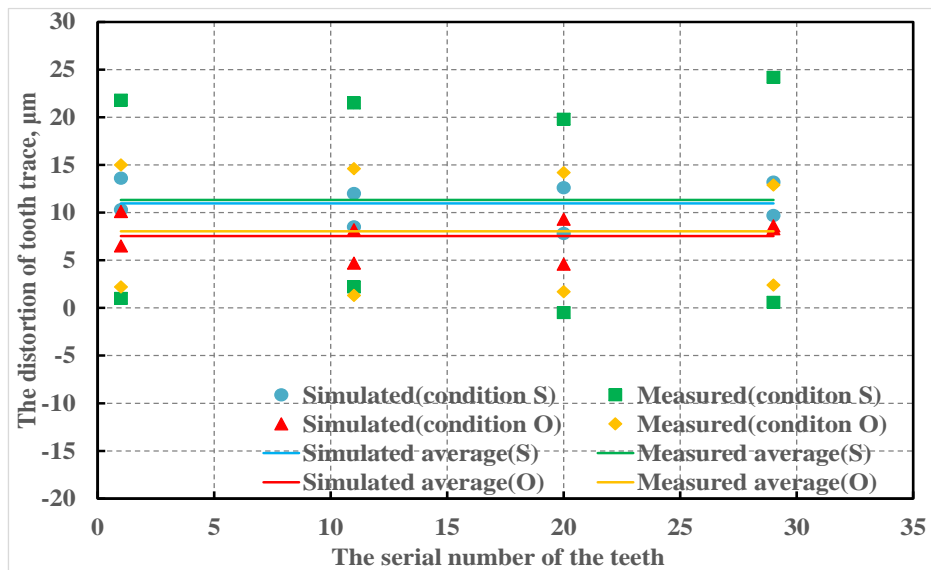
value

Fig. 4-11 Comparison of the tooth trace distortion between experimental value and calculated

value

4.5.2 Hardness Distribution

The difference of carbon content at the surface and inside of the gear after carburizing quenching process will result in martensite layer with a high hardness [16]. The hardness measurement position is at the tooth trace shown in Fig. 4-7. With condition S the hardness distribution in the near surface layers of measured and calculated results is shown in Fig. 4-12. From the results, it can be observed that after carburizing quenching the surface hardness is about 730HV and the maximum hardness is at the surface. With increasing depth, the values of the hardness are decreased gradually. The heat treatment condition S does not satisfy the optimization goal because the hardness in the depth of 20μm of the gear is less than 700HV.

With condition O the hardness distribution in the near surface layers of measured and calculated results is shown in Fig. 4-13. Comparing with the result of condition S, both simulation and experiment results show that the hardness of the gear surface with condition O after heat treatment is higher. It proves that the hardness of the gear with condition O is higher than 700HV in the depth of 20μm. Therefore, the heat treatment condition O satisfies the optimization goal.
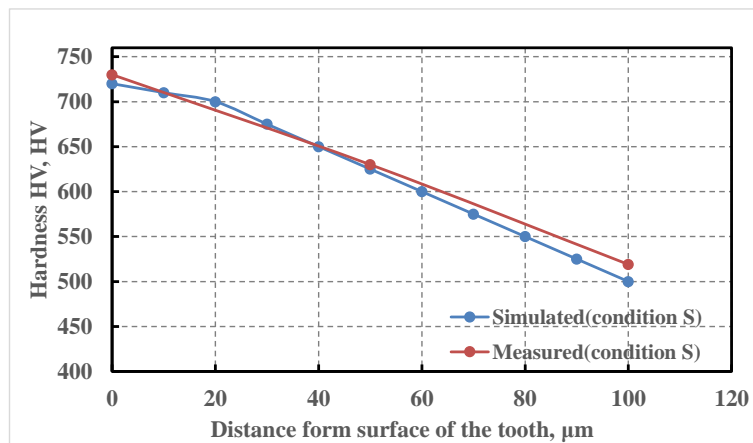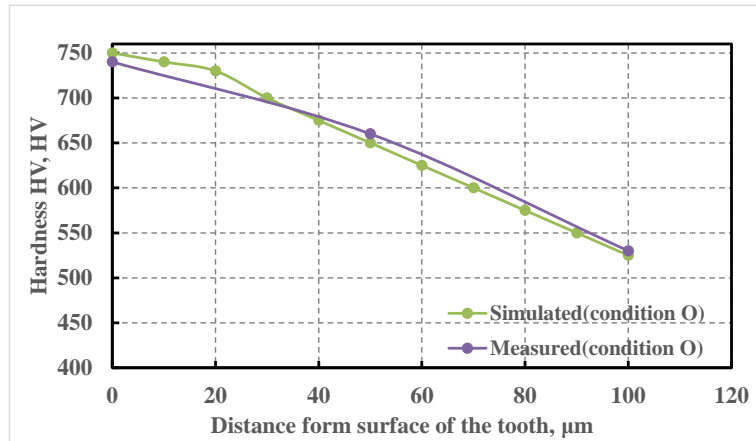

Fig. 4-12 Hardness distribution with condition S

Fig. 4-13 Hardness distribution with condition O

4.6 Conclusion remarks

The carburizing quenching process and the distortion of a gear are simulated based on the metallo-thermo-mechanical theory. From these results, we obtained some useful conclusions:

(1) Selection of optimal cases are determined by the indexes of the distortion of tooth trace. The optimal case determined by the distortion of tooth trace is carburizing time (120min), cooling time before 860℃ (30min), holding time at 860℃ (45min) and the gear orientation during quenching (60 °).

(2) Concerning to the distortion of tooth trace, the order of factors influence level is the gear orientation during quenching > carburizing time> the holding time at 860℃> the cooling time before 860℃.

(3) The measured results concerning hardness and distortion are in good agreement with the simulated values.

(4) It is proved that the minimum distortion of the gear can be obtained with the optimized condition. Meanwhile, the optimized condition satisfies the optimization goal.

References

[1] **Li, W. and Liu, B.,** "Experimental investigation on the effect of shot peening on contact fatigue strength for carburized and quenched gears," *International Journal of Fatigue,* 2018, vol. 106, pp. 103-113.

[2] **Nojima, K., Ogata, K., Tanaka, M., Nishi, R., Ono, Y. and Koide, T.,** "Bending fatigue strength of case-carburized helical gears (In the case of large helix angles)," *Journal of Mechanical Science and Technology,* 2017, vol. 31, no. 12, pp. 5657-5663.

[3] **Mukai, R. and Ju, D.-Y.,** "Simulation of carburizing-quenching of a gear. Effect of carbon content on residual stresses and distortion," *Journal de Physique IV (Proceedings)*, 2004, vol. 120, pp. 489-497: EDP sciences.

[4] **Ju, D., Sahashi, M., Omori, T. and Inoue, T.**, "Residual stresses and distortion of a ring in quenching-tempering process based on metallo-thermo-mechanics," ASM International, Materials Park, OH (United States)1996.

[5] **Zhang, X., Tang, J.-y. and Zhang, X.-r.,** "An optimized hardness model for carburizing-quenching of low carbon alloy steel," *Journal of Central South University,* 2017, vol. 24, no. 1, pp. 9-16.

[6] **Hussein, A. K., Abbas, L. K. and Hameed, A. K.,** "Effect of Carburization Parameters on Hardness of Carburized Steel Using MOORA Approach," *Al-Khwarizmi Engineering Journal,* 2018, vol. 14, no. 3, pp. 92-99.

[7] **Byun, J., Byun, S. and Yi, C.,** "A study on SCr420HB helical gear deformative simulation by heat treatment quenching method," *Journal of the Korean Society for Heat Treatment,* 2015, vol. 28, no. 1, pp. 24-31.

[8] **Liu, Y. G., Zhang, Y., Zhang, W., Li, J. W., Wang, H. B., Gu, H. R. and Jin, J. C.**, "Investigation of hot stamping process of 22MnB5 based on metallo-thermo-mechanical theory," *Advanced Materials Research*, 2015, vol. 1063, pp. 251-256: Trans Tech Publ.

[9] **Zhang, W., Liu, Y., Gu, H., Jin, J., Zhang, Y., Li, J. and Wang, H.**, "Metallo-Thermo-Mechanical Coupled Analysis of the Influence of Key Process Parameters on

the Quality of Hot Stamping Component," *Advanced High Strength Steel and Press Hardening*, 2016, pp. 281-287: World Scientific.

[10] **WANG, J.-q. and ZHAO, C.,** "Process Optimizing about Low Temperature Plasma Carburizing of AISI 304 Austenitic Stainless Steel [J]," *Heat Treatment Technology and Equipment,* 2010, vol. 1.

[11] **Murao, Y. and Sugimoto, J.,** "Correlation of heat transfer coefficient for saturated film boiling during reflood phase prior to quenching," *Journal of Nuclear Science and Technology,* 1981, vol. 18, no. 4, pp. 275-284.

[12] **Uematsu, S. and Kato, M.,** "Involute Profile Error in Finish Roll Forming of Spur Gears-Formation of Pressure Angle Error," *Transactions of the Japan Society of Precision Engineering,* 1989, vol. 55, pp. 1839-1844.

[13] **Uematsu, S.,** "How to Occur Involute Profile Error in Finish Roll Forming of Spur Gears," *Transactions of Japan Society of Precision Engineering,* 1988, vol. 54, no. 1, pp. 139-144.

[14] **Nová, I. and Machuta, J.,** "Monitoring of the Diffusion Processes during Carburizing Automotive Steel Parts," *Manufacturing Technology,* 2016, vol. 16, no. 1, pp. 225-230.

[15] **Peng, Y., Gong, J., Chen, C., Liu, Z. and Jiang, Y.,** "Numerical analysis of stress gradient and traps effects on carbon diffusion in AISI 316L during low temperature gas phase carburization," *Metals,* 2018, vol. 8, no. 4, p. 214.

[16] **Tao, Q., Wang, J., Fu, L., Chen, Z., Shen, C., Zhang, D. and Sun, Z.,** "Ultrahigh hardness of carbon steel surface realized by novel solid carburizing with rapid diffusion of carbon nanostructures," *Journal of materials science & technology,* 2017, vol. 33, no. 10, pp. 1210-1218.

[17] **Mukai, R., Matsumoto, T., JU, D.-y., Suzuki, T., Saito, H. and Ito, Y.,** "Modeling of numerical simulation and experimental verification for carburizing-nitriding quenching process," *Transactions of Nonferrous Metals Society of China,* 2006, vol. 16, pp. s566-s571.

[18] **Zhu, J., Chew, D. A., Lv, S. and Wu, W.,** "Optimization method for building envelope design to minimize carbon emissions of building operational energy consumption using orthogonal experimental design (OED)," *Habitat International,* 2013, vol. 37, pp. 148-154.

Chapter 5 Verification of fatigue strength by optimum process

5.1 Introduction

Since failure caused by repeated loading accounts for at least half of all mechanical failures, the fatigue performance is prime importance for the materials, which are subject to cyclic loading [1, 2]. Carburizing and quenching process is widely used in industry, as a method of surface hardening technology to obtain improved mechanical properties and fatigue strength of mechanical components, such as gears, shafts and so on [3-5]. The main advantages of carburizing are that they can achieve high surface hardness, compressive residual stress and good toughness at the core, which can effectively improve the surface strength, wear resistance and fatigue strength of the steel [6-8].

It is well known that many performances can affect the fatigue resistance of carburized parts. One of the important performances is the distribution of residual stresses [9]. The compressive residual stresses counteract the applied tensile stresses and therefore improve the fatigue performance. The ideal hardness distribution shifts the failure initiation point transfer from the core to the surface. Therefore, in order to obtain maximum gain in fatigue resistance, the hardness distribution should be kept in a certain range depending on the thickness and size of the specimen [10]. Core microstructure is also one of these performances. Lower carbon content of core increases the fatigue resistance, particularly due to the enlarged compressive residual stresses at the surface, compared with the cases of higher carbon content [11]. The refinement of austenitic grain size is also one of these performances, which results in a fine martensitic structure and/or reduced size and density of micro cracks in the structure produce better fatigue resistance [12, 13]. Many factors such as carburizing time and temperature during the various stages of a carburizing process affect the performance above [14, 15]. It is necessary to determine the relationship between the

carburizing process factors and the material performances.

5.2 Experimental procedure

5.2.1 Heat treatment process

Increasing the carburizing temperature and carburizing time will reinforce the carburizing effect but increase domain growth and distortion. On the other hand, insufficient carburizing depth and surface carbon phenomenon occurs with low carburizing temperature and short carburizing time [16, 17]. Therefore, the method of carburizing with high-carbon potential and low temperature diffusion is used to solve this contradiction. Heat treatment condition A shown in Fig. 5-1(a) is a standard carburizing and quenching process which is often used. Heat treatment condition B shown in Fig. 5-1(b) reduces carburization time and increases diffusion time. It is summarized from the previous optimization work it can achieve minimal distortion [18].
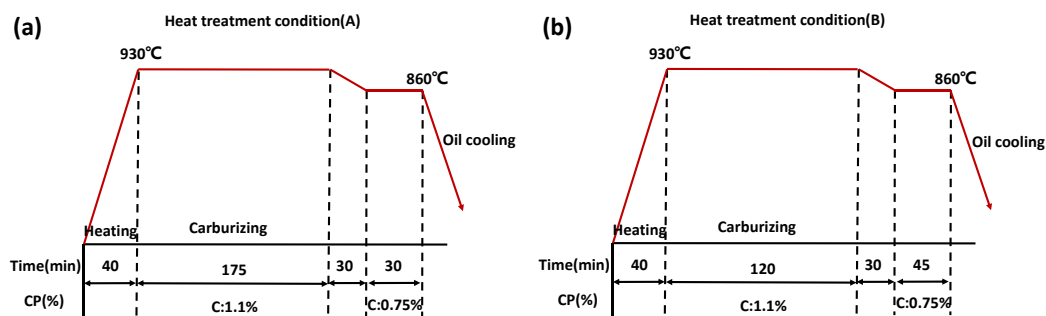
Fig. 5-1 Heat treatment conditions: a – standard condition; b – optimized condition

5.2.2 Material and preparation specimens

A finite element program called COSMAP is developed to predict the temperature field, carbon diffusion, phase transformation, hardness and residual stress during carburizing and quenching process [19]. The size of the specimens is 50 mm $\times$ 50 mm $\times$ 80 mm. The total nodes and elements of model are 9261 and 8000, respectively. Fine meshes concentrate on the surface of the specimen and are used to improve the calculation accuracy where there is steep thermal, stress and carbon gradients.

The chemical compositions of the 20MnCrS5 steel is shown in Table 5-1. The

results of the simulation at surface and cross section are shown in Fig. 5-2. The distribution gradient of the carbon content from surface to the core due to the carbon diffusion can be observed. At the surface, the carbon content reaches 0.75 %. Inside the specimen, the carbon content still keeps low. In addition, the carburizing depth is about 800μm. The differences of the carbon content from surface to core after carburizing process has a great effect on the phase transformations and result in martensite layer with a high hardness. The distribution gradient of the hardness and residual stress from surface to the inside can also be observed.

According to the results of simulation, the carburized layer, subsurface layer and central layer are selected as representative parts to be sliced from the specimens as shown in Fig. 5-3.

Table 5-1:   The chemical compositions of 20MnCrS5 steel by wt%

Material	C	Si	Mn	Cr	Mo
20MnCrS5	0.2	0.2	1.2	1.2	-
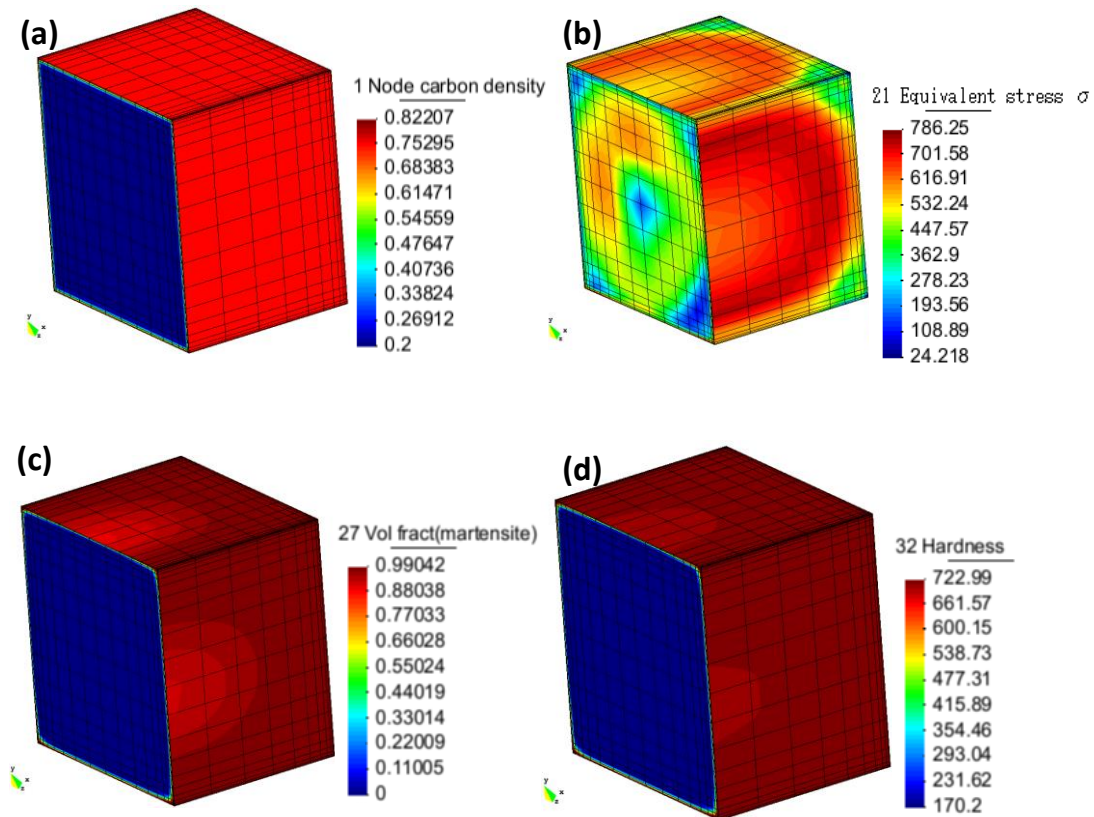
Fig. 5-2 Simulation during carburizing and quenching: (a) Distribution of carbon (b) Distribution of equivalent stress (c) Distribution of martensite (d) Distribution of hardness
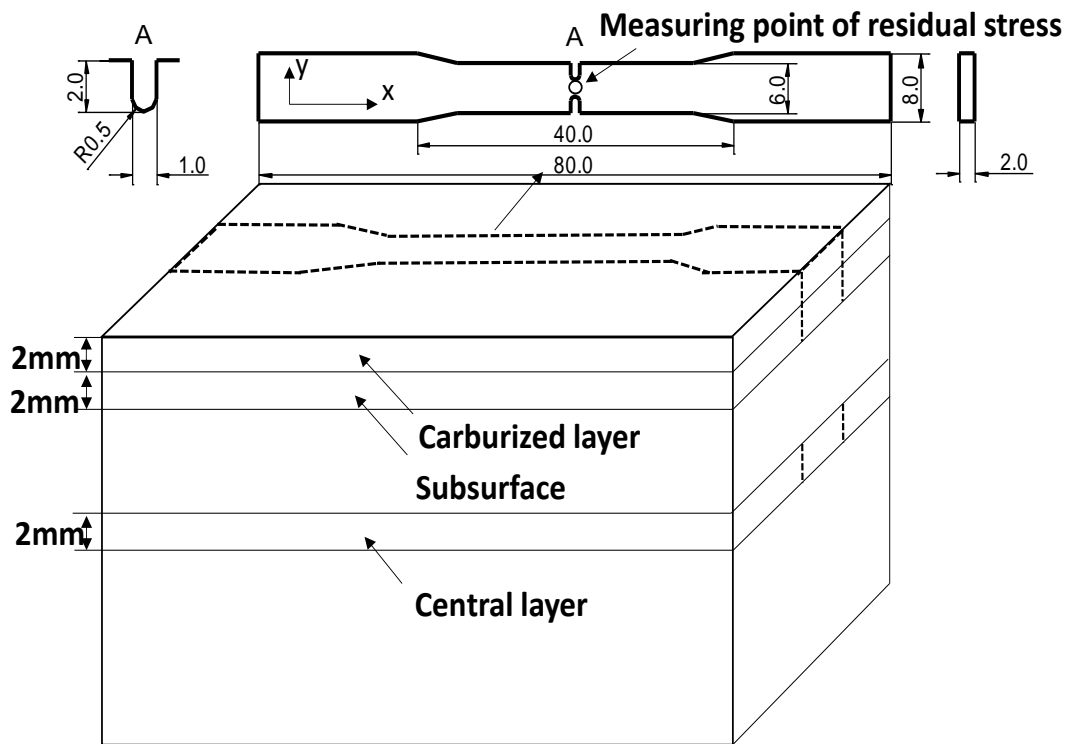
Fig. 5-3 Method of slicing and measuring

5.3 Results and discussion

5.3.1 Microstructure

5.3.1.1 Microstructure of 20MnCrS5-heat treatment process B

The cross section of the specimens was first grounded and polished and then the surfaces of the microstructure observation points are eroded with a solution of 4 % HNO_3 + 96% C_2H_5OH, the microstructures at different depth from the surface are finally observed by OM. The metallographic structure at different positions of the cut surface of the sample after heat treatment is shown in the figure below.

Fig. 5-4 shows the metallographic structure of the surface of the sample, and it can be seen that the carburization depth is about 1000μm. The surface is needle-shaped martensite structure.
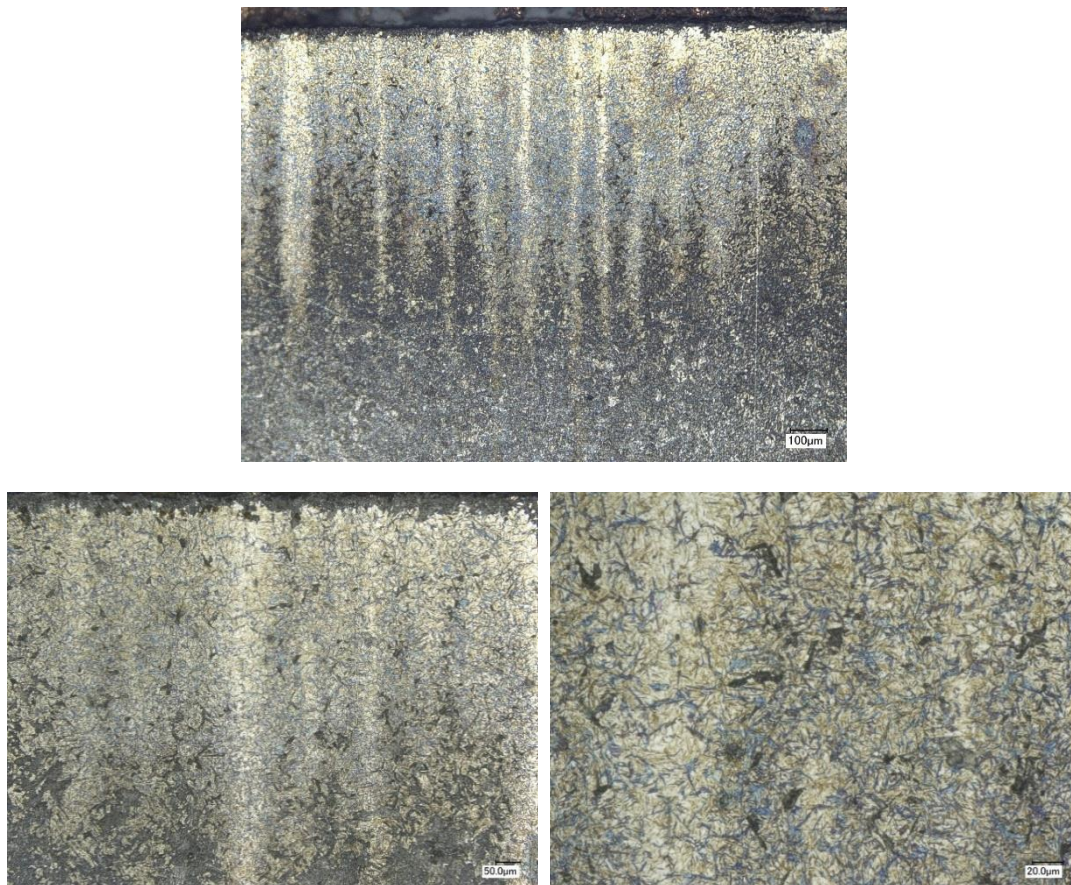
Fig. 5-4 Microstructures of carburized layer with condition B

Fig. 5-5 shows the metallographic structure of the subsurface of the sample, which is the staggered position of the carburized layer and the substrate. The carburized structure is needle-shaped martensite; the non-carburized part is near the surface of the martensite, and gradually transitions to bainite.
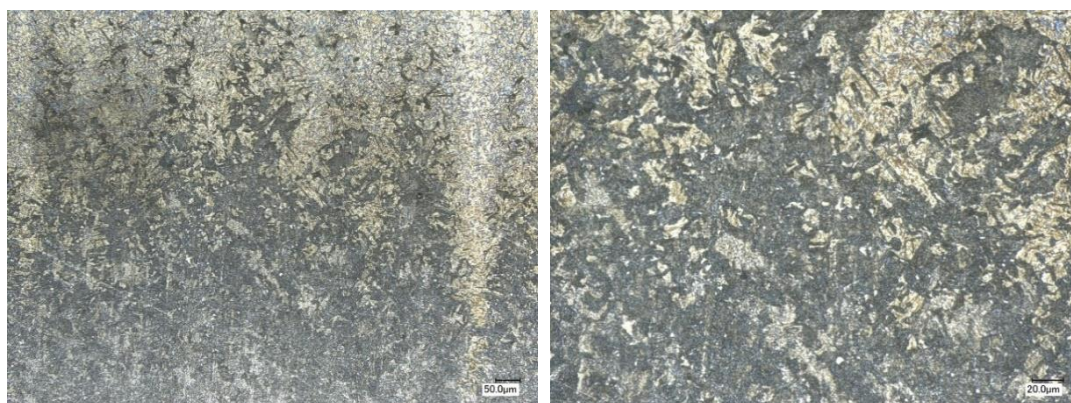

Fig. 5-5 Microstructures of carburized layer with condition B

Fig. 5-6 shows the metallographic structure of the center of the sample. Since the

core has a low cooling rate, the core structure is bainite with a small amount of pearlite structure.
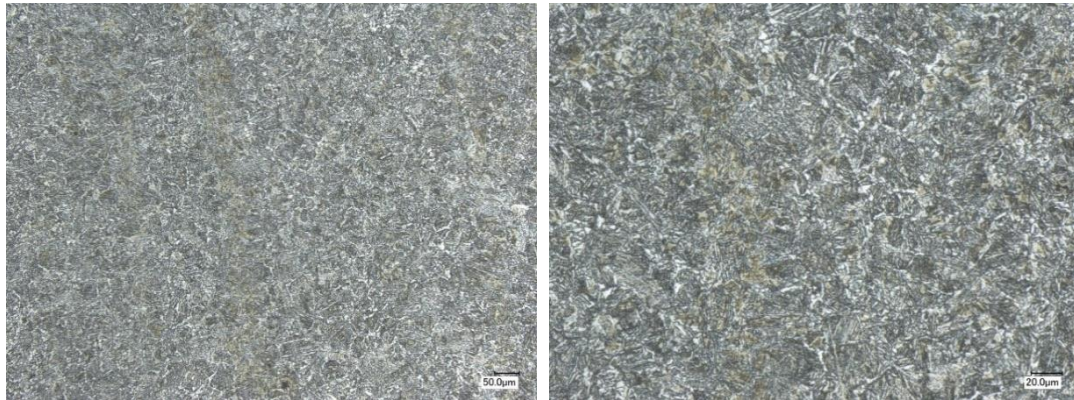

Fig. 5-6 Microstructures of central layer with condition B

According to the distribution of the tissue, the influence of the surface carburized layer was demonstrated, and the surface exhibited high hardness due to the acicular martensite. As the depth increases, it gradually transitions to bainite structure, and the hardness is slightly reduced while showing good toughness.

5.3.1.2 Microstructure with different conditions

The measured results show good agreement with the simulated results. As shown in Fig. 5-7 (a) and Fig. 5-7(b) the microstructure of carburized layer after carburizing and quenching are mainly acicular martensite, retained austenite and fine carbide particles. It can be observed that Fig. 5-7(b) has finer microstructure and less retained austenite. Since the diffusion time of condition B is increased, it facilitates the precipitation of carbon in the retained austenite with the form of carbide. It caused a decrease in the stability of the austenite, which was beneficial to the transformation of the retained austenite. Hence, the decrease of the retained austenite led to a harder surface. As shown in Fig. 5-7(c) and Fig. 5-7(d), the microstructure is to form pearlite structure at central layers. Besides the pearlite structure, small portions of other phases, such as bainite are present. They can retain the strength and toughness of the core. It can be considered that the microstructure with condition B is more beneficial to improve the wear resistance and fatigue strength than that by using the conventional
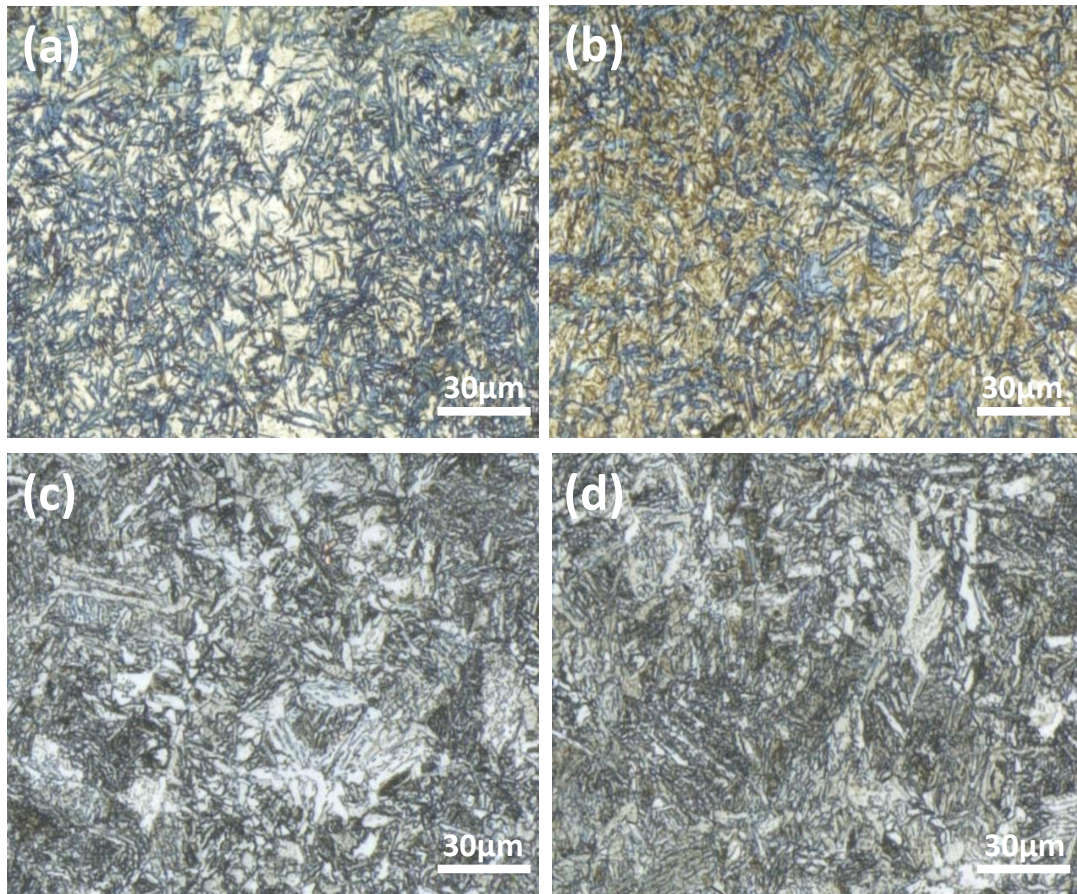
way.

Fig. 5-7 Microstructures with different heat treatment conditions: (a) carburized layer with condition A (b) Subsurface layer with condition B (c) Central layer with condition A (d) Central layer with condition B

5.3.2 Analysis of component distribution

The cross section of the specimens was first grounded and polished and then the surfaces of the microstructure observation points are eroded with a solution of 4 % HNO_3 + 96% C_2H_5OH, the microstructures at different depth from the surface are finally determined by EPMA. The composition distribution at different positions of the cut surface of the sample after heat treatment is shown in the figure below.

The distribution of components in the above parts were analyzed, the distribution of components of gear steel after heat treatment, the forms of several compounds and the effect of these forms on gear strength are analyzed.

It can be seen from the results of Fig. 5-8 that SiC compounds (forming new phase

tissue) appear on the carburized surface, and the remaining components are basically uniform. Generally, SiC compounds have higher hardness, so they can improve the surface hardness and yield strength as well as tensile strength. However, since they are brittle compounds, they have negative effects on the fatigue life of materials. At the same time, stress and strain concentration occurs at the interface of the SiC compound, which is one of the reasons for the negative effect on the tensile fatigue.
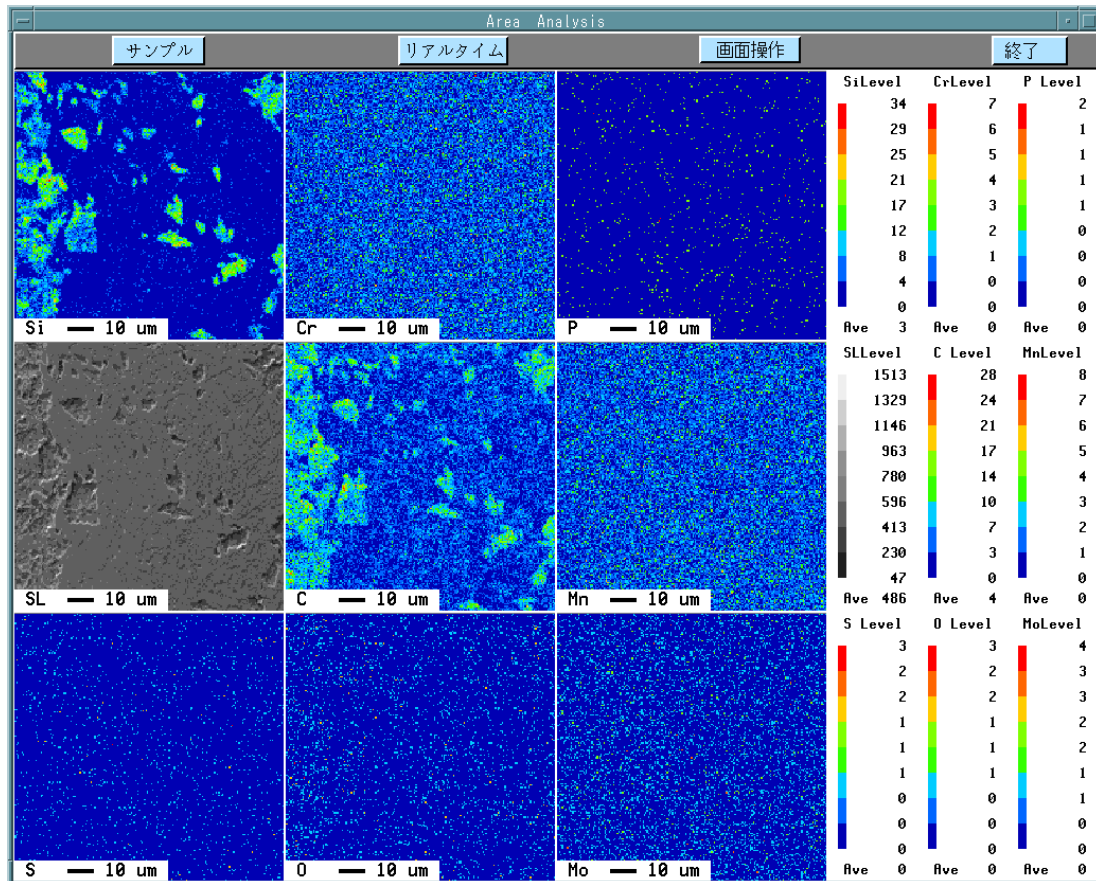

Fig. 5-8 EPMA mapping of the carburized layer (Condition A)

According to the results of Fig. 5-9, it can be seen that SiC compounds still appear at the interface between the carburized layer and the substrate, but the surface distribution is well-distributed, the remaining ingredients are also basically uniform. Therefore, the hardness in the carburized layer will increase, but the material tensile fatigue life has a slight negative effect. For yield stress, the effect of tensile strength is the same as Fig. 5-8, however, the new phase interface of the SiC compound appearing here is not obvious, so the stress strain at the interface is concentrated, and the stress

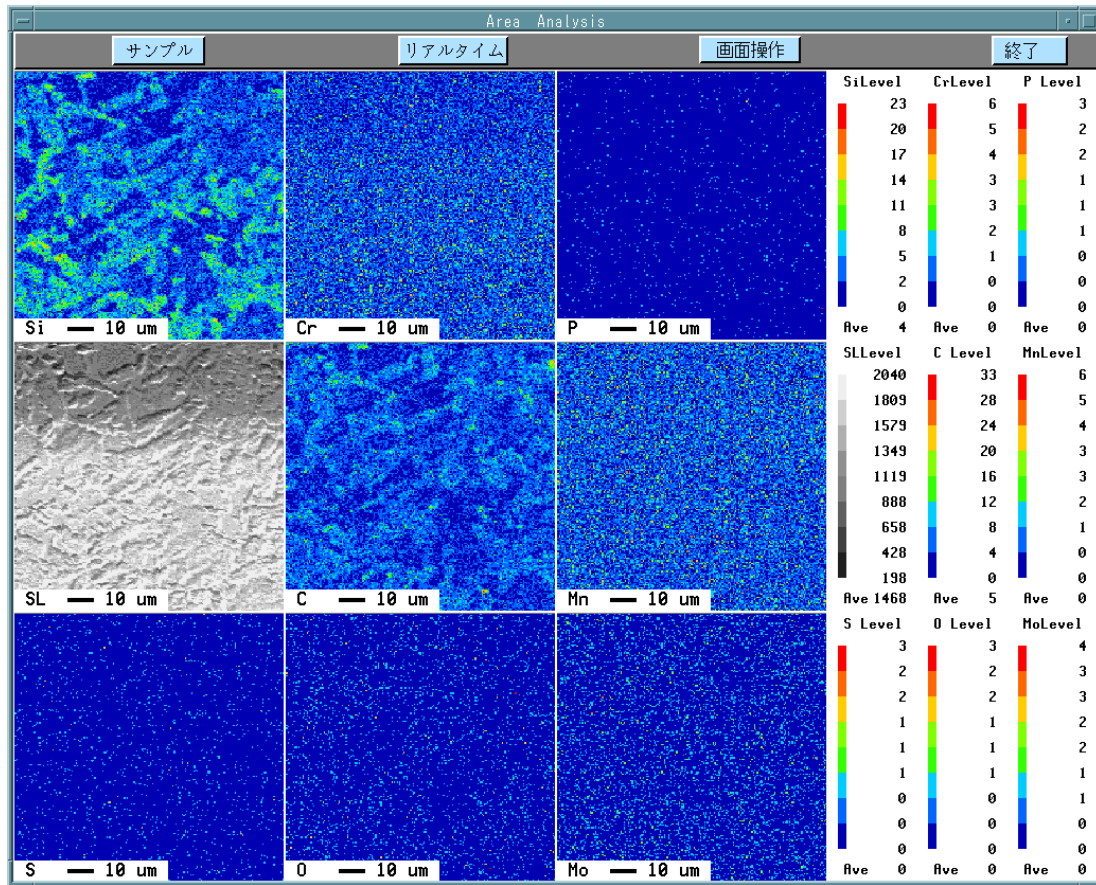and strain of the whole is in a transient distribution state.

Fig. 5-9 EPMA mapping of the subsurface layer (Condition A)

It can be seen from the results of Fig. 5-10 that there is substantially no SiC compound, which indicates that the SiC compound is not produced when the material is also metallurgically prepared, however, due to the increase in C concentration due to carburization, it is estimated that the Si content in Baosteel's substrate is high, so it is easy to form SiC compound. In addition, the composition was found to be substantially uniform inside the substrate. SiC compounds generally have higher hardness and therefore have an effect on the hardness of the surface layer. However, due to a new phase belonging to the MnS compound, there are two possibilities for the presence of MnS compounds, one is the possibility of smelting, and the other is Formation after heat treatment. According to the previous results analysis, the first one is more likely. Since the MnS compound is present inside, if the MnS is a small particle dispersion form, it will be beneficial to the toughness of the material. However, the results show a

flat shape after a 30 micron long bundle of micrometers. Generally, the water may have a negative effect on the strength, but since it is in the core, it should not have much influence on the strength. At the same time, the new phase of the MnS compound in the core generally does not have much effect on the yield strength and tensile strength of the material. However, the interface of the new phase of the MnS compound is obvious, and stress and strain concentration will occur. Since it is generated inside, it has little effect on the fatigue life and strength of the finishing.
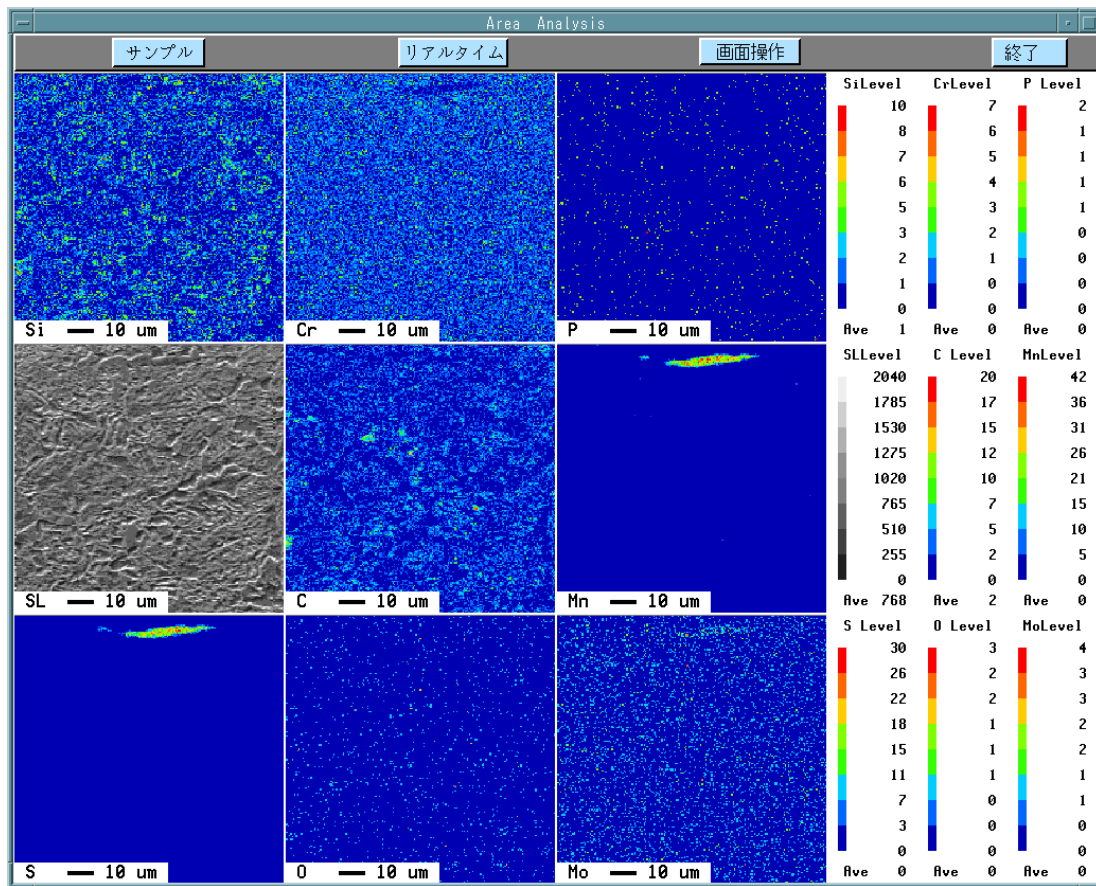

Fig. 5-10 EPMA mapping of the central layer (Condition A)

As shown in Fig. 5-11, it is found that the results of the carburizing and quenching heat treatment condition 4 are significantly different from those of the heat treatment condition 2. First, SiC compound was not found at the surface layer, indicating that the temperature was reduced from 930 degrees to 860 degrees in 10 minutes after carburization, so that the SiC compound was too late to form, but FeC compounds appeared in the surface layer. And the shape is small, round, but not uniform. If the FeC

compound is fine and evenly distributed, it will also act as a dispersion strengthening. Unfortunately, the current results are difficult to give a judgment that greatly contributes to the strength. Since the other ingredients are basically uniform, it should be said that the organizational structure is still good. Since the FeC compound is finely spherical and uniformly distributed, it should be said that it has an effect of enhancing the yield strength and the tensile strength, and does not cause stress and strain concentration, and it is also advantageous for fatigue life.
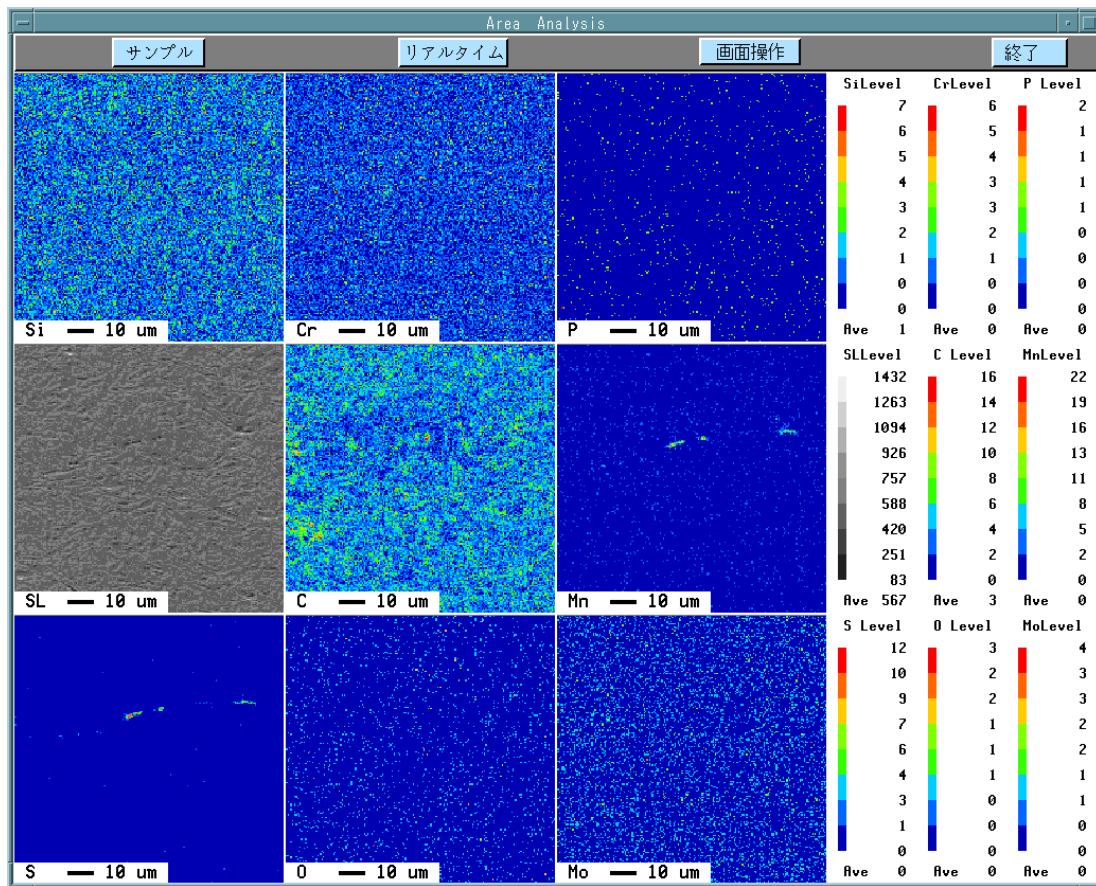

Fig. 5-11 EPMA mapping of the carburized layer (Condition B)

At the subsurface layer, the gradient of the carbon concentration at the interface between the layer and the substrate is larger than that of the carburizing and quenching heat treatment condition 2. At the end of the carburized diffusion layer, that is, the gradient of the carbon concentration at the interface between the layer and the substrate is larger than that of the carburizing and quenching heat treatment condition 2.

Some fine precipitates of MnS have also appeared, and such precipitates are

advantageous for the toughness of the material.   However, since the results obtained

with EPMA are not quantitative, it is not easy to say how much influence on yield

strength, tensile strength and stress-strain distribution. It should not be too big.
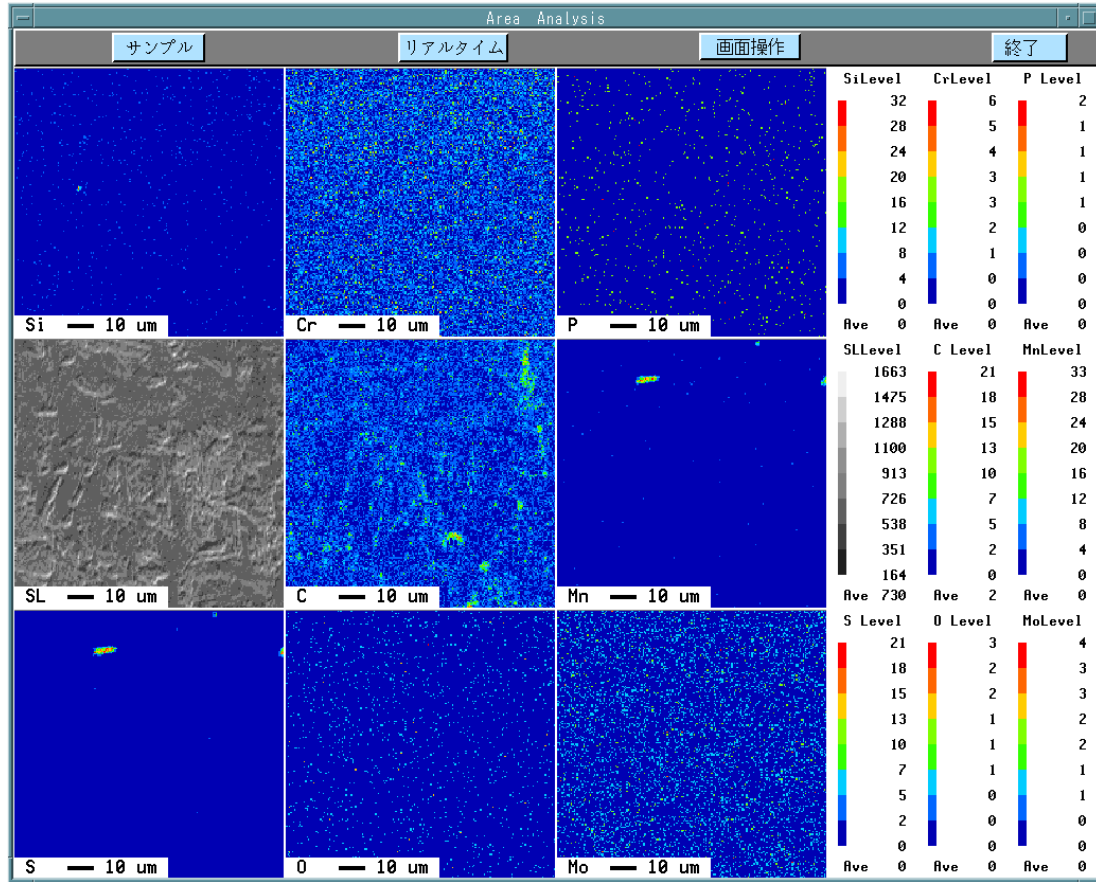

Fig. 5-12 EPMA mapping of the subsurface layer (Condition B)

In Fig. 5-13, it can be seen that there is substantially no SiC compound, but the

presence of MnS compounds, due to the occurrence of MnS compounds under two

different conditions, it is judged that the occurrence of MnS in the smelting is more

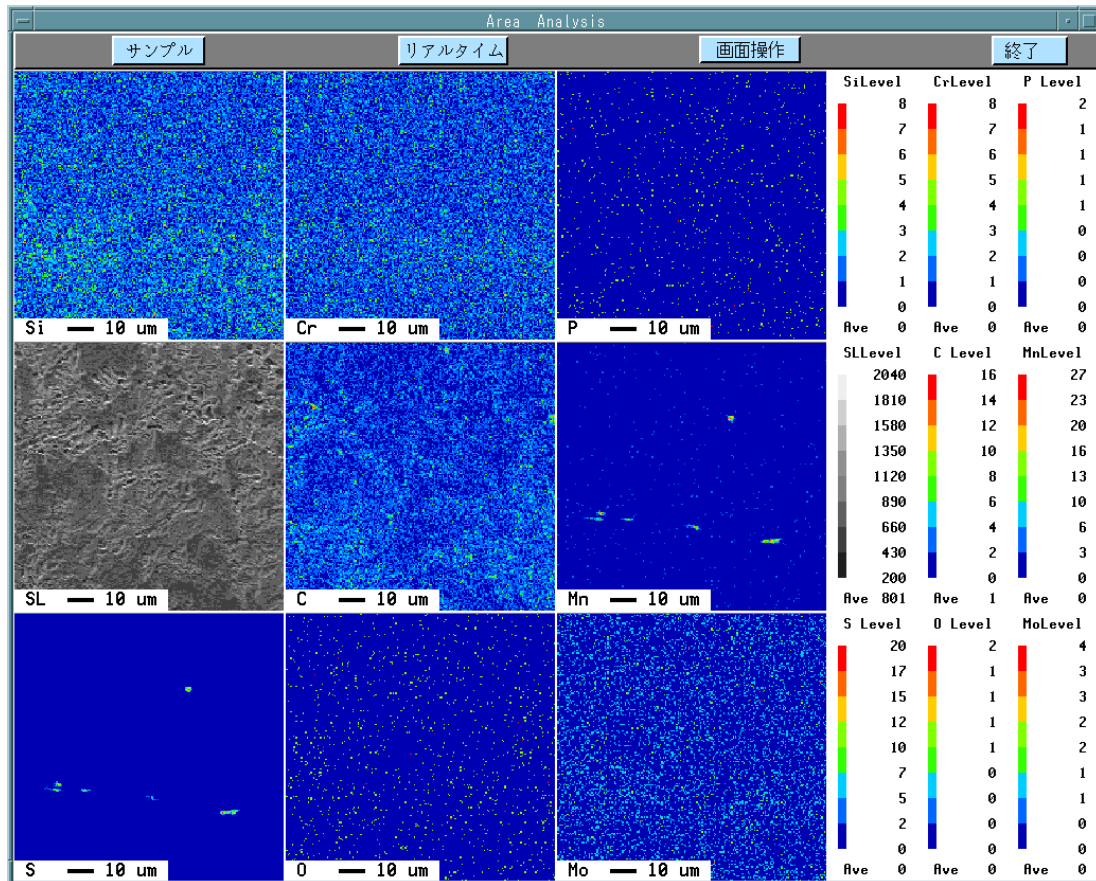likely to occur. The effect is basically the same as the result of Fig. 5-10.

Fig. 5-13 EPMA mapping of the central layer (Condition B)

5.3.3 Surface Hardness

In order to investigate the distribution of the hardness, Vickers hardness is measured of the specimens with different heat treatment conditions. The test force is selected at 49 N. Each result is the average value of three measurements.

The hardness distribution of specimens with different conditions is shown in Fig. 5-14. The measured results show good agreement with the simulated results. The carburizing and quenching processes increase the hardness to meet the requirement for carburizing and quenching production.

As is well known, the retained austenite is inversely proportional to the hardness [20]. Hence the hardness with condition B is higher due to the smaller volume fraction of retained austenite although it is theoretically estimated that the carbon content of the condition A is higher.
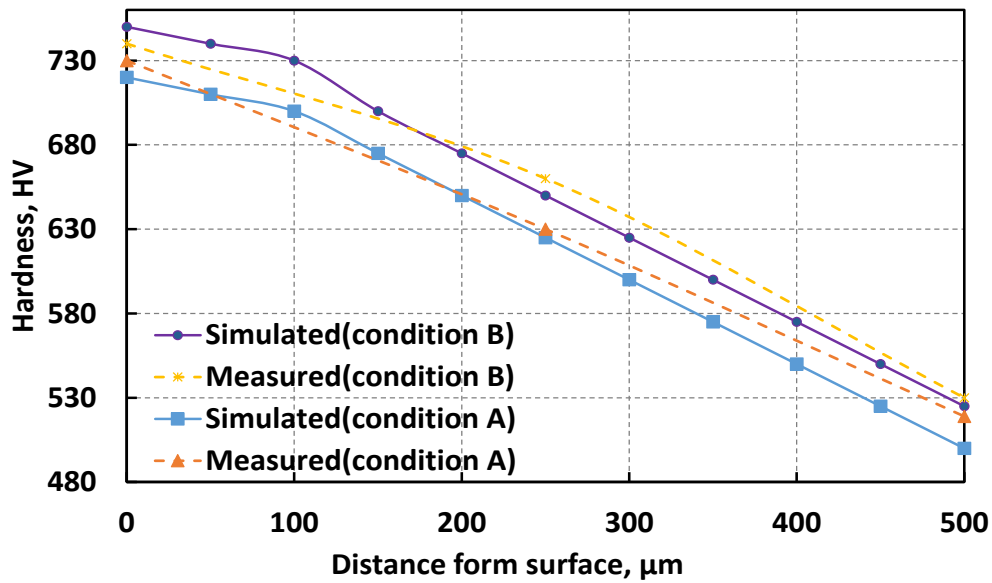
Fig. 5-14 Hardness distribution of specimens with different heat treatment conditions

5.3.4 Residual stress

Residual stresses at the surface of the specimens are measured using the X-ray diffraction stress analysis [21]. A diffractometer (Rigaku PSPC/MICRO stress analyzer) is used to produce Cr-Kα X-ray radiation at a voltage of 30 kV and an electric current of 30 mA. The instrument uses a collimator with a diameter of 0.2 mm.

The measuring point of residual stress is close to the notched tip. The directions of measurement are X direction, which are also shown in Fig. 5-15.

The residual stress distributions in the near surface layers of the test specimens are shown in Fig. 5-16. The measured results show good agreement with the simulated results. It can be observed that the maximum of the compressive residual stresses is about 200μm under the surface of the specimen and the value is about – 560MPa. With increasing depth, the compressive residual stresses are decreased gradually. The depth of the compressive residual stress zone is up to 2000μm. It can be conclude that the residual stress of carburized layer and subsurface with condition B are both greater than that with condition A. It can be considered that more compressive residual stress with condition B is more beneficial for improving the fatigue strength than that by condition A.
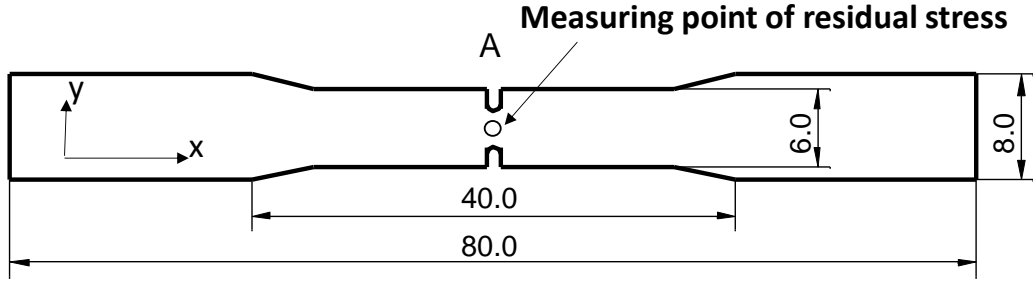
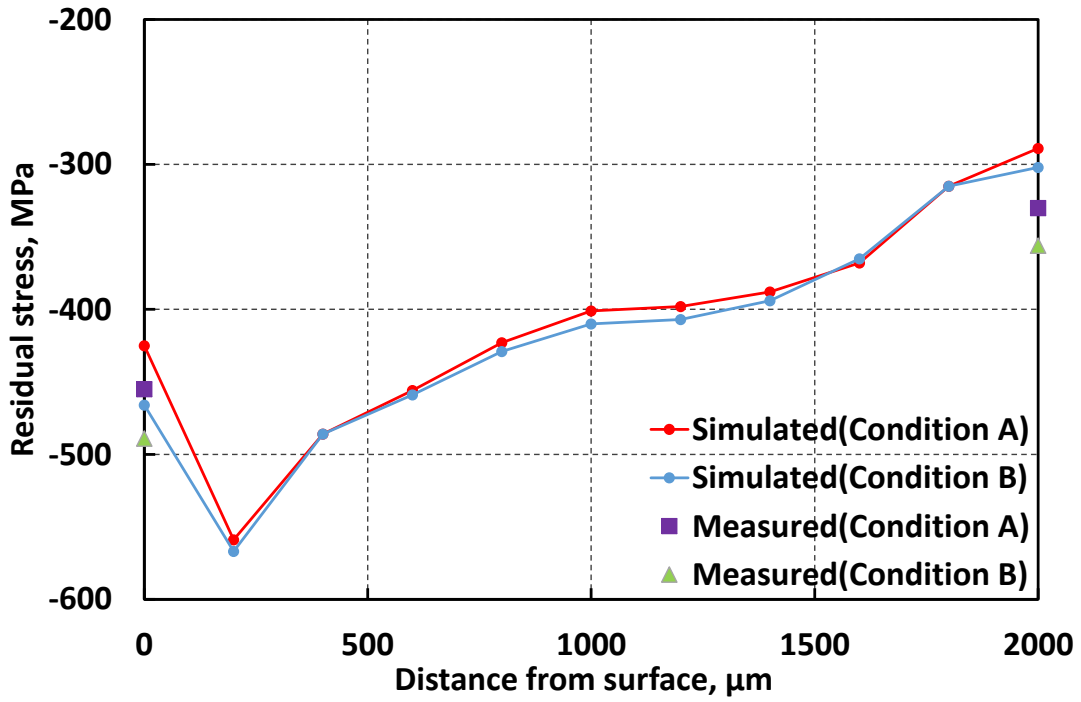Fig. 5-15 Position and direction of measurement by X-ray

Fig. 5-16 Residual stress distribution of specimens with different heat treatment conditions

5.3.5 Domain size

According to the integral breadth of ferrite {211} peak, domain size is obtained via Voigt method [22, 23]. The relationship of measured profile, the structurally broadened profile and the instrumental profile is shown in Eq. 1.

$$\beta_C^h = \beta_C^f + \beta_C^g, \quad \beta_G^{h^2} = \beta_G^{f^2} + \beta_G^{g^2}, \tag{1}$$

where β_C^h, β_C^f and β_C^g denote the Cauchy components half width of measured profile, the structurally broadened profile and the instrumental profile respectively. β_G^h and β_G^g denote the Gaussian components half width of measured profile and the instrumental profile respectively.

After deconvolution, domain sizes (D) is calculated via the following formulas. The Scherrer equation can be written as:

$$D = \lambda/(\beta_C^f * cos\theta), \tag{2}$$

where θ is the diffraction angle and λ is the wavelength of the incident X-ray.

The diffraction pattern with different conditions in the case of X-ray incident angle $\psi = 0\,^\circ$ is depicted in Fig. 5-17. The domain sizes of the specimens with different conditions are shown in Fig. 5-18. It can be proved that the heat treatment process can refine the domain of the specimens and optimized condition can obtain finer domain. It can be considered that condition B with smaller domain size is more beneficial to improve the fatigue strength than condition A.
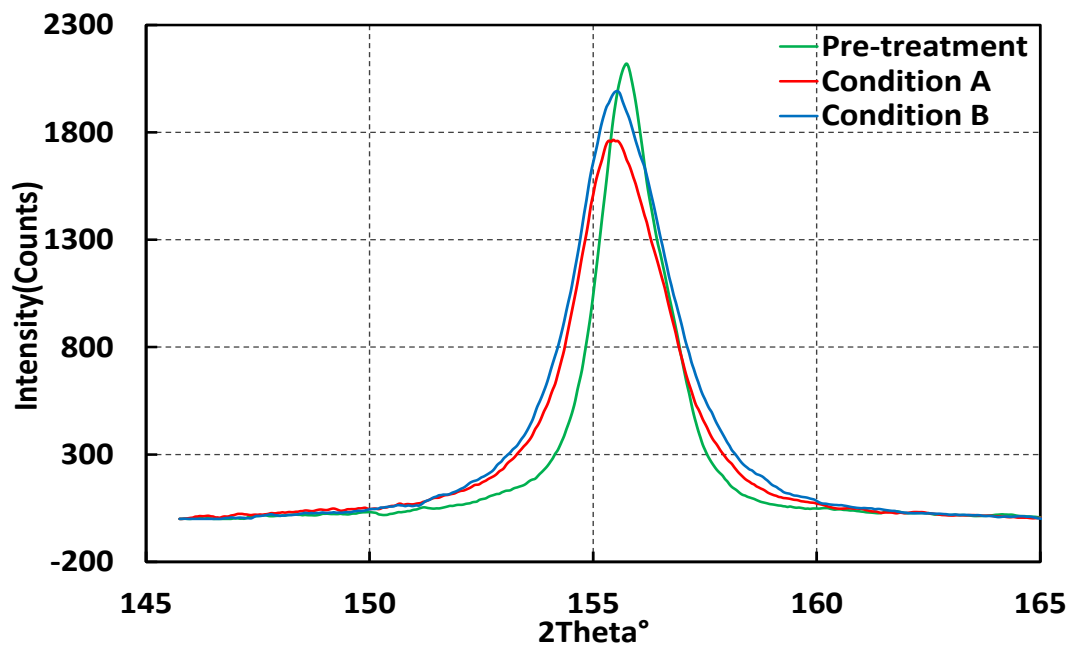

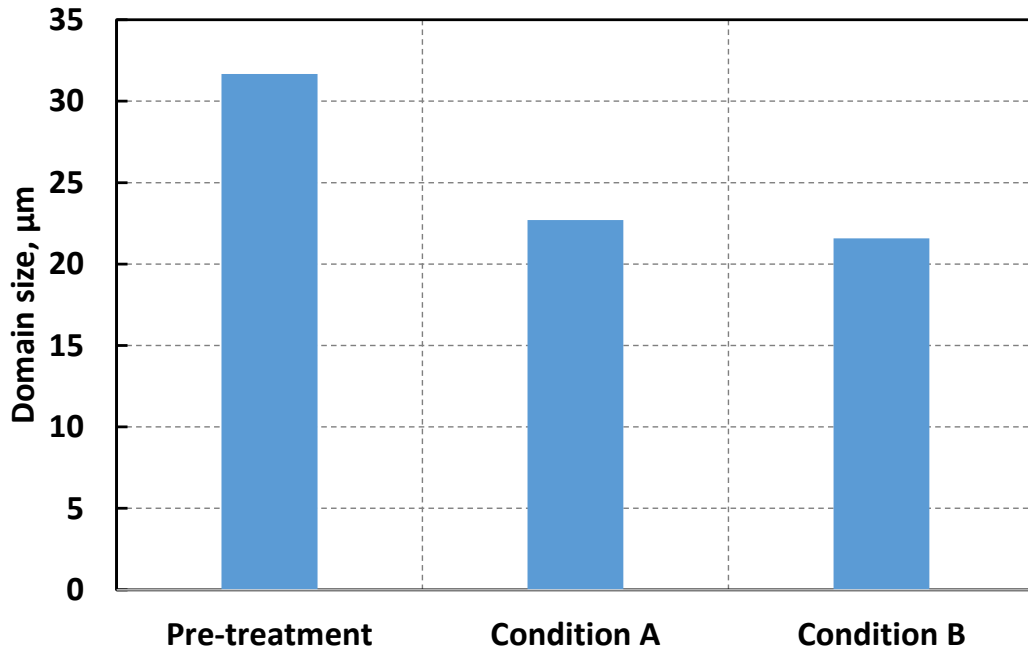Fig. 5-17 X-ray diffraction spectrum and half width

Fig. 5-18 Domain size of specimens with different conditions

5.3.6 Fatigue behavior

The test specimens with various states (original, the carburized layer, subsurface layer and central layer) were tested completely in tension–tension mode at the room temperature until fracture. In this study, load control ($R = S_{min}/S_{max} = 0.1$) using a sinusoidal waveform at 10 Hz is conducted for all testing. A Shimadzu servo-hydraulic fatigue test machine (15kN force and 25mm displacement capacities) with in situ observation by JSM-5410LV scanning microscope was used for all testing.

The fatigue limit of the specimens with different conditions are shown in Fig. 5-19. Comparing with the fatigue limit of original microstructure, it can be proved that the fatigue limits of different layers of specimens with heat treatment are improved with different extents. After carburizing and quenching, the fatigue strength of the central layer is better than that of the subsurface layer and the fatigue strength of the subsurface layer is better than that of the carburized layer. This is because of the different microstructure distribution shown in Fig. 5-7. Comparing with condition A, the condition B has a greater improvement of fatigue strength all in carburized layer, subsurface layer and central layer. Based on previous analysis, it proves that the joint

action of microstructure, domain refinement and compressive residual stress results in the strengthening mechanism.
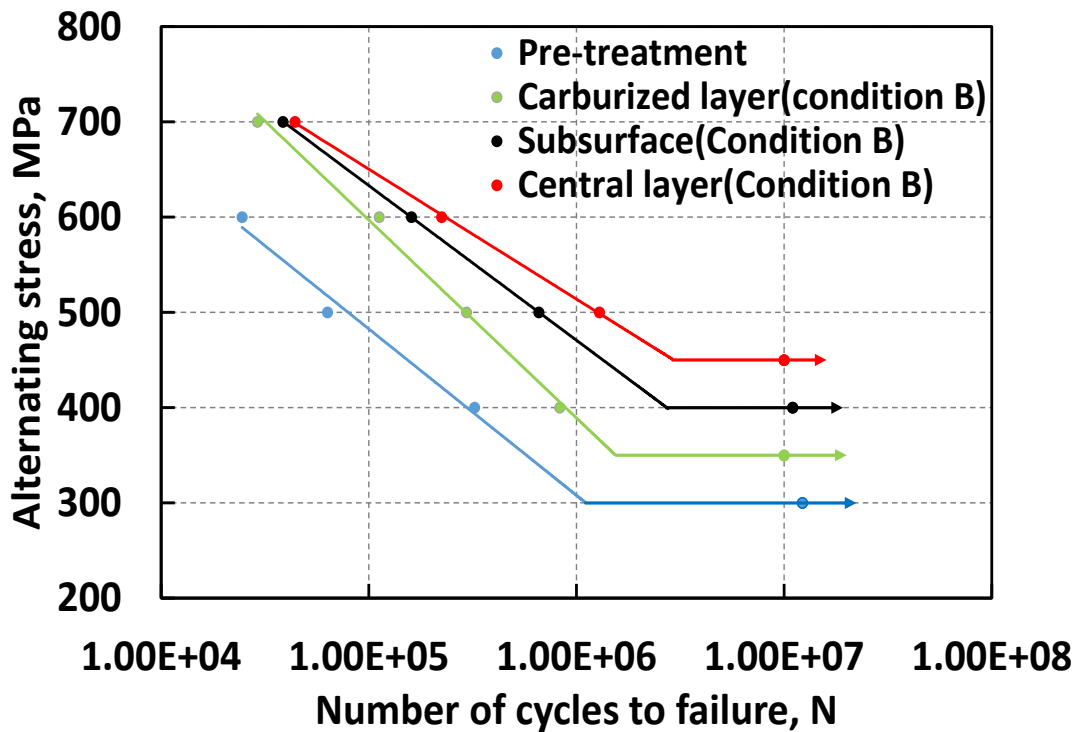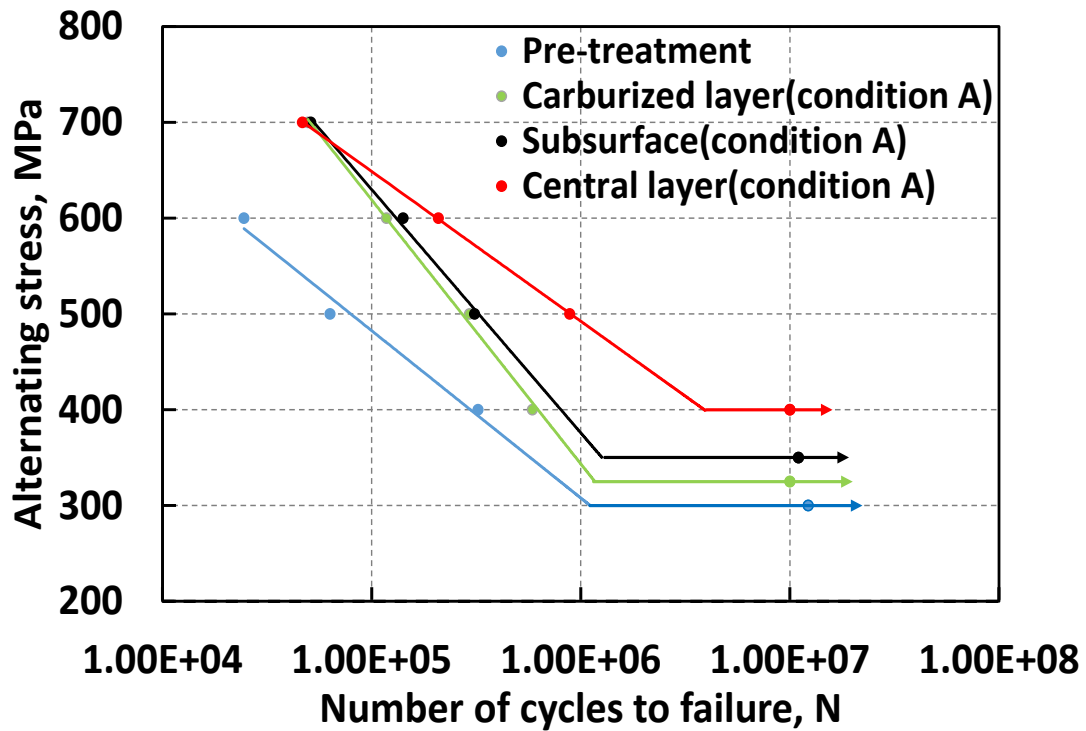

Fig. 5-19 S–N curves of the specimens with heat treatment conditions: (a) condition A; (b) condition B

5.3.7 Fatigue crack growth

The SEM photographs of crack length with different cycles are shown in Fig. 5-20. Fig. 5-20a is the crack of the initial stages with 977857 cycles, and Fig. 5-20b is the crack of the late stages with 1029507 cycles.
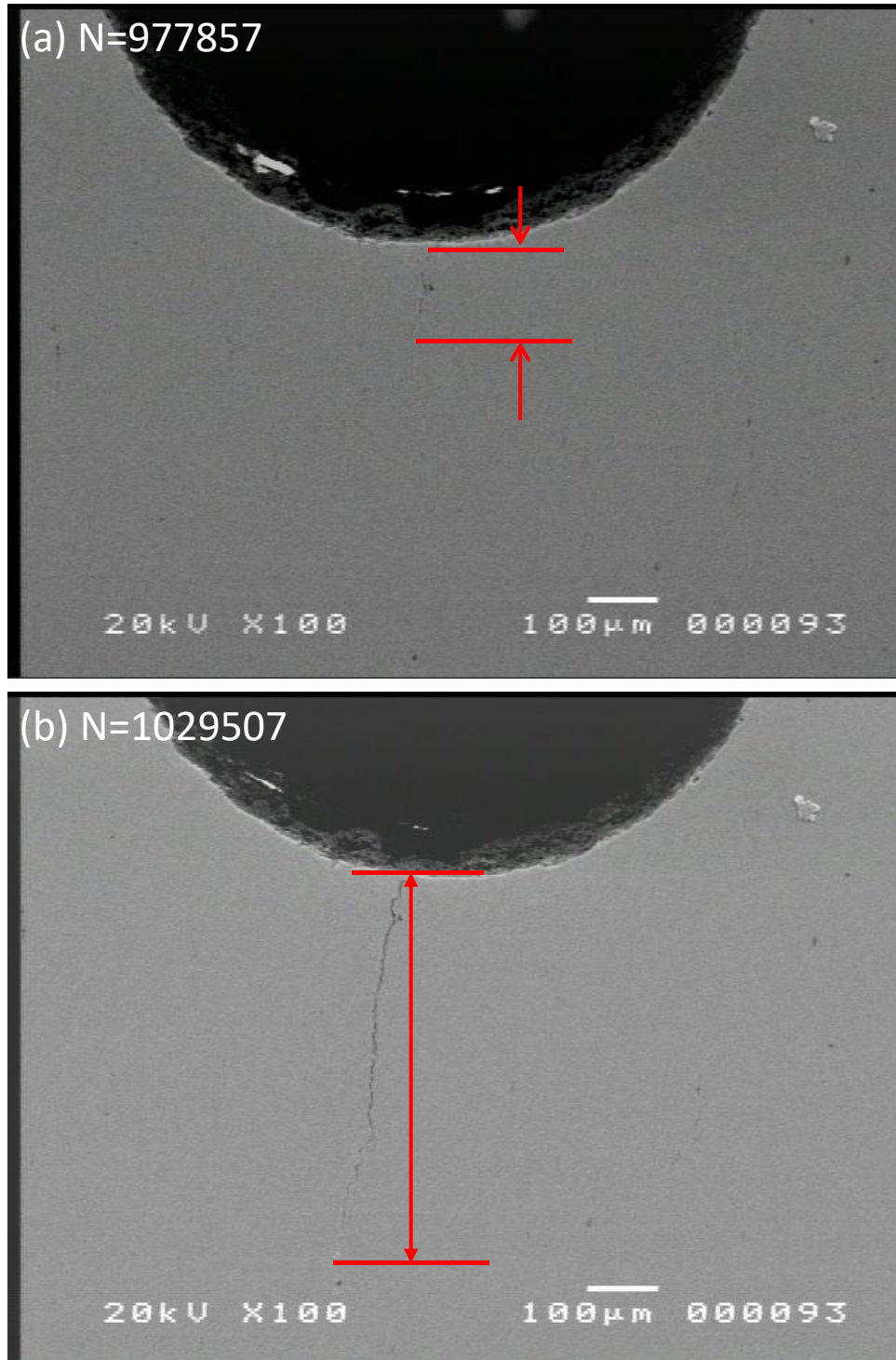

Fig. 5-20 SEM photograph of crack length of specimen with different cycles: (a) N=977857; (b) N=1029507

Crack length versus number of fatigue cycles for carburized layer with 500MPa stress level is shown in Fig. 21a. In order to characterize the crack growth behavior, the stress intensity range ΔK and the crack length per cycle da/dN were computed, and the crack growth rate curves are plotted in Fig. 21b. It can be observed that the crack initiation and the crack propagation rate of condition B is slower than that of condition A.

It is because the residual stress of specimen with condition B is larger and the domain size is smaller. It is noteworthy that when the legth of crack is 200μm, the crack growth rate becomes slower. This is because the maximum of the compressive residual stresses is about 200μm under the surface of the specimens. It is verified that the compressive residual stress has a great influence on the fatigue performance.

As shown in Fig. 22a and Fig. 22b, since the residual stress of specimen is larger, it can clearly be seen that the condition B tends to delay initiation of crack, and the crack growth life increased by 100 percent. Combining previous analysis, it is verified that the compressive residual stress and domain refinement have a great influence on the fatigue performance.

As shown in Fig. 23a and Fig. 23b, since the residual stress is almost the same, the crack is simultaneously generated. It can be proved that crack growth rate with condition B is slower due to domain refinement.

In summary, it proves that the joint action of domain refinement and compressive residual stress results in the strengthening mechanism of carburized layer and subsurface. The domain refinement results in the strengthening mechanism of central layer. The fatigue strengthening effect with condition B is better than that with condition A.

Fig. 5-21 Initiation of crack and speed of crack growth for carburized layer: (a) crack length

versus number of fatigue cycles; (b) da/dN versus ΔK

(a)

σmax=500MPa

- Subsurface(Condition A)
- Subsurface(Condition B)

crack length, μm

N, cycles

(b)

σmax=500MPa

- Subsurface(Condition A)
- Subsurface(Condition B)

da/dN, m/cycle

ΔK, MPa·m$^{1/2}$

Fig. 5-22 Initiation of crack and speed of crack growth for subsurface layer: (a) crack length versus number of fatigue cycles; (b) da/dN versus ΔK
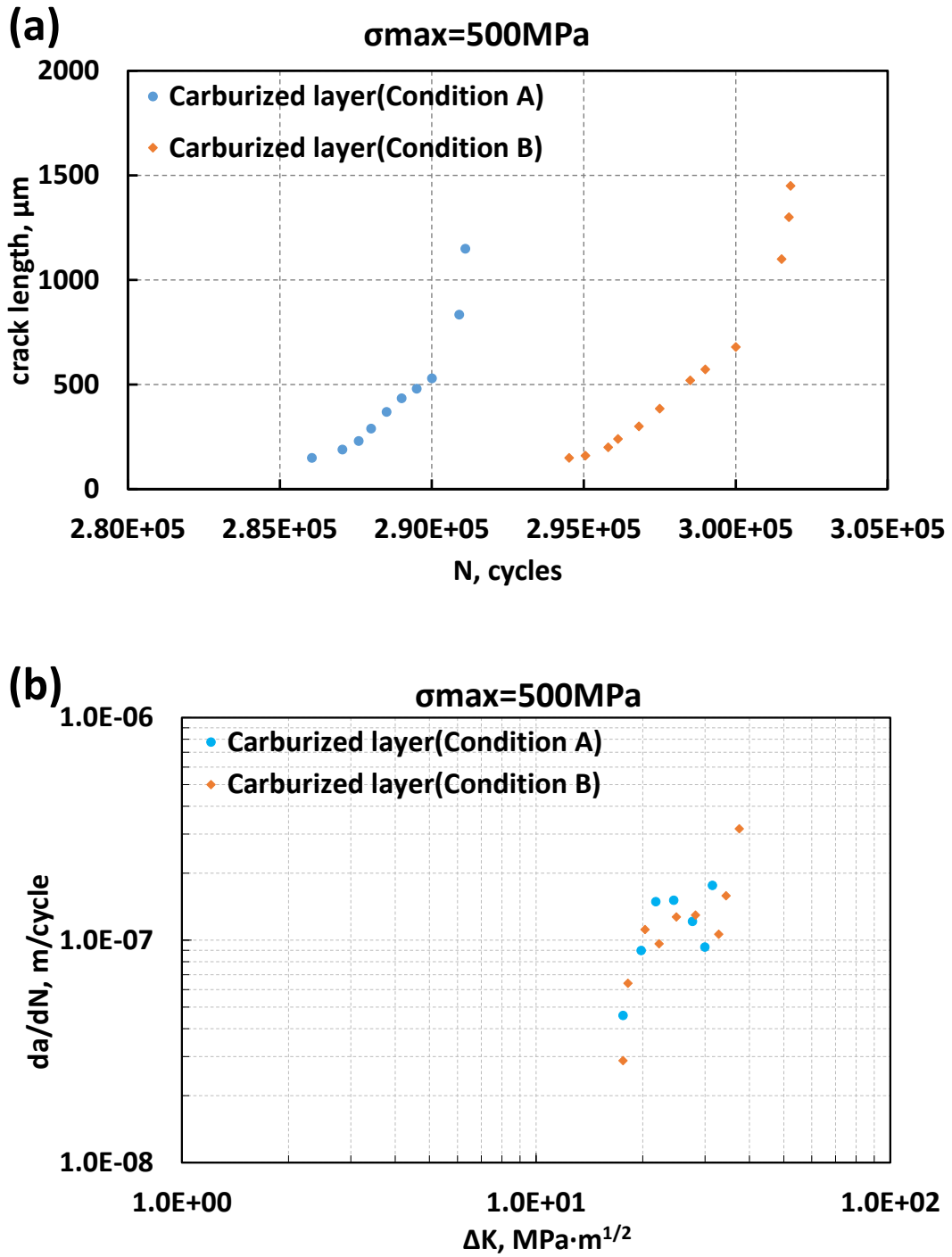
(a)

σmax=500MPa

(b)

σmax=500MPa

Fig. 5-23 Initiation of crack and speed of crack growth for central layer: (a) crack length versus
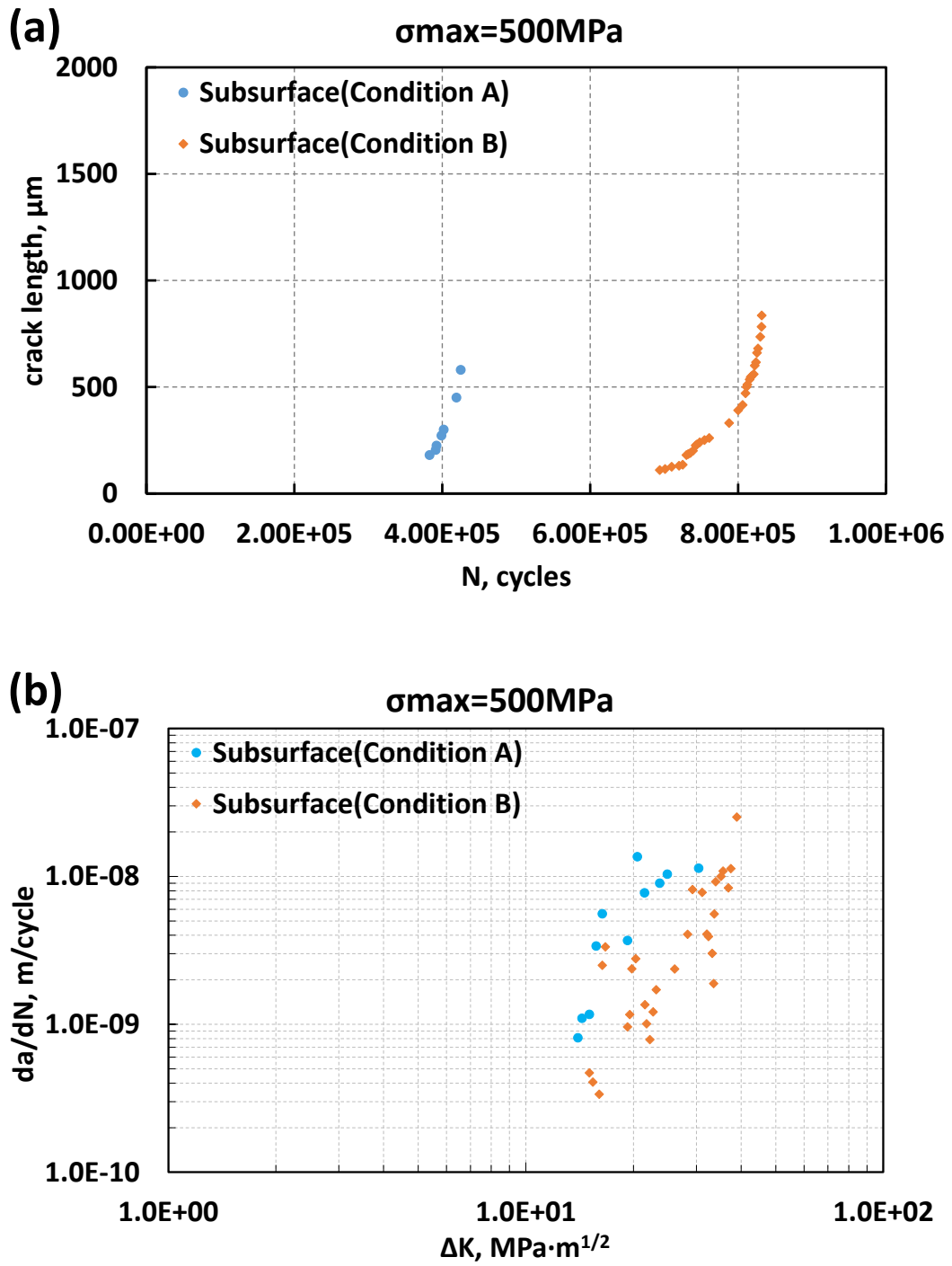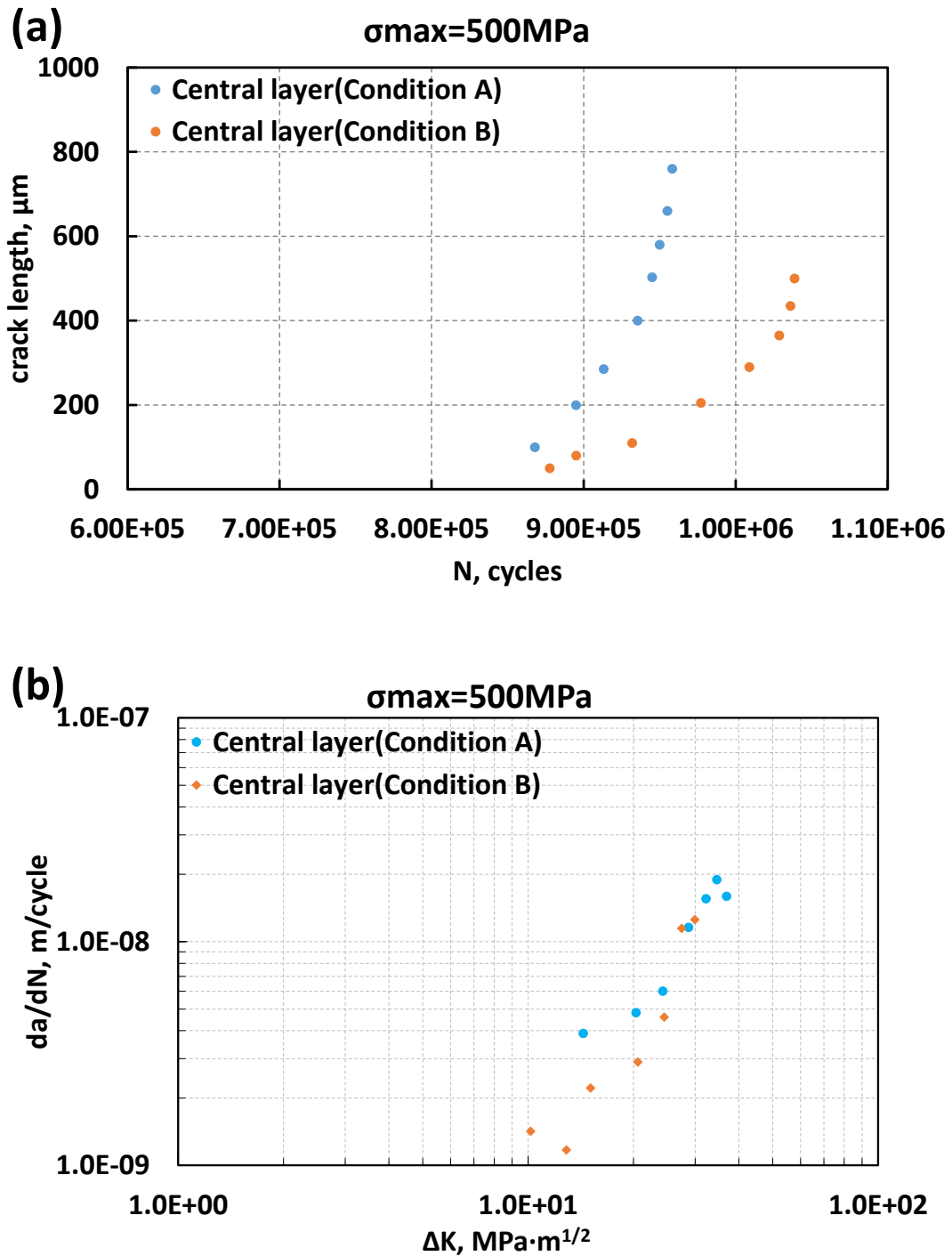
number of fatigue cycles; (b) da/dN versus ΔK

5.3.8 Fracture morphology

The fracture morphology is shown in Fig. 5-24. Fig. 5-24(a) and (b) are toughness

fracture surface, and Fig. 5-24 (c) and (d) are brittleness fracture surface, fatigue

striation patterns can be clearly observed on the toughness fracture surface.
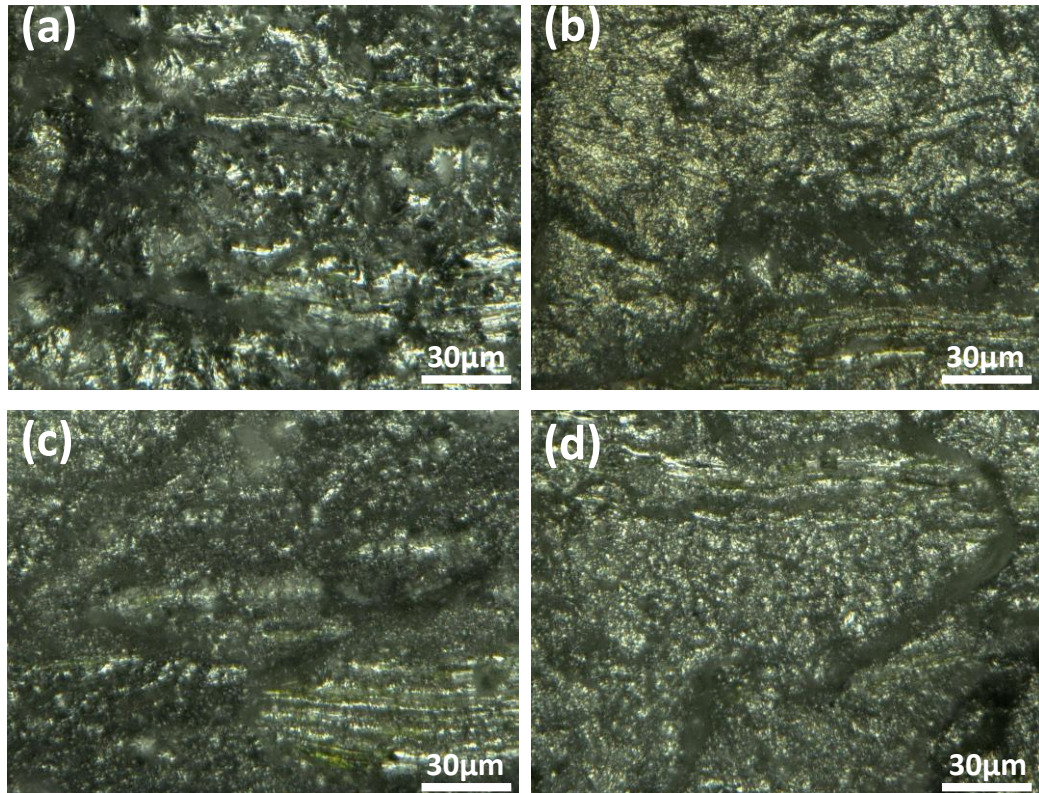

Fig. 5-24 Fracture morphology with different heat treatment conditions: (a) Carburized layer with condition A (b) Carburized layer with condition B (c) Subsurface layer with condition A (d) Subsurface layer with condition B

5.4 Conclusion remarks

The fatigue life of carburized parts is great significance for the engineering design. In the present work the improvement of fatigue performance and strengthening mechanism with different conditions are discussed in detail. The following conclusions can be drawn as:

(1) It is proved that the fatigue performance of different layers of specimens with heat treatments are improved with different extents. The optimization condition has better reinforcing effect;

(2) Condition B results in higher compressive residual stress, smaller domain size and less retained austenite;

(3) The surface hardness with condition B is higher due to the smaller volume

fraction of retained austenite;

(4) The joint action of domain refinement, compressive residual stress and microstructure result in the strengthening mechanism of fatigue performance. Where, the joint action of domain refinement and compressive residual stress results in the strengthening mechanism of carburized layer and subsurface layer. The domain refinement results in the strengthening mechanism of central layer.

References

[1] **Boniardi, M., D'Errico, F. and Tagliabue, C.,** "Influence of carburizing and nitriding on failure of gears – A case study," *Engineering Failure Analysis,* 2006, vol. 13, no. 3, pp. 312-339.

[2] **Genel, K. and Demirkol, M.,** "Effect of case depth on fatigue performance of AISI 8620 carburized steel," *International Journal of Fatigue,* 1999, vol. 21, no. 2, pp. 207-212.

[3] **Srinivasan, R., Natarajan, S. and Sivakumar, V. J.,** "Fatigue life improvement on 20MnCr5 steel through surface modification for auto transmission application," *Archives of Civil and Mechanical Engineering,* 2019, vol. 19, no. 2, pp. 360-374.

[4] **Nojima, K., Ogata, K., Tanaka, M., Nishi, R., Ono, Y. and Koide, T.,** "Bending fatigue strength of case-carburized helical gears (In the case of large helix angles)," *Journal of Mechanical Science and Technology,* 2017, vol. 31, no. 12, pp. 5657-5663.

[5] **Zhang, J., Zhang, Q., Wu, C., Xu, Z. and Lyu, S.,** "Experimental application of pitting formation for 20MnCr5 carburized gear tooth," *International Journal of Precision Engineering and Manufacturing,* 2014, vol. 15, no. 5, pp. 899-903.

[6] **Wang, W., Liu, H., Zhu, C., Bocher, P., Liu, H. and Sun, Z.,** "Evaluation of Rolling Contact Fatigue of a Carburized Wind Turbine Gear Considering the Residual Stress and Hardness Gradient," *Journal of Tribology,* 2018, vol. 140, no. 6, pp. 1-10.

[7] **Chen, Z.-K., Zhou, T., Zhao, R.-Y., Zhang, H.-F., Lu, S.-C., Yang, W.-S. and Zhou, H.,** "Improved fatigue wear resistance of gray cast iron by localized laser carburizing," *Materials Science and Engineering: A,* 2015, vol. 644, pp. 1-9.

[8] **Jo, B., Sharifimehr, S., Shim, Y. and Fatemi, A.,** "Cyclic deformation and fatigue behavior of carburized automotive gear steel and predictions including multiaxial stress states," *International Journal of Fatigue,* 2017, vol. 100, no. 2, pp. 454-465.

[9] **Masoudi Nejad, R., Farhangdoost, K. and Shariati, M.,** "Numerical study on fatigue crack growth in railway wheels under the influence of residual stresses," *Engineering Failure Analysis,* 2015, vol. 52, pp. 75-89.

[10] **Asi, O., Can, A. Ç., Pineault, J. and Belassel, M.,** "The relationship between case depth and bending fatigue strength of gas carburized SAE 8620 steel," *Surface and Coatings Technology,* 2007, vol. 201, no. 12, pp. 5979-5987.

[11] **Farivar, H., Deepu, M. J., Hans, M., Phanikumar, G., Bleck, W. and Prahl, U.,** "Influence of post-carburizing heat treatment on the core microstructural evolution and the resulting mechanical properties in case-hardened steel components," *Materials Science and Engineering: A,* 2019, vol. 744, pp. 778-789.

[12] **Yin, D., Liu, H., Chen, Y., Yi, D., Wang, B., Wang, B., Shen, F., Fu, S., Tang, C., and Pan, S.,** "Effect of grain size on fatigue-crack growth in 2524 aluminium alloy," *International Journal of Fatigue,* 2016, vol. 84, pp. 9-16.

[13] **Hu, D., Mao, J., Song, J., Meng, F., Shan, X. and Wang, R.,** "Experimental investigation of grain size effect on fatigue crack growth rate in turbine disc superalloy GH4169 under different temperatures," *Materials Science and Engineering: A,* 2016, vol. 669, pp. 318-331.

[14] **Mukai, R., Matsumoto, T., Ju, D.-y., Suzuki, T., Saito, H. and Ito, Y.,** "Modeling of numerical simulation and experimental verification for carburizing-nitriding quenching process," *Transactions of Nonferrous Metals Society of China,* 2006, vol. 16, pp. s566-s571.

[15] **Zhang, X., Tang, J.-y. and Zhang, X.-r.,** "An optimized hardness model for carburizing-quenching of low carbon alloy steel," *Journal of Central South University,* 2017, vol. 24, no. 1, pp. 9-16.

[16] **Kim, N.-K. and Bae, K.-Y.,** "Analysis of deformation in the carburizing-quenching heat treatment of helical gears made of SCM415H steel," *International Journal of Precision Engineering and Manufacturing,* 2015, vol. 16, no. 1, pp. 73-79.

[17] **Enloe, C. M., Findley, K. O. and Speer, J. G.,** "Austenite Grain Growth and Precipitate Evolution in a Carburizing Steel with Combined Niobium and Molybdenum Additions," *Metallurgical and Materials Transactions A,* 2015, vol. 46, no. 11, pp. 5308-5328.

[18] **Liu, Y.-q., Chen, Y., Ju, D.-Y. and Miao, S.,** "Optimization Based on Orthogonal Experiment Design and Numerical Simulation for Carburizing Quenching Process of Helical Gear," *Materials Performance and Characterization,* 2018, vol. 7, no. 6.

[19] **Ju, D.-Y. and Inoue, T.,** "On the Material Process Simulation Code COSMAP-Simulated Examples and its Experimental Verification for Heat Treatment Process," *Key Engineering Materials,* 2007, vol. 345-346, pp. 955-958.

[20] **Cola ço, R. and Vilar, R.,** "On the influence of retained austenite in the abrasive wear behaviour of a laser surface melted tool steel," *Wear,* 2005, vol. 258, no. 1-4, pp. 225-231.

[21] **Ju, D. Y. and Han, B.,** "In-situ observation of dislocation and analysis of residual stresses by FEM/DDM modeling in water cavitation peening of pure titanium," *IOP Conference Series: Materials Science and Engineering,* 2015, vol. 82.

[22] **Vives, S., Gaffet, E. and Meunier, C.,** "X-ray diffraction line profile analysis of iron ball milled powders," *Materials Science and Engineering: A,* 2004, vol. 366, no. 2, pp. 229-238.

[23] **Luan, W., Jiang, C., Wang, H., Panardie, J. and Chen, D.,** "XRD investigation of thermostability of TiB2/Al deformation layer introduced by shot peening," *Materials Science and Engineering: A,* 2008, vol. 480, no. 1-2, pp. 1-4.

Chapter 6 Summary

In this thesis, a new transformation plasticity theory in heating stage is proposed. In consideration of material properties, oil for quenching, process influencing factors, etc., the experimental design method, simulation and experimental verification was used. Optimized design for carburizing and quenching process of steel 20MnCrS5 was carried out.

In Chapter 2, the material properties are calculated, a new transformation plasticity theory applied to the austenite transformation is proposed and experimentally verification is carried out simultaneously. The following conclusions also be obtained, a new mathematic model has been developed to describe the transformation plasticity behavior of steels during the austenite transformation, which includes the influence of the dynamic recrystallization of the austenite; Transformation plasticity coefficient in the austenite transformation is not a constant value in proportion to the stress and transformation plasticity strain. As the tensile stress increases, the increase degree of transformation plastic strain decreases significantly.

In Chapter 3, heat treatment of round bars considering transformation plasticity in the carburizing quenching process by software COSMAP was simulated and it is proved that simulation accuracy is improved. The following conclusions also be obtained, Transformation plastic behavior is sufficiently measurable; it is also proved that Excessive heat transfer rate leads to increased deformation.

In chapter 4, simulation and experimental verification of total 27 heat treatment process conditions considering heat treatment process condition, selection of quenching oil and gear orientation during quenching are used. In addition, a multi-purpose evaluation of hardness, residual stress and deformation of gears was used to the experimental design method and an optimal process for carburizing and quenching of gears was designed. The following conclusions also be obtained: Selection of optimal cases are determined by the indexes of the distortion of tooth trace. The optimal case

determined by the distortion of tooth trace is carburizing time (120min), cooling time before 860℃ (30min), holding time at 860℃ (45min) and the gear orientation during quenching (60 °).

In chapter 5, it was demonstrated that by optimum carburizing quenching process, fatigue strength of the test piece is increased while maintaining the surface hardness. The following conclusions also be obtained, the joint action of domain refinement, compressive residual stress and microstructure result in the strengthening mechanism of fatigue performance. Where, the joint action of domain refinement and compressive residual stress results in the strengthening mechanism of carburized layer and subsurface layer. The domain refinement results in the strengthening mechanism of central layer.

Related Publications

[1] Miao, S., Ju, D. Y., and Zhao, H. J., "Residual Stress Modification and Mechanisms of Bearing Steel with Different Microstructures during Water-Jet Cavitation Peening," Materials Performance and Characterization, Vol. 7, No. 4, 2018, pp. 747-758. DOI: 10.1520/MPC20170108 (EI Journal)

[2] Miao, S., Ju, D. Y., Chen, Y., and Liu, Y. Q., "Optimization Based on Orthogonal Experiment Design and Numerical Simulation for Carburizing Quenching Process of Helical Gear," Materials Performance and Characterization, Vol. 8, No. 2, 2018, DOI: 10.1520/MPC20180019 (EI Journal)

[3] Miao, S., Wang, J. G., Ju, D. Y., Zhao, H. J. and Yan, M. Y., " Improvement and Analysis of Fatigue Strength for Mild Steel 20MnCrS5 during Carburizing and Quenching," Materials Science, Vol. 26, No. 2, 2020. (SCI Journal- In press)

[4] Miao, S., Ju, D. Y., Yan, M. Y. and Zhao, H. J., "Study on Transformation Plasticity Behavior of steels during Austenite transformation," Journal of Mechanical Science and Technology (in review)